EAST EUROPEAN JOURNAL OF PHYSICS. 1. 82-88 (2023)
DOI:10.26565/2312-4334-2023-1-09 ISSN 2312-4334

THEORETICAL STUDY OF MATTER DENSITY DISTRIBUTIONS, AND ELASTIC ELECTRON SCATTERING FORM FACTORS OF EXOTIC NUCLEI (^{26}F AND ^{9}C)†

Abeer A. M. Hussein*, Ghaith N. Flaiyh
Department of Physics, College of Science, University of Baghdad, Baghdad, Iraq
**Corresponding Author e-mail: Abeer.Ali1104a@sc.uobaghdad.edu.iq*
Received November 30, 2022; revised December 23, 2022; accepted December 26, 2022

The distributions of nuclear density, root mean square radii, and elastic electron scattering form factor are calculated for nuclei (^{9}C) (core +2p) and (^{26}F) (core +2n) with the two different nuclear potential parameters for (*bc*) and (*bv*), where correlations for both the (effects tensor force and short-range) are used, and the appearance of the long extension is observed in nuclear density distributions for these nuclei. Fortran 95 power station was used to program nuclear properties such as nucleon density (matter, neutron, and proton), elastic electron scattering form factor, and *rms* radii. The computed results for these exotic nuclei are determined to correspond pretty well with the experimental data.
Keywords: *Exotic nuclei; Form factor; Nuclear density (neutron, proton, matter); Neutron-rich; Proton-rich*
PACS: 21.10k, 21.10ft, 21.10Gv, 21.60Jz, 25.40.-h, 25.40.Cm, 25.40.Dn

1. INTRODUCTION

From properties the Halo nuclei: a few weakly bound halo nucleons and a more strongly bound core where This scale separation can be exploited in a few-body description of halo nuclei, because the halo nucleons do not determine the exact structure of the core [1]. Nuclear density distribution is an important factor [2] it's an essential component of both experimental and theoretical research, where the experimental matter density distributions of unusual nuclei are characterized mostly by long tail behavior [3]. Numerous solutions have been put out to deal with tension forces since including short-range correlations and tension forces is a difficult challenge, particularly for the theory of nuclear structure [4,5]. Dellagiacoma et al. presented a simple phenomenological strategy for establishing dynamic short-range and tensor effects [6].

The neutron halo in some neutron-rich nuclei is one of the most intriguing discoveries in recent experimental research employing radioactive nuclear beams [7,8]. Halo nuclei (^{8}He and ^{26}F) were studied by Ghufran M. [9] using the 3-body harmonic oscillator model and Woods-Saxon radial wave functions. While studying the theoretical outlines of calculations, assume that the nuclei understudy are composed of two parts: the stable core and the unstable halo, where the core part is studied using the radial wave functions of harmonic-oscillator (HO) potentials, and the halo is studied using the Woods-Saxon (WS) potential for (^{8}B, ^{17}Ne, ^{11}Be, and ^{11}Li) nuclei by Arkan et al. [10].

In contrast, research on the proton halo in proton-rich nuclei has piqued the curiosity of many in last years, with theory based on relative mean approximation (RMF) predicting the presence of a proton halo structure in some proton-rich nuclei [11, 12], and The ground-state density of the unstable proton-rich ^{9}C, ^{12}N, and ^{23}Al exotic nuclei was investigated using the dual-frequency shell model and binary mass model [13]. The proton emission potentials of several single protons and proton halo nuclei of heavy isotopes (SH) with Z= 121–128 were investigated using the Coulomb model and the proximity potentials as a reactive barrier by Anjali. and others [14].

In this work are studied using the formula two-body charge density distributions for the halo nuclei {^{26}F(core+2n)} and {^{9}C(core+2p)} by using two function shell model (TFSM) with two different parameters *bc* and *bv* for calculated The root mean square radii (*rms*), form factors and the nuclear density (matter, protons, and neutrons) of the ground state with full correlation effects (short range and tensor force).

2. THEORY

The following transforms the one-body density in eq. (1) operator into a two-body density form $\hat{\rho}^{(1)}(\vec{r}) \Rightarrow \hat{\rho}^{(2)}(\vec{r})$ as shown in eq. (2) [15]:

$$\hat{\rho}^{(1)}(\vec{r}) = \sum_{i=1}^{A} \delta(\vec{r} - \vec{r}_i) \tag{1}$$

$$\sum_{i=1}^{A} \delta(\vec{r} - \vec{r}_i) \equiv \frac{1}{2(A-1)} \sum_{i \neq j} \left\{ \delta(\vec{r} - \vec{r}_i) + \delta(\vec{r} - \vec{r}_j) \right\} \tag{2}$$

Another relevant transformation is that of the coordinates of the two particles, which may be expressed, ($\vec{r}_i$ and $\vec{r}_j$), in terms of that relative $\vec{r}_{ij}$, and center -of- mass $\vec{R}_{ij}$ coordinates [16]:

† ***Cite as:*** A.A.M. Hussein, and G.N. Flaiyh, East Eur. J. Phys. **1**, 82 (2023), https://doi.org/10.26565/2312-4334-2023-1-09

$$\vec{r}_{ij}=\frac{1}{\sqrt{2}}(\vec{r}_i-\vec{r}_j) \tag{i}$$

$$\vec{R}_{ij}=\frac{1}{\sqrt{2}}(\vec{r}_i+\vec{r}_j) \tag{ii}$$

Using Eqs. (i) and (ii) in Eq. (2)

$$\hat{\rho}^{(2)}(\vec{r})=\frac{1}{2(A-1)}\sum_{i\neq j}\left\{\delta\left[\vec{r}-\frac{1}{\sqrt{2}}(\vec{R}_{ij}+\vec{r}_{ij})\right]+\delta\left[\vec{r}-\frac{1}{\sqrt{2}}(\vec{R}_{ij}-\vec{r}_{ij})\right]\right\} \tag{3}$$

Using the identity by Hamoudi et al. [17] $\delta(a\vec{r})=\frac{1}{|a^3|}\delta(\vec{r})$ (for three-dimension)

Where (a), is a constant. Then eq. (3) becomes:

$$\hat{\rho}^{(2)}(\vec{r})=\frac{\sqrt{2}}{(A-1)}\sum_{i\neq j}\left\{\delta\left[\sqrt{2}\vec{r}-\vec{R}_{ij}-\vec{r}_{ij}\right]+\delta\left[\sqrt{2}\vec{r}-\vec{R}_{ij}+\vec{r}_{ij}\right]\right\} \tag{4}$$

The operator from Equation (4), can be folded with the two-body operator functions $\tilde{f}_{ij}$ to yield an efficient two-body charge density operator, (utilized for uncorrelated wave functions).

$$\hat{\rho}^{(2)}_{eff}(\vec{r})=\frac{\sqrt{2}}{(A-1)}\sum_{i\neq j}\tilde{f}_{ij}\left\{\delta\left[\sqrt{2}\vec{r}-\vec{R}_{ij}-\vec{r}_{ij}\right]+\delta\left[\sqrt{2}\vec{r}-\vec{R}_{ij}+\vec{r}_{ij}\right]\right\}\tilde{f}_{ij} \tag{5}$$

Where the from $\tilde{f}_{ij}$, is given by [18]

$$\tilde{f}_{ij}=f(r_{ij})\Delta_1+f(r_{ij})\left\{\ 1+\alpha(\mathrm{A})B_{ij}\ \right\}\Delta_2 \tag{6}$$

It's evident of eq. (6), includes two kinds of effects:

I. The first term of equation (6), two-body short range correlations, denoted by (r_{ij}). Here Is a projection operator on the space of all two-body wave functions, with the exception of $^3S^1$ and $^3D_1$ states. Short-range correlations are significant functions of particle separation because they reduce the two-body wave function at short distances where the repulsive core drives the particles apart and heal to unity at long distances where the interactions are very weak. [19] gives the two-body short range correlation**.**

$$f(r_{ij})=\begin{Bmatrix}0 & for\ r_{ij}\le r_c\\ 1-\exp\{-\mu(r_{ij}-r_c)^2\} & for\ r_{ij}>r_c\end{Bmatrix} \tag{7}$$

II. When r_c (*fm*), is the radius of a suitable hard core, and μ =25 fm^{-2} [18], correlation parameter.

The strong tensor, component in the nucleon - nucleon force induces the longer range two- body tensor correlations, that are shown in the second term of equation (6). This projection operator only affects the $^3S_1$ and $^3D_1$ states. The typical tensor operator, B_{ij}, is known as [18], and is created by the scalar product for intrinsic spin space, with coordinate space:

$$B_{ij}=\frac{3}{r_{ij}^2}(\vec{\sigma}_i.\vec{r}_{ij})(\vec{\sigma}_j.\vec{r}_{ij})-\vec{\sigma}_i.\vec{\sigma}_j \tag{8}$$

It makes sense to parameterize the core, and halo densities independently in the case of exotic (halo) nuclei. Eq. (5)'s ground state density distribution can be separated into two portions, one of which is the matter density distribution for the complete exotic nucleus [20].

$$\rho_m(r)=\rho^c_{(p+n)}(r)+\rho^v_n(r) \tag{9}$$

The following formulas produce the *rms* radii of the matching aforementioned densities [20]:

$$\left\langle r^2\right\rangle^{1/2}_U=\frac{4\pi}{U}\int_0^\infty\rho^U(r)r^4\,dr \tag{10}$$

Where U is (proton, neutron or matter). Using ground-state charge density distributions, the elastic electron scattering form factor can be computed. According to the Plane Wave Born Approximation (PWBA), incident and dispersed electron waves are assumed to be plane waves, and charge density distributions are real and spherical symmetric, therefore the form factor is just the Fourier transform of the charge density distribution, resulting in [21]:

$$F(q)=\frac{4\pi}{qZ}\int_0^{\infty}\rho_o(\mathrm{r})\mathrm{Sin}(q\mathrm{r})\mathrm{r}\;dr\,F_{fs}(q)\,F_{cm}(q) \tag{11}$$

Where $F_{cm}(q)$, is the center of mass corrections and F_{fs} (q), is the finite nucleon size The free nucleon form factor, $F_{fs}(q)$ is considered to be the same for protons and neutrons. This correction is written as follows [21]:

$$F_{fs}(q)=e^{-0.43q^2/4} \tag{12}$$

Where the free nucleon form factor F_{fs} (q), for protons and neutrons is consider to be the same. According to [20], the center of mass correction F_{cm} (q) is as follows:

$$F_{cm}(q)=e^{q^2w^2/4A} \tag{13}$$

Where (w) is the harmonic-oscillator size parameter, and (A) is the nuclear mass number.

As a result, when the shell model wave function is, removes F_{cm} (q) eliminates the spurious state caused by the center of mass's motion. The ground state (r) of equation (5), which we obtain after these modifications, can now be used to calculated the form factor $F(q)$ incorporating the impact of two- body correlation functions (11).

3. RESULTS AND DISCUSSION

The nuclear ground state properties of two-neutron (^{26}F) and two-proton (^{9}C) exotic nuclei have been calculated using two- body nucleon density distributions, with including the effect of two-body correlations tenser force (α=0.1) and short range (rc=0.5 fm) using two frequency shell model (TFSM) by relying on equations 5, 7, and 8, where the two particle harmonic oscillator wave functions were employed with two different size parameters of b_c and b_v, where we supposed that which the two- neutron occupies the $2s_{1/2}$ orbital for (^{26}F) and two- proton occupies the $1p_{1/2}$ for (^{9}C) . Elastic electron scattering form factors for these nuclei are studied through combining the charge density distribution with the Plane Wave Born Approximation.

Table 1 Show average radius of neutrons and protons was calculated based on equations (5), (6) and (10), where we got the results when the full correlation (r_c=0.5 fm, α =0.1) and without correlation (r_c=0, α=0) .

Table 2 displays the values of the harmonic oscillator size parameter b_c and b_v utilized in the two function shell model (TFSM) of the present calculations for the selected exotic nuclei and the calculated *rms* radii for core (^{24}F and ^{7}Be) nuclei and exotic nuclei (^{26}F and ^{9}C) when FC's (r_c = 0.5 fm, α = 0.1) the calculated results are in good agreement with the indicated experimental data [22, 23, 24].

Table 1. The computed neutron and proton *rms* radii for (^{26}Fand ^{9}C) nuclei.

Exotic nuclei ^{26}F			
Proton size parameter	**b_p=1.965 fm**	**Neutron size parameter**	**b_n=2.09 fm**
$\langle r_p^2\rangle^{1/2}_{r_c=0.5,\alpha=0.1}$	**2.955663**	$\langle r_n^2\rangle^{1/2}_{r_c=0.5,\alpha=0.1}$	**3.512850**
$\langle r_p^2\rangle^{1/2}_{r_c=0,\alpha=0}$	**2.955916**	$\langle r_n^2\rangle^{1/2}_{r_c=0,\alpha=0}$	**3.525076**
$\langle r_p^2\rangle^{1/2}_{exp}$ [23]	**2.95**	$\langle r_n^2\rangle^{1/2}_{exp}$ [23]	**3.53±0.17**
$\langle r_p^2\rangle^{1/2}_{FC's}$	**-0.0002**	$\langle r_n^2\rangle^{1/2}_{FC's}$	**-0.012**
Exotic nuclei ^{9}C			
Proton size parameter	**b_p=1.85 fm**	**Neutron size parameter**	**b_n=1.77fm**
$\langle r_p^2\rangle^{1/2}_{r_c=0.5,\alpha=0.1}$	**2.681358**	$\langle r_n^2\rangle^{1/2}_{r_c=0.5,\alpha=0.1}$	**2.258469**
$\langle r_p^2\rangle^{1/2}_{r_c=0,\alpha=0}$	**2.677457**	$\langle r_n^2\rangle^{1/2}_{r_c=0,\alpha=0}$	**2.242334**
$\langle r_p^2\rangle^{1/2}_{exp}$ [24]	**2.684**	$\langle r_n^2\rangle^{1/2}_{exp}$	**-**
$\langle r_p^2\rangle^{1/2}_{FC's}$	**-0.003**	$\langle r_n^2\rangle^{1/2}_{FC's}$	**-0.016**

Table 2. bc and bv parameters used in the current study's two function shell model (TFSM), in addition to computed and experimental data rms radii of ^{26}F and ^{9}C halo nuclei.

Halo nuclei	**Core nuclei**	**b_c (fm)**	**b_v (fm)**	**b_m (fm)**	***rms* matter radii for core nuclei $\langle r^2\rangle_c^{1/2}$ (fm)**		***rms* matter radii for halo nuclei $\langle r^2\rangle_m^{1/2}$ (fm)**	
					Calculated results	Experimental Data	Calculated results	Experimental Data
^{26}F	**^{24}F**	1.93	3.649	2.025	3.028205	3.03 ± 0.06 [22]	3.23719	3.23 ± 0.13 [23]
^{9}C	**^{7}Be**	1.76	3.47	1.78	2.311942	2.31 ± 0.02 [24]	2.422160	2.42 ± 0.03 [24]

A. Exotic nuclei ^{26}F

The nucleus ^{26}F is the first observed case of a neutron halo in 1979, and is unstable with respect to β-decay, with a half-life time ($\tau_{1/2}$ =8.2 *ms*) and neutron separation energy (S_{2n} = 5.04 *MeV*). The halo nucleus ^{26}F (J^{π},T =1^{+},4) is formed by coupling the core ^{24}F (J^{π} ,T= 3^{+},3) with the valence (halo) two neutron (J^{π} ,T=0^{+},1) [25-26]. The blue curve represents 2BNDD's for the core nuclei ^{24}F (proton + neutron) with oscillator size parameter (b_c =1.93 *fm*). The green curve represents 2BNDD's for valence (two neutrons) for ^{26}F nuclei with oscillator size parameter (b_v=3.649 *fm*), while the red solid curve represents the total calculation for the core nucleons and the valence two neutrons, and the shaded curve represents the experimental of nucleon densities of ^{26}F [23]. Figure (1) shows the computed matter density distributions show long tail for all of these nuclei and shows that the halo phenomenon and the long tail in ^{26}F is connected to the outer two neutrons for nucleon densities but not to the core nucleons, which is consistent with the experimental data [23], we have a long tail that agrees with the experimental data.

Figure (2) illustrates a calculated of the matter density distributions of neutron-rich ^{26}F (red curve) with the matter density distributions of the stable nuclei ^{19}F (yellow curve) by using two –body charge density distributions with effect of short range (r_c= 0.5*fm*) and tensor force (α = 0.1), we shown along tail is clearly in the matter distribution of the halo nuclei.

The neutron (blue curve), proton (brown curve), and matter (red curve) show densities of ^{26}F we show in Figure (3).

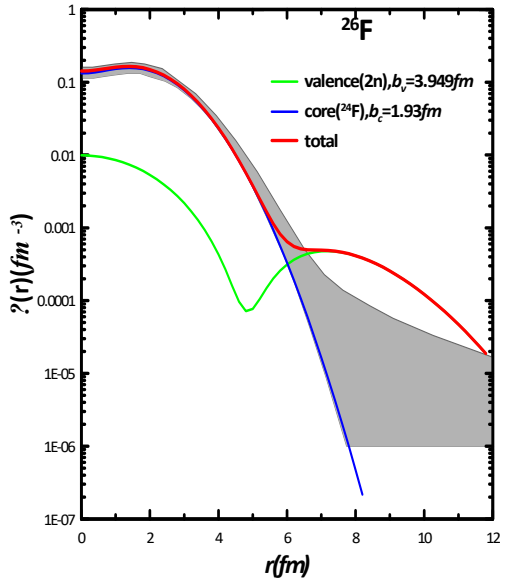

Figure 1. Core, valence and matter density distributions of (^{26}F)

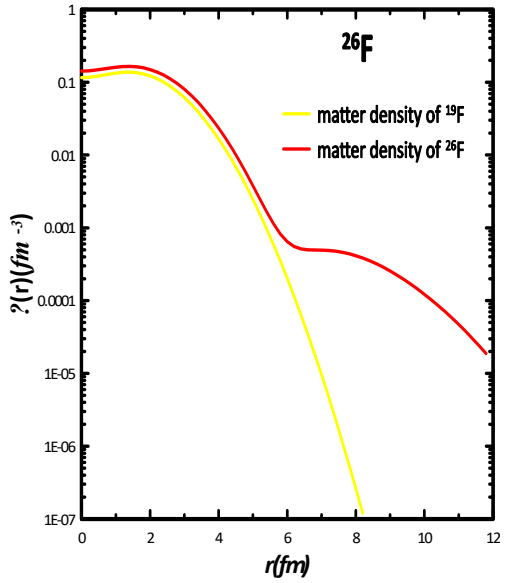

Figure 2. Calculated matter density distribution of neutron-rich (^{26} F) with that of stable nuclei (^{19}F)

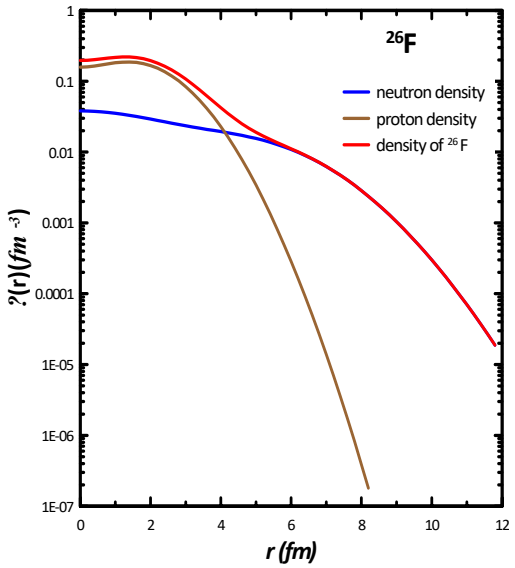

Figure3. Proton, neutron, and matter densities were calculated for ^{26}F halo nuclei

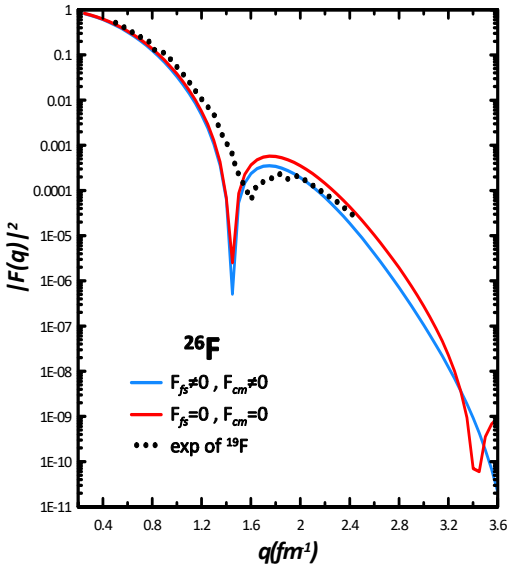

Figure 4. Elastic scattering electron form factor for ^{26}F with experimental data [27].

The neutron *rms* radius is found to be more than the proton *rms* radius, the neutron diffuseness is greater than the proton diffuseness in ^{26}F, and there is a considerable density differential between neutron and proton in ^{26}F, The typical behavior of the halo nucleus (the long tail) is clearly seen in the two neutron for ^{26}F distributions (blue curve), as shown in these figure. We note that the difference between the radii of the neutron and the proton is (r_n-r_p= 0.5571 *fm*) for ^{26}F. This difference is also supported by the halo structure for these alien cores.

Figure (4) presents the electron form factor for ^{26}F with FC'S using PWBA. Where the average radii of nuclei (b=2.025*fm*) were used, these values were adopted by comparing $\langle r^2 \rangle_{\exp}^{1/2}$ with $\langle r^2 \rangle_{the}^{1/2}$ we get a match with the experimental data. The blue curve represents the form factor of 2BCDD's with finite nucleon size corrected and center of mass correction ($F_{fs}(q) \neq 0$,$F_{cm}(q) \neq 0$) , the red curve represents the form factor of 2BCDD's with ($F_{fs}(q)$=0 , $F_{cm}(q)$=0) and the circle-packed are experimental data for stable nuclei ^{19}F [27]. We obtain the Form factors are not dependent on the neutrons that make up the halo but rather results from a difference in the proton density distribution of the last proton in the nuclei, obtain good form factors at the momentum for q<3.6 *fm* and we note that the behavior of the theoretical results for halo nuclei (^{26}F) matches the practical results for stable nuclei (^{19}F).

B. Exotic nuclei ^{9}C

The proton-halo nucleus ^{9}C is an interesting candidate with ($\tau_{1/2}$=126.5 *ms*) for studying the existence of two-proton halo because of the borromean structure and small two-proton separation energy (S_{2p}= 1.436 *MeV*) [25, 26]. ^{9}C (J^{π},T= 3/2, 3/2) is composed of a core ^{7}Be (J^{π}, T = 3/2^{-}, 3/2) with ($\tau_{1/2}$=53.22 *d*) and outer two loosely bound protons (J^{π}, T = 0^{+}, 1) surrounding the core to form the ^{9}C nucleus halo.

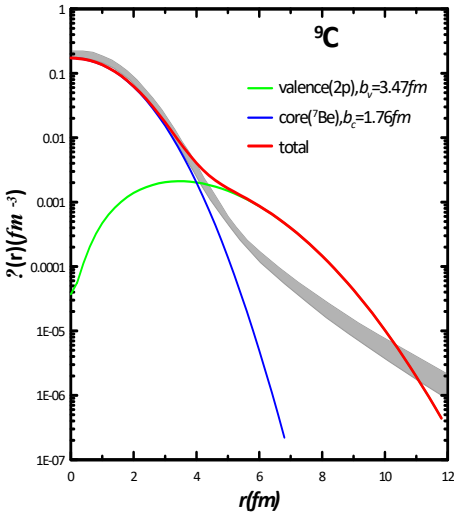

Figure 5. Core, halo and matter density distribution of (^{9}C)

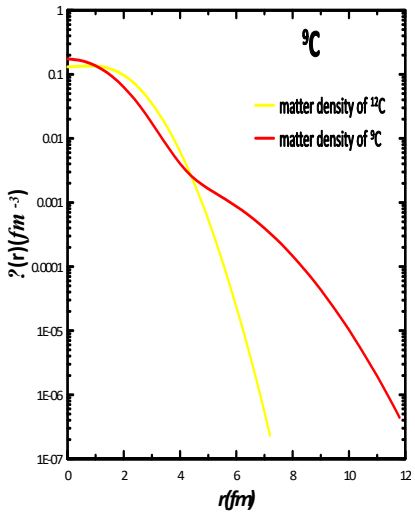

Figure 6. Calculated matter density distribution of proton –rich (^{9}C) with that of stable nuclei (^{12}C)

Figure (5) shows the relation between 2BNDD's (in fm^{-3}) of the ground state and r (in *fm*) With including short range effect (r_c= 0.5 *fm*) and tensor force effect (α =0.1) for ^{9}C nuclei. The blue curve represents 2BNDD's for the core ^{7}Be (proton + neutron) with oscillator size parameter (b_c=1.7 *fm*). The green curve represents 2BNDD's for valence (two proton) for ^{9}C nuclei with oscillator size parameter (b_v=3.47 *fm*), while red solid curve represents the total calculation for the core nucleons and the two valance protons, and the shaded curve represents the experimental [24], we have a long tail that agrees well with the experimental results.

Figure (6) illustrates a calculated matter density distributions of proton-rich ^{9}C (red line) with the matter density distributions of the stable nuclei ^{12}C (yellow line) by using 2BCDD's, we shown along tail is clearly in the matter distribution of the halo nuclei.

The neutron (blue curve), proton (brown curve), and matter (red curve) show densities of ^{9}C we show in Figure (7). It is observed that the proton *rms* radius is more than the neutron *rms* radius, that the proton diffuseness is greater than the neutron diffuseness in ^{9}C, and that there is a significant density differential between the proton and neutron in ^{9}C. The typical behavior of the halo nucleus (the long tail) is clearly seen in the two proton for ^{9}C distributions (brown curve), as shown in these figure. We note that the difference between the radii of the neutron and the proton is (r_p -r_n = 0.42288 *fm*) for ^{9}C. This difference is also supported by the halo structure for these alien cores.

Figure (8) presents the electron form factor for ^{9}C with FC'S using PWBA. Where the average radii of nuclei (b=1.78*fm*) were used, these values were adopted by comparing $\langle r^2 \rangle_{\exp}^{1/2}$ with $\langle r^2 \rangle_{the}^{1/2}$ we get a match with the experimental data. The blue curve represents the form factor of 2BCDD's with finite nucleon size corrected and center of mass correction (F_{fs}(q) ≠0, $F_{cm}(q)$ ≠0), the red curve represents the form factor of 2BCDD's with (F_{fs}(q)= 0, $F_{cm}(q)$ =0), and the circle-packed are experimental data for stable nuclei ^{7}Be [27]. It is clear that the form factor is dependent

on the detailed properties of the two proton halo and the difference in which depends on the mass number and the size parameter b_m ,obtain good form factors at the momentum for q<3.6 *fm* and we note that the behavior of the theoretical results for halo nuclei (^{9}C) matches the practical results for stable nuclei (^{12}C).

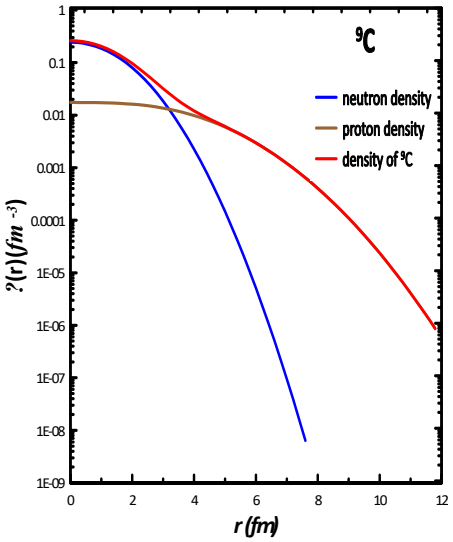

Figure 7. Proton, neutron, and matter densities were calculated for ^{9}C halo nuclei

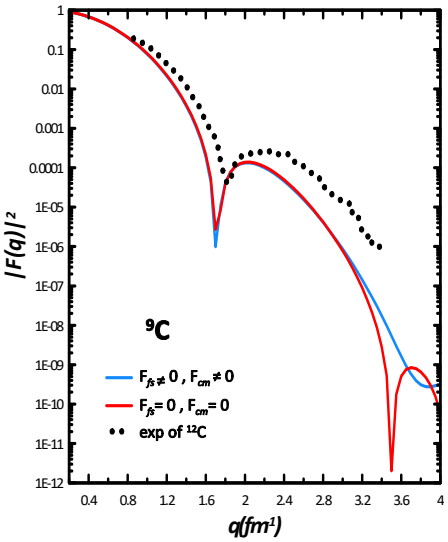

Figure 8. Elastic scattering electron form factor for ^{9}C with experimental data [27]

4. CONCLUSIONS

The measured matter density for our exotic nuclei using the framework of two body nucleon density distribution with effects of tensor force and short range with two different oscillator size parameters *bc* and *bv* showed a long tail behavior. The calculated proton and neutron distributions, density of matter and *rms* radii, are based on the halo nuclei ^{26}F and ^{9}C. The charge density distributions are joined with the PWBA to studied the form factors for these nuclei. The considerable difference in charge form factors between unstable nuclei (^{26}F and ^{9}C) and their stable isotopes (^{19}F and ^{12}C) is attributable to an increase in proton concentrations in the peripheral area.

ORCID IDs

Abeer A.M. Hussein, https://orcid.org/0000-0003-0068-1347; **Ghaith N. Flaiyh,** https://orcid.org/0000-0001-9918-4484

REFERENCES

[1] M. Hongo, and D. Thanh Son ,"Universal Properties of Weakly Bound Two-Neutron Halo Nuclei", Phys. Rev. Lett. **128**, 212501 (2022). https://doi.org/10.1103/PhysRevLett.128.212501

[2] A.N. Antonov, P.E. Hodgson, and I.Zh. Petkov, *Nucleon Momentum and Density Distributions in Nuclei*, (Clarendon Press, Oxford, 1988), pp. 97-102.

[3] I. Tanihata, H. Savajols, and R. Kanungo, "Recent experimental progress in nuclear halo structure studies", Progress in Particle and Nuclear Physics, **68**, 215–313 (2013).

[4] H. Bethe, B.H. Brandow, and A.G. Petschek, "Reference spectrum method for nuclear matter", Phys. Rev. **129**(1), 225-264 (1963). https://doi.org/10.1103/PhysRev.129.225

[5] G.E. Brown, and T.T.S. Kuo, "Structure of finite nuclei and the free nucleon-nucleon interaction", Nucl. Phys. A, **92**(3), 481-494 (1967). https://doi.org/10.1016/0375-9474(67)90627-6

[6] F. Dellagiacoma, G. Orlandiniand, and M. Traini, "Dynamical correlations in finite nuclei: A simple method to study tensor effects", Nucl. Phys. A, **393**(1), 95-108 (1983). https://doi.org/10.1016/0375-9474(83)90066-0

[7] I. Tanihata. J. Phys. G: Nucl. Part. Phys. **22**, 157 (1996). https://doi.org/10.1088/0954-3899/22/2/004

[8] P.G. Hansen, A.S. Jensen, and B. Jonson, Ann. Rev. Nucl. Part. Sci. **45**, 591 (1995). https://www.annualreviews.org/doi/pdf/10.1146/annurev.ns.45.120195.003111

[9] G.M. Sallh, and A.N. Abdullah, Iraqi Journal of Science, **62**(8), 2555-2564 (2021). https://doi.org/10.24996/ijs.2021.62.8.8

[10] Arkan R. Ridha, Wasan Z. Majeed, Iraqi Journal of Science, **63**(3), 977-987 (2022). https://doi.org/10.24996/ijs.2022.63.3.7

[11] B.Q. Chen, Z.Y. Ma, F. Grümmer, and S. Krewald, "Relativistic mean-field theory study of proton halos in the 2s1d shell", J. Phys. G: Nucl. Part. Phys. **24**, 97 (1998). https://doi.org/10.1088/0954-3899/24/1/013

[12] Z. Ren, A. Faessler, and A. Bobyk, "Relativistic mean-field description of a proton halo in the first excited (1/2)+ state of 17F", Phys. Rev. C, **57**, 2752 (1998). https://doi.org/10.1103/PhysRevC.57.2752

[13] A.K. Hamoudi, G.N. Flaiyh, and A.N. Abdullah, "Study of Density Distributions, Elastic Electron Scattering form factors and reaction cross sections of ^{9}C, ^{12}N and ^{23}Al exotic nuclei", Iraqi Journal of Science, **56**(1A), 147-161 (2015). https://www.iasj.net/iasj/download/e5ff2f1a46127a57

[14] K.P. Anjali, K. Prathapan, and R.K. Biju, Braz. J. Phys. **50**, 298 (2020). https://doi.org/10.1007/s13538-020-00750-1

[15] A.N. Antonov, P.E. Hodgson, and I.Zh. Petkov, "Nucleon Momentum and Density Distribution in Nuclei", Z. Physik A, **297**, 257–260 (1980). https://doi.org/10.1007/BF01892806

[16] R.D. Lawson, *Theory of the Nuclear Shell Model*, (Clarendon Press, Oxford, 1980).
[17] A.K. Hamoudi, R.A. Radhi, G.N. Flaiyh, and F.I. Shrrad, "The effect of two body Correlations on the charge density distributions and elastic electron scattering form factors for some 2s-1d shell nuclei", Journal of Al-Nahrain University, **13**, 88-984 (2010). https://www.iasj.net/iasj/download/d9ae0c35e9ff9031.
[18] J. Fiasi, A. Hamoudi, J.M. Irvine, and F. Yazici, J. Phys. G: Nucl. Phys. **4**, 27 (1988). https://doi.org/10.1088/0305-4616/14/1/007
[19] S. Sugimoto, K. Lkeda, and H. Toki, "Study of the effect of the tensor correlation on the alpha-alpha interaction in 8Be with charge and parity projected Hartree-Fock method", Nucl. Phys. A, **789**, 155-163 (2007). https://doi.org/10.1016/j.nuclphysa.2007.04.004
[20] T.T.S. Kuo, and G.E. Brown, "Structure of finite nuclei and the free nucleon-nucleon interaction: An application to ^{18}O and ^{18}F". Nucl. Phys. A, **85**, 40-86 (1966). https://doi.org/10.1016/0029-5582(66)90131-3
[21] A.N. Abdullah, Int. J. Mod. Phys. E, **29**, 2050015 (2020). https://doi.org/10.1142/S0218301320500159
[22] J.D. Walecka, *Electron Scattering for Nuclear and Nucleon Structure*, (Cambridge University Press, Cambridge, 2001), pp. 3112.
[23] A. Ozawa, T. Suzuki, and I. Tanihata, "Nuclear size and related topics", Nucl. Phys. A, **693**, 32–62 (2001). https://doi.org/10.1016/S0375-9474(01)01152-6
[24] S. Ahmad, A.A. Usmani, and Z.A. Khan, Phys. Rev. C, **96**, 064602 (2017). https://doi.org/10.1103/PhysRevC.96.064602
[25] R.E. Warner, F. Carstoiu, J.A. Brown, F.D. Becchetti, D.A. Roberts, B. Davids, M. Horoi, et al, "Reaction and proton-removal cross sections of ^{6}Li, ^{7}Be, ^{10}B, ^{9,10,11}C, ^{12}N, ^{13,15}O, and ^{17}Ne on Si at 15 to 53 MeV/nucleon", Phys. Rev. C, **74**, 014605 (2006). https://doi.org/10.1103/PhysRevC.74.014605
[26] G. Audi, F.G. Kondev, M. Wang, W.J. Huang, and S. Naimi, Chin. Phys. C, **41**, 030001 (2017). https://doi.org/10.1088/1674-1137/41/3/030001
[27] H. Rui, L. Jia-Xing, Y. Jian-Ming, J. Juan-Xia, W. Jian-Song, H. Qiang, Chain. Phys. Lett. **27**(9), 092101 (2010). https://doi.org/10.1088/0256-307X/27/9/092101
[28] H. De Vries, C.W. Jager, and C. De Vries, "Nuclear charge-density-distribution parameters from elastic electron scattering", Atomic Data and Nuclear Data Tables, **36**(3), 495-536 (1987). https://doi.org/10.1016/0092-640X(87)90013-1

ТЕОРЕТИЧНЕ ДОСЛІДЖЕННЯ РОЗПОДІЛУ ГУСТИНИ МАТЕРІЇ ТА ФОРМ-ФАКТОРІВ ПРУЖНОГО РОЗСІЮВАННЯ ЕЛЕКТРОНІВ ЕКЗОТИЧНИХ ЯДЕР (^{26}F ТА ^{9}C)

Абір А. М. Хусейн, Гейт Н. Флей

Факультет фізики, Науковий коледж, Багдадський університет, Багдад, Ірак

Розподіл ядерної густини, середньоквадратичних радіусів і форм-фактори пружного розсіювання електронів розраховано для ядер (^{9}C) (ядро +2p) і (^{26}F) (ядро +2n) з двома різними параметрами ядерного потенціалу для (*bc*) і (*bv*), де використовуються кореляції для обох ефектів (тензорної сили і короткодії), і спостерігається поява довгого розширення в розподілах ядерної густини для цих ядер. Fortran 95 використовувався для програмування ядерних властивостей, таких як густина нуклонів (матерії, нейтронів і протонів), форм-факторів пружного розсіювання електронів і середньоквадратичних радіусів. Визначено, що результати обчислень для цих екзотичних ядер досить добре відповідають експериментальним даним.

Ключові слова: *екзотичні ядра; форм-фактор; ядерна щільність (нейтрон, протон, речовина); багатонейтронні ядра, багатопротонні ядра*

East European Journal of Physics. 1. 89-93 (2023)
DOI:10.26565/2312-4334-2023-1-10 ISSN 2312-4334

FP SHELL EFFECTIVE INTERACTIONS AND NUCLEAR SHELL STRUCTURE OF ^{44}Sc[†]

Maryam K. Hassan*, Firas Z. Majeed
Department of Physics, College of Science, Baghdad University, Baghdad, Iraq
**Corresponding author e-mail: mariam.kameel1204a@sc.uobaghdad.edu.iq*
Received January 5, 2023; accepted January 20, 2023

Nuclear energy levels in ^{44}Sc isotope, with fp shell model space occupation low levels fp-LS shell within shell model calculations had been investigated. The interactions have been used to calculate the nuclear energy levels which are fpd6, hw, fpy**,** with fp shell model space, d3f7cospn for 1d3/21f7/2 model space. The results are compared with each other and with available experimental data, its agreement with some results is clear. The used of model space interactions is the best fitted two body matrix elements in fp shell model space beside the good agreements in the reproduced values of energy levels scheme. The general estimation of the reproduced data is good especially below 3MeV. All inscriptions are given in diagrammatic notation, the wave vectors and analysis are modeled in the so-called diagrammatic notation. The potential of oscillator is utilized to construct single particle vector, considering $^{40}_{20}\mathbf{Ca}_{20}$ as a core for fp shell model space and $^{32}_{16}\mathbf{S}_{16}$ as an inert core for the model space d3f7. The OXFORD BEUNES AIRES SHELL MODEL CODE is utilized to accomplish the results for all tested nuclei.
Keywords: *Nuclear energy levels; Scandium isotope ^{44}Sc; Nuclear reaction; Diagrammatic notation; FPD6pn*
PACS: 21.10._k, 21.60._n, 21.60.Cs

1. INTRODUCTION

Many studies have been performed to understand the nuclear properties and the internal structure of nuclei. Due to the complex nature of nuclei, there is no unified theory to describe their behaviors, properties, and structures [1]. The shell theory has many benefits and properties, such as the model independence suggested, the applied physical N-N potential, besides the traditional Hamiltonian related to different categories of eigenvectors, and plenty of nuclei. The shell theory is still relevant and provides the primary theoretical methods for realizing all measurable nuclei [1]. Excitation energies, binding energies, and spectroscopic factors were calculated in the LS shell ($1f_{5/2}$, $2p_{3/2}$, $2p_{1/2}$) space so as to acquire effective N-N matrix elements [2].

The presence of an orbital distance at N = 32 in isotope-rich neutrons localized in the nearby magic nucleus ^{48}Ca was inspired by interactions between PN [3]. Filled pf-LS shell model inspections of A=48 nuclei were performed [4], and Kuo-Brown (KB) [10] to KB1 and KB3G were modified. The isobaric chains A = 50, A = 51, and A = 52 were studied [5] using KB3G, FPD6, and their released version, KB3G [6]. The shell theory established an important method for conducting such research. In this hypothesis, realistic potentials are founded, and the basis vectors are denoted by exact quantum numbers of angular momentum (J), isospin (T), and parity (π) [7]. Plenty of research [8] was done to detect the distribution of Eigen functions and construct the framework of the shell model [9].

Independently by Maria Mayer and by Jensen, Haxel, and Suess) in the 1950s, the nuclear shell theory has been regarded as a major theory in the understanding of nuclear structure [10]. Due to extreme single-particle motion in spherical symmetry, only the addition of strong spin-orbit terms was invoked to permit the redesign of a wide range of results for isotopes near the nuclear magic numbers [11]. Calculations had been accomplished in model space of full fp-*LS* shell contains $1f_{7/2}$, $1f_{5/2}$, $2p_{3/2}$, $2p_{1/2}$ subshell and considering ^{40}Ca as a core. The number of particles that can be excited to higher configurations is not restricted. Thus, apart from testing the suitability of GXPF1A interaction in explaining the experimental data, a comparison of results with that of his results would also throw light on the role of intruder $g_{9/2}$ orbital, appropriate choice of core, and the effect of truncation on the particles to be excited [12].

Nuclear energy levels, total angular momenta, and even-even parity for nucleons present outside closed and no core for (^{42}Ca, ^{44}Ca, ^{46}Ca and ^{48}Ca), which occupied fp-shell ($1f_{7/2}$, $1f_{5/2}$, $2p_{3/2}$, $2p_{1/2}$), within shell model calculations were intriguing. Four interactions had been assigned to calculate the nuclear energy spectrum of ^{42}Ca, ^{44}Ca, ^{46}Ca and ^{48}Ca. The results of the FPD6, GXPF1, and KB3G interactions are compared with each other and with available experimental data. Code OXBASH had been utilized to generate model space wave vectors and at the same time receive the comparable model space effective interaction that was selected for this study.

This work aims to reproduce the nuclear energy levels of the (^{44}Sc) isotope, utilizing FPD6pn as a model space effective interaction to generate model space vectors. The calculations are performed using the OXBASH code [14]. The calculated energy levels for the isotopes under study with a different set of effective interactions will be compared with the available experimental data.

2. THEORY

The ground state of the core and two extra nucleons system is described by a minimum of the total energy. Generally, the two extra nucleons are then in the lowest available single-particle orbit ρ and are coupled to that value of the total spin

[†] ***Cite as***: M.K. Hassan, and F.Z. Majeed, East Eur. J. Phys. **1**, 89 (2023), https://doi.org/10.26565/2312-4334-2023-1-10

and isospin Γ for which $E_{\Gamma}^{(1)}(\rho^2)$ assumes its minimum value. All other states, in which the two particles are coupled to different values of Γ or when one or both of the extra nucleons are excited into a different single-particle orbit, represent excited states. The Hamiltonian of the core-plus-two-nucleon system can be split into two terms as in eq. (1) [15]:

$$H = H_{core} + H_{12}, \tag{1}$$

with

$$H_{core} = \sum_{k=3}^{A}[T(k) + U(k)] + [\sum_{3=k<l}^{A} W(k,l) - \sum_{k=3}^{A} U(k)], \tag{2}$$

$$H_{12} = \sum_{k=1}^{A}[T(k) + U(k)] + [\sum_{k=1}^{2}\sum_{l=3}^{A} W(k,l) + W(1,2) - \sum_{k=1}^{2} U(k)]. \tag{3}$$

where H_{core} refers to the interaction between the core particles (labeled by k=3, …, A). Assuming that the closed-shell core is inert, then the contribution of H_{core} to the total energy is a constant. H_{12} describes the contribution from the two additional particles. It can be written more specifically as [15].

$$H_{12} = H_{12}^{(0)} + H_{12}^{(1)}. \tag{4}$$

where $H_{12}^{(0)}$ Specifies the single-particle Hamiltonion given by

$$H_{12}^{(0)} = [T(1) + U(1)] + [T(2) + U(2)] = H_{s.p.}(1) + H_{s.p.}(2) \tag{5}$$

A and $H_{12}^{(1)}$ denotes the residual interaction and it is given by

$$H_{12}^{(1)} = [\sum_{l=3}^{A} W(1,l) - U(1)] + [\sum_{l=3}^{A} W(2,l) - U(2)] + W(1,2) \tag{6}$$

If we now take

$$U(k) = \sum_{l=3}^{A} W(k,l) \text{ for } k= 1, 2, \tag{7}$$

The single-particle terms in the residual interaction $H_{12}^{(1)}$ exactly vanish and only the two-particle term $W(1, 2)$ survives. In other words, the residual interaction is given by $H_{12}^{(1)} = W(1,2)$, where $W(1, 2)$ does not contain any single-particle terms. The definition in eq. (7) with the summation over all particles of the core implies that the single-particle states are defined with respect to the core nucleus. The general derivation of a self-consistent single-particle potential U is given in the Hartree-Fock theory. The later approximation, is so complex, so it will not be discussed here, however. In most shell-model calculations one makes the approach that the single-particle potential can be represented using the mathematical simple harmonic-oscillator or the Saxon-Woods potential. In that case $H_{12}^{(1)}$ is no longer equal to $W(1, 2)$. It is assumed now that for such a simplified single-particle potential U, the residual interaction, as given in eq. (6), still can be represented by a two-body interaction. The residual two-body interaction from now on, will be specified by $\sum_{i<j} V(i,j)$. Thus, in the case of two active particles outside a core one has [15]:

$$H_{12}^{(1)} = V(1,2). \tag{8}$$

From eqs. (3), (4), (5) and (6) it can be written for the total Hamiltonian:

$$H = H_{core} + H_{s.p.}(1) + H_{s.p.}(2) + V(1,2). \tag{9}$$

The binding energy of the nucleus with two particles outside the core in the orbit ρ and coupled to spin and isospin Γ is given by the expectation value [15]:

$$E_{\Gamma}^{b}(A) = \left\langle \Phi_{\Gamma}^{(0)}(1, \dots, A) \middle| H \middle| \Phi_{\Gamma}^{(0)}(1, \dots, A) \right\rangle. \tag{10}$$

The total Hamiltonian in the state $\Phi_{\Gamma}^{(0)}(1, \dots, A)$ of the complete nucleus, the wave function $\Phi_{\Gamma}^{(0)}(1, \dots, A)$ can be written as the antisymmetrized product of the core wave function, Φ_{00}(core), and the wave function $\Phi_{\Gamma}^{(0)}(1, 2)$ describing the extra two nucleons [15]:

$$\Phi_{\Gamma}^{(0)}(1, \dots, A) = \mathcal{A}\{\Phi_{00}(\text{core})\Phi_{\Gamma}^{(0)}(1,2)\}. \tag{11}$$

The function Φ_{00} (core) and $\Phi_{\Gamma}^{(0)}(1,2)$ are considered to be antisymmetric in the particles 3, …, A and 1, 2, respectively. The antisymmetrizer $\mathcal{A}$ must complete the antisymmetrization for all particles by permuting particle coordinates and taking appropriate linear combinations. For the evaluation of the matrix element in eq. (11), the correct results are also obtained with the simpler product function Φ_{00} (core)$\Phi_{\Gamma}^{(0)}(1,2)$. Since in eq. (11) the total Hamiltonian has been decomposed into terms that operate on either particles 1, 2 or particles 3, A, one obtains from the orthonormality of the wave function Φ_{00} (core) and $\Phi_{\Gamma}^{(0)}(1,2)$ [15]:

$$\left\langle \Phi_{00}(core)\Phi_{\Gamma}^{(0)}(1,2)\middle|H\middle|\Phi_{00}(\text{core})\Phi_{\Gamma}^{(0)}(1,2)\right\rangle = \langle \Phi_{00}(core)|H_{core}|\Phi_{00}(core)\rangle +$$

$$\left\langle \Phi_{\Gamma}^{(0)}(1,2)\middle|H_{s.p.}(1) + H_{s.p.}(2)\middle|\Phi_{\Gamma}^{(0)}(1,2)\right\rangle + \left\langle \Phi_{\Gamma}^{(0)}(1,2)\middle|V(1,2)\middle|\Phi_{\Gamma}^{(0)}(1,2)\right\rangle. \quad (12)$$

The coupled two-particle wave function $\Phi_{\Gamma}(1.2)$ can be defined as in the following eqs [15].

$$\Phi_{JM}(j_a(1)j_b(2)) = \sum_{m_a m_b}\langle j_a m_a j_b m_b|JM\rangle\, \emptyset j_a m_a(1)\, \emptyset j_b m_b(2) \quad (13)$$

$$\Phi_{JM}^{\pm} = \sqrt{\frac{1}{2}}(1 \pm P_{12})\Phi_{JM}(j_a(1)j_b(2)) = \sqrt{\frac{1}{2}}\{\Phi_{JM}(j_a(1)j_b(2)) \pm (-1)^{J-j_a-j_b}\Phi_{JM}(j_b(1)j_a(2))\}. \quad (14)$$

For the evaluation of the matrix element of $H_{s.p.}(1)$ in eq. (12) one can integrate out the coordinates of particle 2, and the same for $H_{s.p.}(2)$ the coordinates of particle 1. Because of orthonormality of Clebsch-Gordan coefficients the matrix elements each reduce to expectation values of $H_{s.p.}$ for single-particle eigenstates, e_ρ. Eq. (12) is seen to be identical to eq. (12) with the single-particle energies given by [15]

$$2e_\rho = \left\langle \Phi_{\Gamma}^{(0)}(1,2)\middle|H_{s.p.}(1) + H_{s.p.}(2)\middle|\Phi_{\Gamma}^{(0)}(1,2)\right\rangle = \left\langle \rho^2\middle|H_{12}^{(0)}\middle|\rho^2\right\rangle_{\Gamma}. \quad (15)$$

The residual interaction is given by [15]

$$E_{\Gamma}^{(1)}(\rho^2) = \left\langle \Phi_{\Gamma}^{(0)}(1,2)\middle|V(1,2)\middle|\Phi_{\Gamma}^{(0)}(1,2)\right\rangle = \langle \rho^2|V(1,2)|\rho^2\rangle_{\Gamma}, \quad (16)$$

and the binding energy of the core given by [15].

3. RESULTS AND DISCUSSION

Microscopic models have been introduced to constitute nuclear energy states. The model with mixed multi-nucleon conformations is one of the most important models. In the adopted method, the systems ^{40}Ca and ^{32}S are considered non-active cores with extra-active baryons (neutrons only) that are named the LS shell. Calculations of the shell model are carried out within a model space in which the nucleons are free to occupy a few orbits and are able to reproduce the measured static moments and transition strengths [16, 20].

The shell theory is an important theoretical topic for microscale calculations of nucleus buildup and is a major part of nuclear theory. The essential assumption in the shell model is that every particle plays separately in a potential average, including a dominant non-central spin-orbit part and the baryons themselves. After this, the baryons allied into classes, the "shells," distant from each other. By this approach, the nucleus is divided into an inert core made up of filled LS shells plus a certain number of valence nucleons called the valence body [16]. Energy level values in this work are calculated by the shell model calculations that are performed via the computer code OXBASH [14].

From Figure 1 which represents the energy level scheme for ^{44}Sc it is clear that there are a specific differences between the calculated and experimental results in general, the calculated results reveals that there are an energy gap between $J_k^{\pi} = 0_1^+$ and $J_k^{\pi} = 4_2^+$ by the value of $\Delta E = 3MeV$ but this state has a well defined value as compared with the experimental one and the state $J_k^{\pi} = 2_2^+$ has a fair agreement with experiment but the higher the states the wider the difference with the laboratory states, in the case of the interaction d3f7cospn he resulted scheme with fine structure spectrum as a result of large number of active particles in a narrow space with an energy spacing $\Delta E < 50\ KeV$ beside the existence of different parity states generated from different parity subshell orbits, the results in this case are far from the experimental scheme.

The function of energy levels and density will be very useful in identifying the energy spectrum and studying the distribution of states between 1 and 10 MeV. Nuclear shell theory is based on some reliable but not certain realistic assumptions, as well as a wide range of fitting parameters that are not well reproduced to generate static and dynamic nuclear properties, and must be readjusted to meet experimental requirements.

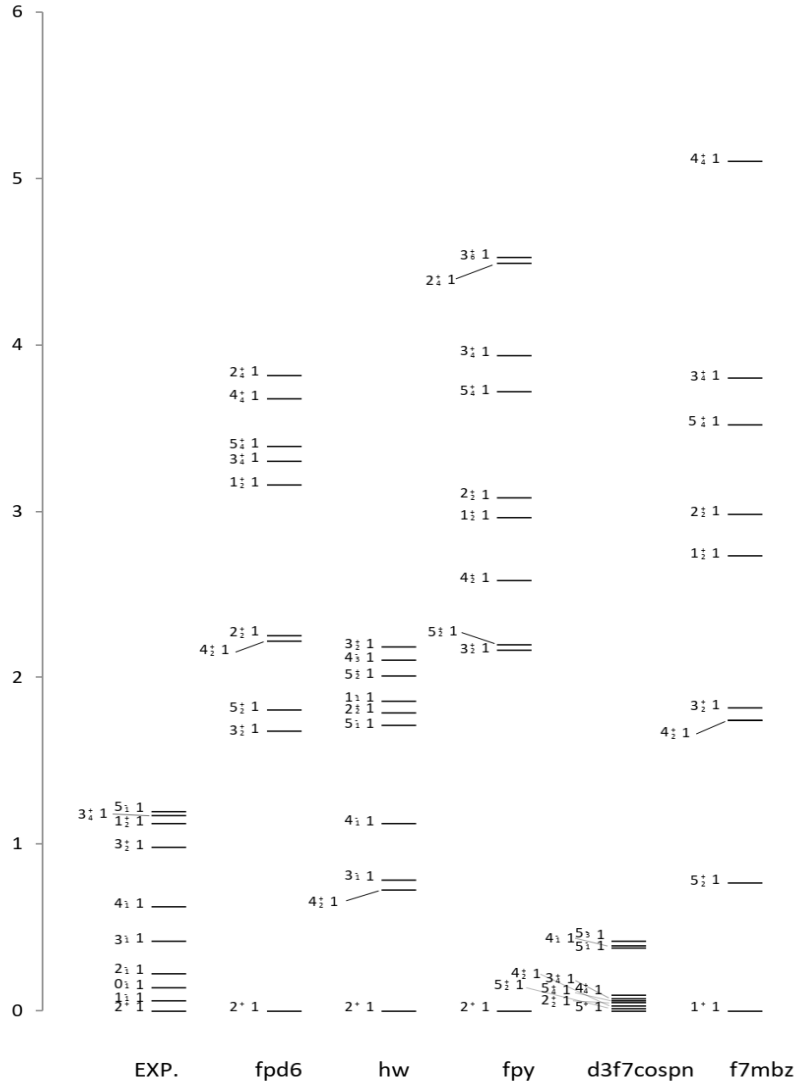

The energy levels scheme of ^{44}**Sc** by using **Fpd6**,**HW**,**FPY**, **D3F7COSPN** and **f7mbz**

Figure 1. The energy levels scheme of ^{44}**Sc** by using Fpd6, HW, FPY, D3F7COSPN, and f7mbz interactions with closed core ^{40}Ca for **(J_K^πT),** positive parity, ten orders

4. CONCLUSIONS

The results reflect that the interactions do not have the best contributions to the theoretical calculations if we remember that the fitting and adjustable parameters are extracted from adjustable two-body matrix elements in subshells gathering that pair. The reproduced data are good for even total spin values and bad for odd total spin values.

Acknowledgement

Thanks to Dr. B.A. Brown for his assistance in producing energy-level files from the OXBASH code.

ORCID IDs

Maryam K. Hassan, https://orcid.org/0000-0003-2060-4672; **Firas Z. Majeed,** https://orcid.org/0000-0001-6527-3913

REFERENCES

[1] M. Honma, T. Otsuka, B.A. Brown, and T. Minzusaki, "Effective interaction for pf-shell nuclei", Phys. Rev. C, **65**, 061301(R) (2002). https://doi.org/10.1103/PhysRevC.65.061301

[2] H. Crannell, R. Helm, H. Kendall, J. Oeser, and M. Yearian, "Electron-Scattering Study of Nuclear Levels in Cobalt, Nickel, Lead, and Bismuth", Phys. Rev. **123**(3), 923 (1961). https://doi.org/10.1103/PhysRev.123.923

[3] J.I. Prisciandaro, P.F. Mantica, B.A. Brown, D.W. Anthony, M.W. Cooper, A. Garcia, D.E. Groh, et al., "New evidence for a subshell gap at N=32", Phys. Lett. B, **510**, 17-23 (2001). https://doi.org/10.1016/S0370-2693(01)00565-2

[4] E. Caurier, and A.P. Zuker, Phys. Rev. C, **50**, 225 (1994). https://doi.org/10.1103/PhysRevC.50.225

[5] A. Poves, J. Sánchez-Solano, E. Caurier, and F. Nowacki, Nucl. Phys. A, **694**, 157 (2001). https://doi.org/10.1016/S0375-9474(01)00967-8

[6] W.A. Richter, M.G. Van Der Merwe, R.E. Julies, and B.A.Brown, Nucl. Phys. A**, 532**, 325 (1991). https://doi.org/10.1016/0375-9474(91)90007-S
[7] V. Zelevinsky, B.A. Brown, N. Frazier, and M. Horoi, Phys. Rep. **276**, 8 (1996). https://doi.org/10.1016/S0370-1573(96)00007-5
[8] R.R. Whitehead, A. Watt, D. Kelvin, and A. Conkie, Phys. Lett. B, **76**, 149 (1978). https://doi.org/10.1016/0370-2693(78)90262-9
[9] B.A. Brown, G. Bertsch, Phys. Lett. B, **148**(1-3), 5 (1984). https://doi.org/10.1016/0370-2693%2884%2991598-3
[10] J. Suhonen, *From Nucleons to Nucleus Concepts of Microscopic Nuclear Theory*, (Springer, Finland, 2006).
[11] R.D. Lawson, *Theory of the Nuclear Shell Model*, (Clarendon Press, Oxford, New York, 1980).
[12] L. Coraggio, A. Covello, N. Itaco, and T.T.S. Kuo, Prog. Part. Nucl. Phys. **62**, 135 (2009). https://doi.org/10.1016/j.ppnp.2008.06.001
[13] F.Z. Majeed, and S.S. Mashaan, Indian Journal of Natural Sciences, **9**, 50 (2018).
[14] B.A. Brown et al, OXBASH code, MSUNSCL Report 524 (1988).
[15] P.J. Brussaard, and P.W.M. Glademans, *Shell-model Applications in Nuclear Spectroscopy*, (North-Holland Publishing Company, Amsterdam, 1977).
[16] H. Sagawa, and X.Z. Zhang, "Evolution of Deformations in Medium-Mass Nuclei", Phys. Rev. C, **72**(5), 054311 (2005). https://doi.org/10.1103/PhysRevC.72.054311
[17] G. Audi, F.G. Kondev, Meng Wang, W.J. Huang, and S. Naimi, "The NUBASE2016 Evaluation of Nuclear Properties", Chinese Phys. C, **41**(3), 030001 (2017). https://doi.org/10.1088/1674-1137/41/3/030001
[18] A.A. Al-Rahmani, S.F. Kazem, "Elastic Electron-Nucleus Scattering Form Factors of Selected Medium Mass Nuclei", NeuroQuantology, **18**(8), 49-58 (2020). https://doi.org/14704/nq.2020.18.8.NQ20204
[19] A.H. Ali, **"**Investigation of the Quadrupole Moment and Form Factors of Some Ca Isotopes", Baghdad Science Journal, **17**(2), 0502 (2020). https://doi.org/10.21123/bsj.2020.17.2.0502
[20] L. Wang, J. Liu, R. Wang, M. Lyu, C. Xu, and Z. Ren, "Global analysis of nuclear cluster structure from the elastic and inclusive electron scattering", Phys. Rev. C, **103**, 054307 (2021). https://doi.org/10.1103/PhysRevC.103.054307
[21] B. Hernández, P. Sarriguren, O. Moreno, E. Moya de Guerra, D.N. Kadrev, and A.N. Antonov, "Nuclear shape transitions and elastic magnetic electron scattering", Phys. Rev. C, **103**, 014303 (2021). https://doi.org/10.1103/PhysRevC.103.014303

ЕФЕКТИВНІ ВЗАЄМОДІЇ ОБОЛОНКИ FP ТА СТРУКТУРА ЯДЕРНОЇ ОБОЛОНКИ ^{44}Sc

Мар'ям К. Хассан, Фірас З. Маджид
Факультет фізики, Науковий коледж, Багдадський університет, Багдад, Ірак

Було досліджено рівні ядерної енергії в ізотопі ^{44}Sc з моделлю fp-оболонки з низькими рівнями зайнятості простору fp-LS в рамках розрахунків моделі оболонки. Взаємодії були використані для розрахунку рівнів ядерної енергії, які є fpd6, hw, fpy, з моделлю простору оболонки fp, d3f7cospn для моделі простору 1d3/21f7/2. Результати порівнюються між собою та з наявними експериментальними даними, їх збіг з деякими результатами очевидний. Використання взаємодій простору моделі є найкраще підігнаними елементами матриці двох тіл у просторі моделі оболонки fp, окрім хороших узгоджень у відтворених значеннях схеми рівнів енергії. Загальна оцінка відтворених даних хороша, особливо нижче 3 МеВ. Усі написи подано у діаграмному записі, хвильові вектори та аналіз змодельовані також у так званому діаграмному записі. Потенціал осцилятора використовується для побудови вектора однієї частинки, розглядаючи $^{40}_{20}\mathbf{Ca}_{20}$ як ядро для моделі простору оболонки fp та $^{32}_{16}\mathbf{S}_{16}$ як інертне ядро для моделі простору d3f7. Код моделі оболонки OXFORD BEUNES AIRES використовується для отримання результатів для всіх перевірених ядер.

Ключові слова: *ядерні енергетичні рівні; ізотоп скандію ^{44}Sc; ядерна реакція; схематичні позначення; FPD6pn*

East European Journal of Physics. **1.** 94-101 (2023)
DOI:10.26565/2312-4334-2023-1-11 ISSN 2312-4334

VITRIFICATION OF A SIMULATOR OF VAT RESIDUES FROM LIQUID RADIOACTIVE WASTE†

Sergii Sayenko[a], Volodymyr Shkuropatenko[a]*, Yevhenii Svitlychnyi[a], Anna Zykova[a], Svitlana Karsim[a], Dmytro Kutnii[a], Volodymyr Morgunov[b]
[a]*National Science Center, Kharkiv Institute of Physics and Technology, Kharkiv, 61108, Ukraine*
[b]*V.N. Karazin Kharkiv National University, 4 Svobody Sq., Kharkiv, 61022, Ukraine*
**Corresponding Author: shkuropatenko@kipt.kharkov.ua*
Received January 10, 2023; revised January 20, 2023; accepted January 10, 2023

The study on the posibility of the use of the optimal glass compositions for vitrification of an imitator of vat residues of liquid radioactive waste from nuclear power plants with VVER-1000 reactors was carried out. The main process parameters such as vitrification temperature, strength, corrosion resistance, absence of crystalline phases, minimization of glass-forming additives and inclusion the maximum amount of waste were analyzed. It has been established that the melting temperature of lead-borosilicate glass matrices was 1150 °C, which satisfies the requirements for vitrification of low- and medium-level waste. The ultimate compressive strength of the obtained samples of glass matrices was 136.0 MPa. In addition, it has been shown that lead-borosilicate glass matrices are the most resistant to leaching. The cesium leaching rate was $1.5 \cdot 10^{-5}$ g/cm^2·day.
Keywords: *liquid radioactive waste; vat residue; vitrification; strength, leaching rate*
PACS: 28.41.Kw

INTRODUCTION

At present, the problem of environmental safety during the process of the radioactive waste immobilization is very challenging for further nuclear power industry development. It is well known that exploitation of nuclear power plants (NPPs) results in accumulation of liquid radioactive wastes (LRW) of low and middle activity. Ukrainian NPPs currently accumulate a large amount of LWR, represented by vat residues with a salt content of 200 to 600 g/l, salt melt with a higher salinity, spent filter materials and sludge. According to the rules for ensuring radiation safety, liquid radioactive waste cannot be transferred for long-term storage and disposal without additional processing. Various technologies for processing such types of waste to a state suitable for disposal are under consideration [1].

The most common and fairly cheap method of LRW conditioning is cementing [2, 3]. However, cement matrices are characterized by increased solubility in an aqueous medium, and the volume of final waste forms significantly increases [4]. Some authors argue that the most optimal method for solidifying LRW is inclusion in glass with subsequent burial in near-surface storage facilities [5, 6]. The prospect of using glass as a protective matrix is due to the high ability to include elements in its composition, regardless of their charge and atomic size, resistance to radiation damage, and proven production technology [7]. In addition, vitrification of waste reduces their volume by several times, and thus saves expensive storage space. The cost of disposal is very high, even in its simplest near-surface variant, which is used only for low- and medium-level short-lived nuclear waste. For example, in France, the cost of storing one cubic meter of low-and medium-level short-lived waste in a near-surface storage facility is about 2200 € [8].

The main problems of the vitrification method are associated with the use of high-temperature processes. In addition, the following difficulty arises during vitrification process: for radioactive waste with a variable composition, it is necessary to change the composition of the glass frit accordingly in order to obtain a sufficiently high-quality product. Since radioactive waste contains many different elements, their introduction into glass changes its parameters and affects its stability. Moreover, some components are practically not included in glass at their certain content in radioactive waste.

However, despite the above limitations, the vitrification method is considered as one of the promising methods for converting LRW into a solid state. The high stability of the glass, combined with a sufficiently large reduction in the volume of waste, encourages the use of LRW vitrification as an alternative to cementing. A significant advantage of vitrification is the fact that there are no significant restrictions on the concentration of salts in LRW, as well as on the content of organic materials and surfactants, compared with the use of cement.

Vitrification of radioactive waste, especially of high-level activity, has been carried out in several countries for almost 40 years. Teams of specialists from the United States, France, Russia, Great Britain, Belgium, and others are carrying out numerous works on the development and improvement of methods for the vitrification of radioactive waste [8–10]. However, research on the composition and long-term behavior of vitrified high and intermediate level wastes, mainly borosilicate compositions, is still ongoing. The main attention is paid to the composition, chemical and

† ***Cite as:*** S. Sayenko, V. Shkuropatenko, Y. Svitlychnyi, A. Zykova, S. Karsim, D. Kutnii, and V. Morgunov, East Eur. J. Phys. **1**, 94 (2023), https://doi.org/10.26565/2312-4334-2023-1-11

radiation resistance of glass matrices in order to ensure the safe conditioning of wastes of various compositions and demonstrate the safety of their disposal [11].

Thus, in [12], various glass and glass-ceramic materials are considered that are capable of immobilizing waste with a high load. The emphasis here is on the importance of the solubility of the waste components and the consequent undesirable crystallization compared to intentional crystallization of the glass-ceramic waste forms.

According to the authors of [13], glass is considered an acceptable form for curing low-level waste with a high boron content, generated at Korean nuclear power plants. The advantages of the process are ease of handling and unique ability to accept a wide variety of waste streams. The study involved development of glass structure and producing of several glass frits which were evaluated to determine their suitability for LRW vitrification. The fly ash generated in coal-fired power plants with the main components SiO_2 and Al_2O_3, is a material necessary for the formation of glass mesh. For selected compositions using fly ash, detailed evaluations of the final product were carried out, including the amount of waste, uniformity, chemical resistance, viscosity, etc. Up to 30 wt. % of the waste was included in the composition of glass welded at 1200 °C using fly ash after adding 5–10 wt. % Na_2O.

Works have been carried out and are being carried out to develop glass compositions for the immobilization of LRW from nuclear power plants with pressurized water reactors (PWR), characterized by a high concentration of sodium and boron [7, 14–17]. Borosilicate glass matrices with high insulating properties are considered as promising candidates.

The aim of the work is an experimental study of the vitrification of the simulant of vat residues of LRW from nuclear power plants with VVER-1000 and the effect of the glass composition on the strength properties and corrosion resistance of the obtained glass matrices.

MATERIALS AND METHODS

Experimental studies of the process of vitrification of liquid radioactive waste were carried out on simulators of vat residues (VR) of LRW from nuclear power plants with VVER reactors. The following salts and solutions were the initial materials for obtaining the VR simulator: H_3BO_3, NaOH, HNO_3, NaCl, KOH, NH_4OH, $FeSO_4{\cdot}7H_2O$, $CuSO_4{\cdot}5H_2O$, $CsNO_3$. A solution imitating the vat residue was obtained by dissolving weighed portions of the required amount of salts in distilled water to provide the appropriate concentration, according to the data on the average chemical composition of the vat residue of liquid radioactive waste from NPPs with VVER-1000 reactors. The vat residue has the following composition, g/l: Na^+ cations – 140.9; K^+ – 37.9; NH^{4+} – 1.0; Fe^{3+} – 4; Cu^{2+} – 0.74, anions BO_3^{3-} – 150.8; NO^{3-} – 156.2; SO_4^{2-} – 6; Cl^- – 2.8. Specific activity for the main isotopes: ^{137}Cs – $5.2{\cdot}10^{-5}$ Ci/l, ^{134}Cs – $2.8{\cdot}10^{-5}$ Ci/l, ^{60}Co – $6.1{\cdot}10^{-6}$ Ci/l [18]. The amount of cesium in the solution-simulator was increased by several orders of magnitude in relation to the calculated amount in accordance with the activity of its isotopes. In this case, it became possible to quantitatively determine cesium in a solution-simulator of VR by mass spectrometric methods.

The study of the composition of the resulting solution-simulator of VR was carried out using a high-resolution mass spectrometer with ionization in inductively coupled plasma ICP-MS ELEMENT 2.

Glass samples were melted in aluminum oxide crucibles in air in a Nabertherm P310 high-temperature electric furnace.

To grind the powders, a Pulverisette 6 planetary monomill was used.

Diffractometric studies were carried out on a DRON-4-07 X-ray diffractometer in copper Cu-Kα radiation using a Ni selective absorbing filter. The diffracted radiation was recorded by a scintillation detector. Phases were identified using the database of crystalline compounds ICDD PDF-2 (2004). To determine the vitrification temperature of the VR simulator, differential thermal (DTA) and thermographic (TG) analyzes were performed on an SDT Q600 V20.9 Build 20 thermal analyzer in the temperature range of 20–1200°C, heating rate 20°C/min.

Elemental analysis of samples of vitrified VR simulators was carried out on a high-resolution EMAL-2 laser mass spectrometer with double focusing according to Mattauch-Herzog. The random error of the analysis results is characterized by a relative standard deviation of 0.1–0.3.

The study of the microstructure of the obtained samples was carried out on a scanning (SEM) electron microscope JSM-7001F.

An IKS-29 IR spectrophotometer (LOMO) was used to record absorption spectra in the IR range.

The apparent density of the obtained samples was determined by hydrostatic weighing.

To prepare a solution-simulator of the vat residue, the required amounts of salts H_3BO_3, NaOH, NaCl, KOH, $FeSO_4{\cdot}7H_2O$, $CuSO_4{\cdot}5H_2O$ was dissolved in distilled water, then nitric acid HNO_3 and a solution of ammonia hydrate NH_4OH were added. The density of the model solution imitating the vat residue is 1300 g/l, pH = 11.

In order to determine the compliance with the composition of the VR simulator and real vat residue of NPPs with VVER-1000 reactors, the concentrations of the following elements in the obtained solution-simulator were measured: B, Na, K, S, Cl, Fe, Cu, Cs. The studies were carried out using a high-resolution mass spectrometer with ionization in inductively coupled plasma ICP-MS ELEMENT 2. The initial probe of the simulator solution was diluted 150,000 times. The results of the analysis, together with the targeted composition of the VR, are presented in Table 1. There is a fairly good agreement between the measured and the targeted composition of the VR. A slight discrepancy between the targeted and measured amounts of elements is probably due to the difficulty in taking a representative sample and the presence of insoluble precipitate in the simulant solution.

Before calcination, the obtained solution imitating the vat residue was dried at a temperature of 90 °C for 35 hours. The calcination was carried out in air at a temperature of 600 °C for 1 hour. After heat treatments, the mass of the obtained calcinate decreased by more than 3 times compared with the mass of the initial solution-simulator of VR. Then, the calcinate was ground in a planetary monomill at a speed of 300 rpm within 30 minutes. The resulting powder consisted of particles ≤ 10 μm in size.

Table 1. Targeted and measured composition of the vat residue solution

Element	Targeted concentration, g/l	Measured concentration, g/l
B	27.7	<16.8
Na	140.9	<114.6
K	37.9	<22.2
S	2.0	<1.7
Cl	2.8	<1.1
Fe	4.0	<4.2
Cu	0.7	<2.4
Cs	<0.1	<0.45

The process of vitrification of the VR simulator consisted of mixing powdered calcinate with glass-forming powder additives and subsequent melting of glass in aluminum oxide crucibles. Taking into account the fact that, in terms of radiation and corrosion resistance, borosilicate glass is one of the optimal matrices for localizing radioactive waste, various compositions of borosilicate matrices for vitrification of salt boron-containing wastes were studied. Since the content of Na and B in the vat residues of LRW from NPPs with VVER reactors is quite high, there is no need to add components containing these elements to obtain borosilicate glass. SiO_2 powder in the form of quartz sand was used as the main glass-forming additive. As is known, one of the main requirements for the vitrification of medium-level waste is the use of a minimum amount of additives in the melting of glass matrices [10]. Therefore, in the course of experiments on vitrification of the VR simulator, lead oxide, barium oxide, and calcium fluoride were added separately. It is known that the vat residues of NPPs with VVER-1000 reactors include Na_2SO_4 and NaCl components, which during the process of immobilization in borosilicate glasses may cause phase separation associated with the immiscibility of silicate and sulfate (chloride) systems [7, 19]. In order to prevent phase separation and the appearance of a sulfate-chloride phase during the vitrification of sulfate- and chloride-containing LRW, it is necessary to add PbO, BaO, and CaF_2 additives [20-22]. The following glass matrices SK45, SK45-Pb10, SK45-Ba10, and SK45-CF10 were obtained (Table 2).

Table 2. Chemical composition (initial) and melting temperature of glass matrices

Glass matrix	Compounds, wt. %					Melting temperature, °C
	SiO_2	PbO	BaO	CaF_2	VR	
SK45	45				55	1150
SK45-Pb10	45	10			45	1150
SK45-Ba10	45		10		45	1100
SK45-CF10	45			10	45	1150

The glass melting temperature and time were determined from the results of experiments to obtain the highest quality glass according to visual observations and with an acceptable viscosity for pouring the resulting glass from a crucible into metal molds (Fig. 1a). The optimal temperature-time conditions for vitrification of VR simulators were determined: 1100 – 1150°C, holding time 1 hour. The cube-shaped metal molds with the resulting glasses were annealed and cooled to room temperature in the switched off furnace. The samples of glass matrices SK45, SK45-Pb10, SK45-Ba10 and SK45-CF10 obtained after extraction from the metal mold are shown in Fig. 1b. As can be seen, samples-cubes with an edge length of 2 cm of all the above compositions of glass matrices are transparent and characterized by high-quality penetration.

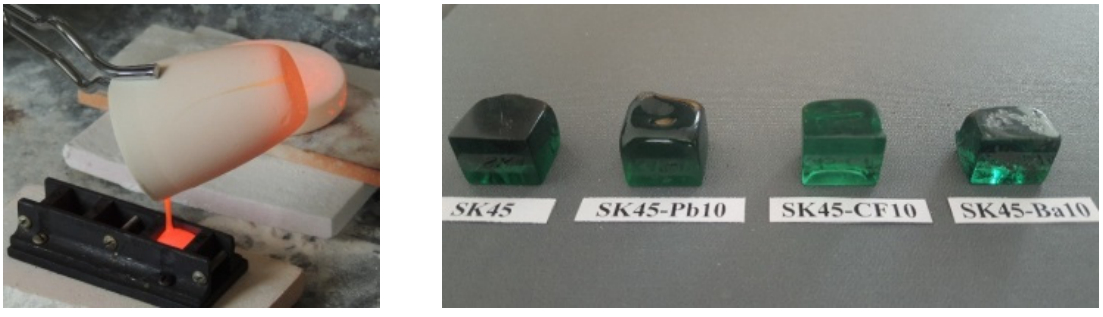

a b

Figure 1. Spill (a) and appearance of samples of glass matrices (b).

RESULTS AND DISCUSSION

Study of the phase composition of the mixture to obtain the SK45 glass matrix after heat treatment at a temperature of 600ºC for 1 hour showed the presence of the following phases: sodium nitrate $NaNO_3$ (JCPDS 36-1474), sodium tetraborate $Na_2B_4O_7$ (JCPDS 29-1179) and glass-forming silicon oxide SiO_2 (JCPDS 39-1425). Sodium nitrate and sodium tetraborate are the main components of the vat residues. In addition, in the region of angles $2\theta \approx 24–35$ °, there is a diffraction halo, which indicates the presence of an amorphous phase in the sample (Fig. 2a).

The presence of an amorphous phase in the material of the SK45 glass matrix indicates that at a temperature of 600ºC the process of glass formation is already underway. This fact is confirmed by the analysis of thermograms taken with the SDT Q600 V20.9 Build 20 thermal analyzer (Fig. 3). It can be seen that for the glass matrices SK45 and SK45-Pb10, an endothermic effect is observed, which starts at a temperature of about 430ºC [23]. This effect corresponds to the beginning of the glass transition process, which causes the presence of an amorphous phase at higher heat treatment temperatures.

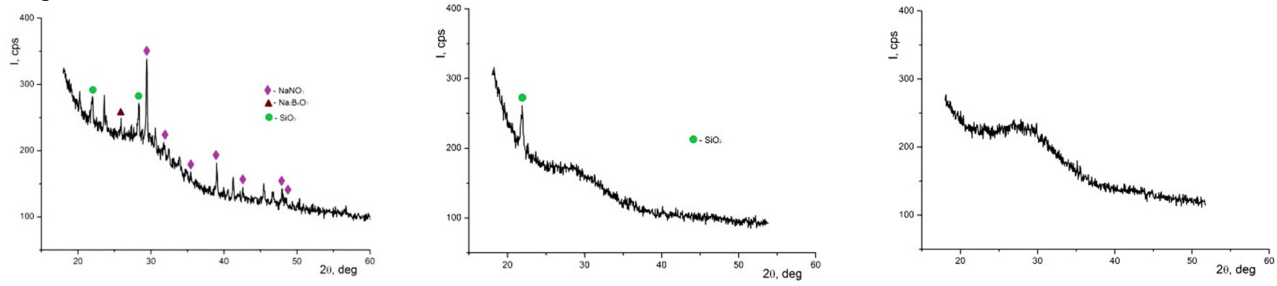

a b c

Figure 2. Diffractograms of SK45 glass matrix after heat treatment: 600ºC, 1 hour (a), 700 ºC, 1 hour (b), 1150ºC, 1 hour (c)

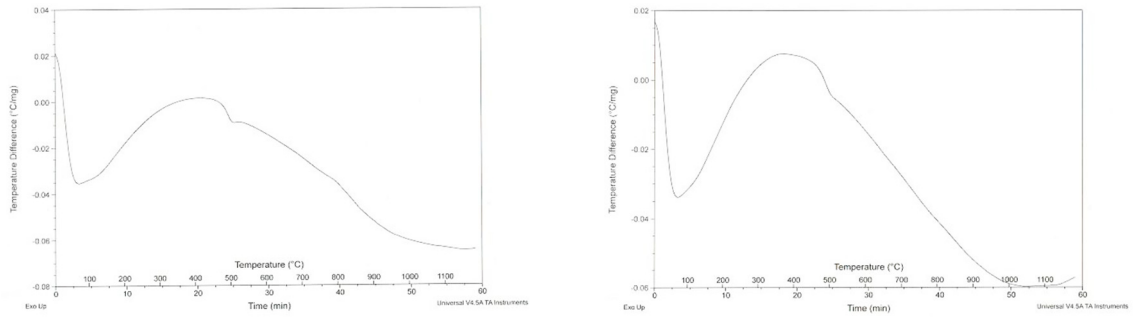

a b

Figure 3. Thermograms of samples of glass matrices SK45 (a) and SK45-Pb10 (b).

An increase in the melting temperature of the SK45 glass matrix material to 700 ºC leads to the disappearance of reflections of the components present in the distillation residues, namely sodium nitrate and sodium tetraborate. A decrease in the number of silicon oxide reflections to one is also observed (Fig. 2b). Further, after melting glass at a temperature of 1150ºC for 1 hour, according to X-ray phase analysis, only a diffraction halo in the region of angles $2\theta \approx 24 \div 35°$ is present in the diffraction pattern of the glass matrix SK45, i.e. the sample consists entirely of the amorphous phase (Fig. 2c). It should be noted that, according to XRD analysis, all obtained glass matrices SK45, SK45-Pb10, SK45-Ba10, and SK45-CF10 are X-ray amorphous.

Also, the absence of crystalline inclusions and segregation zones is confirmed by the results of scanning electron microscopy. The homogeneity of the glass matrix material and the absence of segregation zones are also confirmed by data on the uniformity of the distribution of glass matrix elements and cesium, obtained using X-ray cartography (Fig. 4).

Since glass is a brittle material, resistance to mechanical failure is an important criterion for evaluating the physical stability of a solidified waste form. In this regard, the mechanical properties of glassed LRW undoubtedly require quantitative evaluation, and their values must comply with the acceptance criteria for storage and disposal.

The strength test under uniaxial compression of samples of vitrified VR simulators was carried out on an electromechanical press of the “ZD 10/90” brand. During testing, the obtained samples-cubes of glass matrices with an edge length of 2 cm were installed with one of the selected faces on the lower support plate of the press in the center relative to its longitudinal axis. Next, loading was carried out and the forces of destruction of glass samples were determined. The determination of the compressive strength was calculated by dividing the breaking force by the working area of the glass sample. The results of tests to determine the compressive strength of the obtained samples is shown in Table 3. In addition, the values of the apparent density of the obtained glass matrices are presented.

The apparent density values increase significantly with the addition of lead oxide to the glass composition. Also, samples of the glass matrix SK45-Pb10 are characterized by the maximum value of the compressive strength. Sufficiently

high compressive strength values are also observed for glass matrix samples SK45, SK45-Ba10, and SK45-CF10. Thus, the authors of [8] provide data on the compressive strength of borosilicate glass for radioactive wastes in the range of 22-54 MPa. In addition, the obtained values of the ultimate compressive strength significantly exceed the norm for mechanical strength, which characterizes the quality of hardened high-level waste (9 MPa) [24].

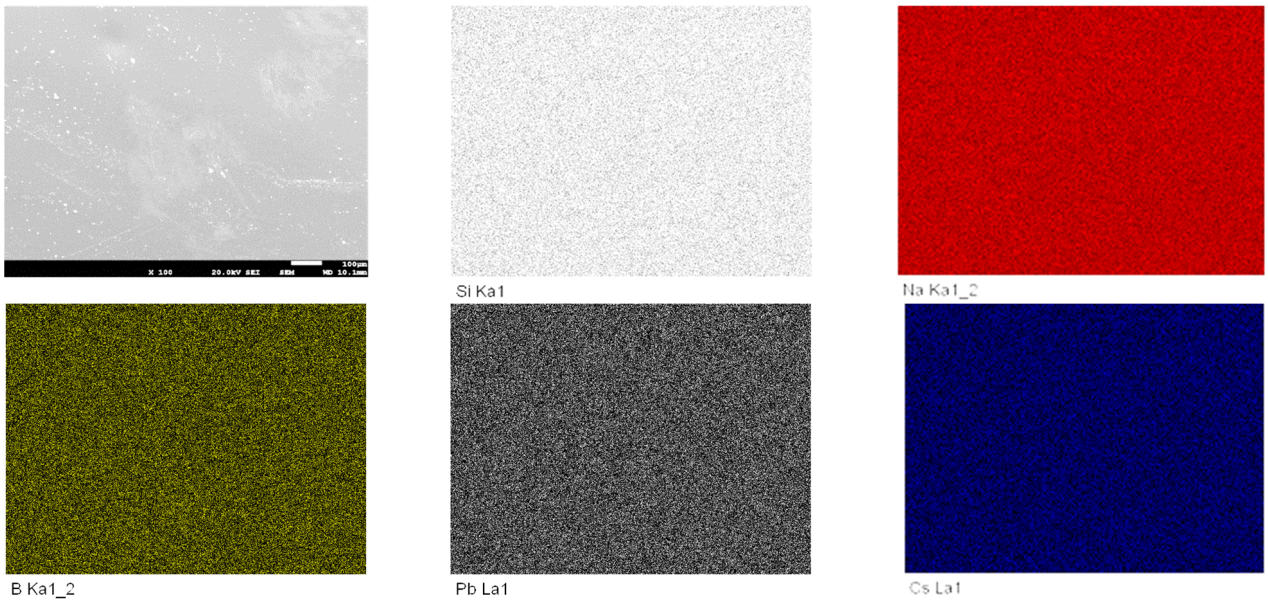

Figure 4. X-ray cartography of a cleavage of glass matrix sample SK45-Pb10:
a – structure, b – Si, c – Na, d – B, e – Pb, f – Cs elemental distribution

Table 3. Density and compressive strength of glass matrix samples

Glass matrix	Density, g/cm3	Compressive strength, MPa
SK45	2.62	78.5
SK45-Pb10	2.84	136.0
SK45-Ba10	2.59	59.5
SK45-CF10	2.27	72.6

To ensure reliable isolation of radionuclides included in the glass matrix for a long time, the vitrified waste form must have certain physical and mechanical characteristics. Since the main route of radionuclides entry from vitrified forms of waste into the environment is leaching by groundwater, it is necessary to determine their corrosion resistance [15].

The main parameter characterizing the corrosion resistance of the glass matrix is the leaching rate of radionuclides and matrix elements. The loss of total mass during leaching has the same function as the rate of leaching under the same test conditions. Mass loss is fairly easy and quick to measure. Therefore, this parameter was initially used to control the corrosion resistance of the glass matrix in order to determine the optimal glass composition for vitrification of the vat residue simulators.

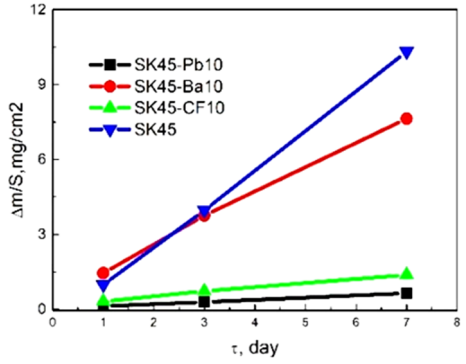

Figure 5. Dependence of mass loss of glass matrix samples on leaching time

The leaching test was carried out in Teflon containers at a constant temperature of 90 °C for 1, 3 and 7 days. The vitrified samples of the VR simulator had the shape of a cube with an edge of 2 cm. The mass of the samples was measured before and after leaching. The loss of the total mass related to the total surface of the samples Δm/S (g/cm^2) was calculated by the formula:

$$\Delta m \,/\, S = \frac{(m_0 - m_t)}{s} \qquad (1)$$

where m_0 (g) is the initial mass of the sample, m_t (g) is the mass of the sample after t days of leaching, S (cm^2) is the total surface of the sample.

The results of leaching of glass matrix samples SK45, SK45-Pb10, SK45-Ba10 and SK45-CF10 are shown in Fig. 5.

As can be seen, the best indicators of corrosion resistance are observed on samples SK45-Pb10. The mass loss of the SK45-Pb10 sample on the 7th day of leaching is $6.4 \cdot 10^{-4}$ g/cm^2. As is known, the presence of a small amount of lead oxide significantly reduces the mobility of sodium ions in a glass frame. Sufficiently high corrosion resistance is demonstrated by samples of the glass matrix SK45-CF10. However, the weight loss of the SK45-CF10 glass matrix

samples on the 7th day of leaching is $1.37 \cdot 10^{-3}$ g/cm^2, which is more than twice the weight loss of the SK45-Pb10 sample. According to the authors of [20], the addition of fluorine ion has a destructive effect on the silicon-oxygen framework of the glass matrix. As a result, spatial cavities are formed in the glass matrix to accommodate sulfate ions.

In turn, a noticeable destruction of the silicon–oxygen framework can lead to the degradation in the corrosion resistance of the glass. Also, finely dispersed crystalline phases of fluorine-containing compounds are formed with a certain concentration of fluorine in glass. The fluorine-containing crystalline particles act as nuclei for heterogeneous glass crystallization.

A more noticeable destruction of the silicon-oxygen framework of the SK45-CF10 glass matrix compared to SK45-Pb10 is observed in the IR spectra of samples of these glass matrices (Fig. 6). The IR spectrum of the SK45-Pb10 glass matrix sample has a broad band in the region of 470 cm^{-1} and a broad doublet band with weak maxima at 980 and 1020 cm^{-1}. These bands refer, respectively, to the bending and stretching vibrations of O-Si-O in the silicon-oxygen glass network. The spectrum exhibits a weak peak at 700 cm^{-1} associated with symmetric stretching vibrations of the Si-O-Si bridges, as well as a peak at 1590 cm^{-1} (deformation vibrations of OH in water molecules) and a doublet at 3400 and 3450 cm^{-1} due to the presence of two types of H_2O: structurally bound and absorbed [25–28]. The spectrum of the glass matrix sample SK45-CF10 also contains a number of broad bands with a sharp maximum at 470 cm^{-1} and a diffuse maximum in the region of 980 cm^{-1}, which are due to bending and stretching vibrations of the Si-O bonds. However, there is no second maximum of the 1020 cm^{-1} doublet. In addition, there are differences in the spectral band associated with stretching and bending vibrations of structurally bound and absorbed water molecules and hydroxyl groups.

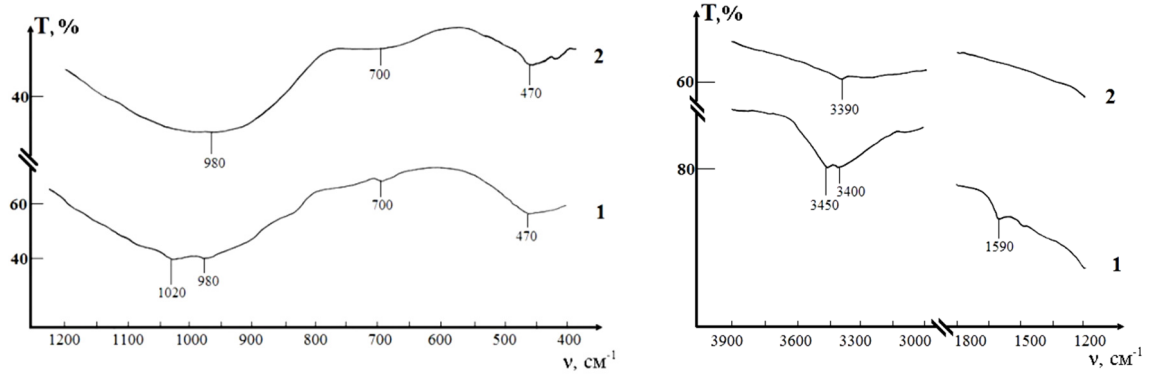

a b

Figure 6. IR absorption spectra of glass matrices
(curve 1 – SK45-Pb10, curve 2 – SK45-CF10) in the range: a – 400-1200 cm^{-1}, b – 1200-4000 cm^{-1}

After the adding of barium oxide into the composition of borosilicate glass, an increase in mass loss during leaching test is observed. The greatest weight loss during leaching is detected on samples of the SK45 glass matrix. The reduced corrosion resistance of the SK45 sample compared to other tested glasses is explained by the fact that the SK45 glass matrix is welded from 45 wt.% silicon oxide and 55 wt.% VR simulators. While all other glass matrices are welded with a load of 45 wt.% of the VR simulators. This fact means that SK45 glass matrix contains the largest amount of easily soluble sodium and potassium compared to other glass matrices, and explains the degradation of the corrosion properties of the SK45 glass matrix.

Conducted tests for corrosion resistance with an increase in leaching time up to 28 days showed a decrease in the weight loss of samples of glass matrices with time. The mass loss of the S45-Pb10 sample on the 28 day of leaching is $1.06 \cdot 10^{-3}$ g/cm^2, and that of the S45-CF10 sample is $2.83 \cdot 10^{-3}$ g/cm^2. The weight loss of the S45-Pb10 sample is more than two times less than the weight loss of the SL-1 glass matrix sample ($2.44 \cdot 10^{-3}$ g/cm^2) at the same waste load (45 wt.%), which was proposed as the matrices for immobilization of borate waste from PWR reactors [4].

The leaching rate of SK45-Pb10 and SK45-CF10 glass matrix elements during leaching tests was determined using the following equation:

$$v = \frac{m_n^i}{f_i \cdot SA \cdot t_n} \tag{2}$$

where:
ν is the leaching rate (g/cm^2·day),
m^i_n is the mass of the i-th element (g) leached over a given time interval,
f_i is the mass fraction of the i-th element in the initial sample (g/g),
SA is the open geometric surface of the sample (cm^2),
t_n is the duration of the n_{th} leaching period (day).

The mass of each element in the leach for the nth leaching period was determined using a high-resolution mass spectrometer with ionization in inductive plasma ICP-MS ELEMENT 2 and f_i - EMAL-2 laser mass spectrometer.

The values of the leaching rates of the elements Si, B, Na, K, Pb, Ca, and Cs from the glass matrices SK45-Pb10 and SK45-CF10 are shown in fig. 7. For the glass matrix SK45-Pb10, during the first day, the highest leaching rate is observed for cesium, potassium, and sodium, and the lowest for lead. With an increase in leaching time, the rate of potassium and cesium leaching decreases significantly, but the rate of sodium leaching remains relatively high. Thus, the leaching rate of Cs after 14 days is $1.5 \cdot 10^{-5}$, K – $5.22 \cdot 10^{-6}$, Na – $2.53 \cdot 10^{-5}$, Pb – $1.72 \cdot 10^{-6}$ g/cm^2·day. The glass matrix SK45-CF10 is characterized by the highest leaching rates for sodium ($5.8 \cdot 10^{-5}$) and boron ($5.1 \cdot 10^{-5}$ g/cm^2·day). The smaller values of leaching rate are observed in the case of cesium ($3.8 \cdot 10^{-5}$) and potassium ($2.4 \cdot 10^{-5}$ g/cm^2·day). The lowest leaching rates are detected for calcium ($2.5 \cdot 10^{-6}$ g/cm^2·day). It should be noted that the cesium leaching rate from the SK45-CF10 glass matrix is more than 2 times higher compared to the SK45-Pb10 glass matrix.

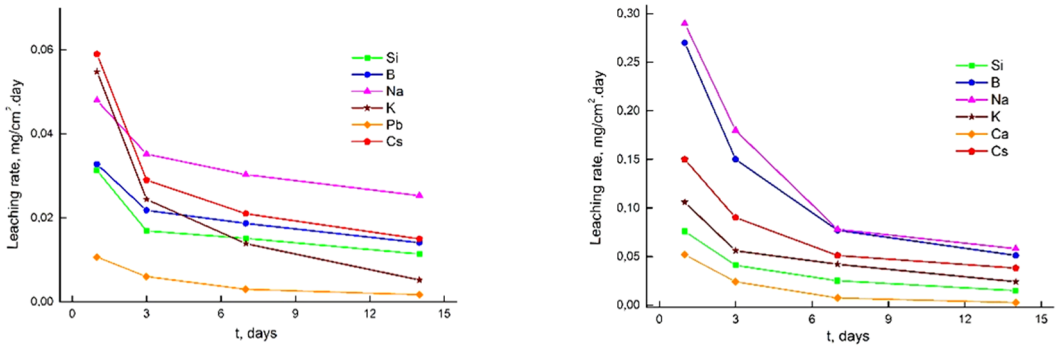

Figure 7. Leaching rates of glass matrix elements: (a) SK45-Pb10, (b) SK45-CF10

The obtained rates of cesium leaching at a temperature of 90 °C from a vitrified simulator of VR are consistent in order of magnitude with the data given in the literature on the leaching rate of ^{137}Cs from vitrified wastes of low and medium activity at the same (45 wt.%) or lower waste load [28]. In general, these values indicate a sufficiently high corrosion resistance of glasses, which are quite acceptable for the immobilization of LRW vat residues.

Previously, the absorbed dose which is accumulated by borosilicate glass matrices with included vat residues during 300 years of storage was calculated, and studies of the effect of simulated X-ray irradiation on their physical and mechanical properties were also carried out. It was shown that a lead-borosilicate glass matrix has a high radiation resistance [29]. The obvious advantage of the obtained glass matrices is the relatively low melting point along with the high content of included waste. Thus, the glass matrix S45-Pb10, containing 45% imitators of LRW vat residues, in combination with high strength, corrosion and radiation characteristics, is promising candidate for curing of the boron-containing salt LRW.

CONCLUSION

1. Experimental studies of the process of immobilization of the imitator of vat residues residues of LRW from nuclear power plants with VVER-1000 reactors in borosilicate glass were carried out. To obtain borosilicate glass matrices, quartz sand, oxides of lead, barium, and calcium fluoride were used.

2. Tests for mechanical strength under uniaxial compression of cubic samples of borosilicate glass matrices of various compositions were carried out. It has been established that the maximum compressive strength of lead-borosilicate matrix specimens is 136.0 MPa. Samples of this glass matrix have maximum density values – 2.84 g/cm^3.

3. According to the results of SEM and XRD studies of lead-borosilicate matrices, the prepared samples are X-ray amorphous, characterized by a dense and uniform structure, and have no crystalline inclusions.

4. Studies of the corrosion resistance of the obtained samples of glass matrices by leaching in water were carried out. It has been established that lead-borosilicate matrices are the most leaching-resistant glass matrices for immobilization of the vat residue simulators. The cesium leaching rate is $1.5 \cdot 10^{-5}$ g/cm^2·day.

5. It is shown that the obtained lead-borosilicate glass matrices are the most optimal candidates for immobilization of the vat residues of LRW from NPP. These glass matrices are characterized by high mechanical strength, corrosion and radiation resistance and include the maximum amount of LRW simulator – up to 45 wt.%.

Competing interests. The authors declare that they have no competing interests.

ORCID IDs

Sergii Sayenko, https://orcid.org/0000-0002-2598-3598; **Volodymyr Shkuropatenko**, https://orcid.org/0000-0003-2618-0858
Yevhenii Svitlychnyi, https://orcid.org/0000-0002-6522-4940; **Anna Zykova**, https://orcid.org/0000-0001-6390-8161
Svitlana Karsim, https://orcid.org/0000-0003-0656-1717; **Dmytro Kutnii**, https://orcid.org/0000-0001-9591-4013
Volodymyr Morgunov, https://orcid.org/0000-0002-8681-1941

REFERENCES

[1] S.Y. Sayenko, V. Shkuropatenko, A. Pylypenko, A. Zykova, S. Karsim, V. Andrieieva, and S. Moshta, PAST, **2**, 103–113 (2020), https://vant.kipt.kharkov.ua/ARTICLE/VANT_2020_2/article_2020_2_103.pdf

[2] Y.O. Olkhovyk, and P.O. Korchagin, Ядерна енергетика та довкілля [Nuclear energy and environment], **1**, 20-23 (2014), http://npe.org.ua/wp-content/uploads/2019/02/3_2014.pdf. (in Ukrainian)
[3] B.G. Ershov, T.K. Yurik, G.L. Bykov, A.V. Gordeev, P.V. Kozlov, O.M. Slyunchev, and Yu.V. Glagolenko, Вопросы радиационной безопасности [Radiation Safety Issues], **1**, 3 (2008), http://bibliom.ru/wp-content/uploads/2015/06/33.pdf. (in Russian)
[4] L. Shanggen, J. Sheng, and B. Tang, **298**, 180-183 (2001). https://doi.org/10.1016/S0022-3115(01)00592-X
[5] N.P. Laverov, B.I. Omel'yanenko, S.V. Yudintsev, S. V. Yudintsev, and S.V. Stefanovsky, Geol. Ore Deposits, **54**, 1–16 (2012). https://doi.org/10.1134/S1075701512010059
[6] N.P. Laverov, B.I. Omel'yanenko, S.V. Yudintsev, S.V. Stefanovsky, and B.S. Nikonov, Geol. Ore Deposits, **55**, 71–95 (2013). https://doi.org/10.1134/S1075701513020037
[7] I. Sobolev, M. Ojovan, T. Scherbatova, O. Batuhnova, *Стекло для радиоактивных отходов* [*Glasses for radioactive waste*]. (Energoatomizdat, Moscow, 1999). (in Russian)
[8] M. Ojovan, and P. Poluektov, Безопасность Окружающей Среды [Environmental Safety], **1**, 112-115 (2010). https://www.atomic-energy.ru/technology/33037
[9] D.J. Backhouse, A.J. Fisher, J.J. Neeway, C.L. Corkhill, N.C. Hyatt, and R.J. Hand, npj Mater. Degrad. **2**, 1-10 (2018). https://doi.org/10.1038/s41529-018-0050-5
[10] P.A. Bingham, N.C. Hyatt, and R.J. Hand, Glass Technology: European Journal of Glass Science and Technology, Part A, **53**(3), 83-100 (2012). https://doi.org/10.1038/s41529-018-0050-5
[11] S. Gin, P. Jollivet, M. Tribet, S. Peuget, and S. Schuller, Radiochim. Acta, **105**(11), 927-959 (2017). https://doi.org/10.1515/ract-2016-2658
[12] J.S. McCloy, and S. Schuller, Comptes Rendus. Géoscience, **354**, 121-160 (2022). https://doi.org/10.5802/crgeos.111
[13] J. Shenga, K. Choi, and M. JaeSong, Journal of Nuclear Materials, **297**(1), 7-13 (2001). https://doi.org/10.1016/S0022-3115(01)00598-0
[14] K. Sawada, Y. Enokida, and T. Tsukada, Journal of Nuclear Science and Technology, **57**(6), 671-677 (2020). https://doi.org/10.1080/00223131.2019.1710615
[15] N. Krylova, and P. Poluektov, Атомная энергия [Atomic Energy], **78**(2), 93-98 (1995). https://j-atomicenergy.ru/index.php/ae/article/view/4852 (in Russian)
[16] S. Stefanovskii, Физика и химия стекла [Physics and chemistry of glass], **16** (5), 818-826 (1990). (in Russian)
[17] U. Olihovik, Ядерна і радіаційна безпека [Nuclear and radiation safety], **4**(64), 46-50 (2014). http://dspace.nbuv.gov.ua/handle/123456789/97638. (in Ukrainian)
[18] B. Kudriavcev, U. Korchagin, and A. Reznik, Patent RU2226726C2 (2004). (in Russian)
[19] A. Nikiforov, V. Kulichenko, and M. Jiharev, *Обезвреживание жидких радиоактивных отходов* [*Neutralization of liquid radioactive waste*], (Energoatomizdat, Moscow, 1985). (in Russian)
[20] O. Karlina, N. Iliina, A. Ovchinnikov, and M. Ojovan, Patent RU2065215C1 (1996).
[21] P.A. Bingham, A.J. Connelly, R.J. Hand, N.C. Hyatt, and P.A. Northrup, Glass Technol.: Eur. J. Glass Sci. Technol. A, **50**(3), 135–138 (2009). https://shura.shu.ac.uk/id/eprint/5705
[22] S. Stefanovskii, A. Minaev, and F. Lifanov, Радиохимия [Radiochemistry], **32**(3), 162-166 (1990). (in Russian)
[23] Dj. Geodokyan, and S. Stepanyan, Физика и химия стекла [Physics and chemistry of glass], **5**, 622-635 (1982). (in Russian)
[24] Отходы высокоактивные отвержденные. Общие технические требования [Highly active solidified waste. General technical requirements], GOST R 50926-96. (Gosstandart Rossii, Moscow, 1996).
[25] M. Skvorcov, N. Mihailenko, and S. Stefanovskii, Успехи в химии и химической технологии [Advances in chemistry and chemical technology], **XXXI**(3), 108-110 (2017), https://cyberleninka.ru/article/n/borosilikatnye. (in Russian)
[26] I. Levickii, L. Papko, and M. Dyadenko, Химия и технология неорганических материалов и веществ [Chemistry and technology of inorganic materials and substances], **3**, 3-8 (2015). https://cyberleninka.ru/article/n/steklotsementy-dlya-vakuumplotnyh-spaev. (in Russian)
[27] S. Stefanovskii, I. Ivanov, A. Gulin, and F. Lifanov, Радиохимия [Radiochemistry], **3**, 106-109 (1993). (in Russian)
[28] I. Sobolev, S. Dmitriev, F. Lifanov, A. Kobelev, S. Stefanovsky, and M. Ojovan, Glass Technology, **46**(1), 28–35 (2005). https://www.ingentaconnect.com/content/sgt/gt/2005/00000046/00000001/art00003
[29] V. Morgunov, S. Sayenko, V. Shkuropatenko, Y. Svitlychnyi, O. Bereznyak, S. Lytovchenko, and V. Chyshkala, "Calculation of the Absorbed Dose by a Borosilicate Glass Matrix and its simulated irradiation", East Eur. J. Phys. **3**, 121 (2022). https://doi.org/10.26565/2312-4334-2022-3-16

ОСКЛУВАННЯ ІМІТАТОРА КУБОВИХ ЗАЛИШКІВ РІДКИХ РАДІОАКТИВНИХ ВІДХОДІВ

С.Ю. Саєнко[a], В.А. Шкуропатенко[a], Є.О. Світличний[a], Г.В. Зикова[a], С.О. Карсім[a], Д.В. Кутній[a], В.В. Моргунов[b]

[a]Національний науковий центр "Харківський фізико-технічний інститут вул. Академічна, 1, Харків, 61108, Україна
[b]Харківський національний університет імена В. Н. Каразіна, м. Свободи, 4, Харків, 61022, Україна

В роботі проведено дослідження та обгрунтування використання оптимальних складів скла для осклування імітатору кубових залишків РРВ АЕС з реакторами ВВЕР-1000 в залежності від таких параметрів, як температура осклування, міцність, корозійна стійкість, відсутність кристалічних фаз, мінімізація скло-утворюючих добавок та включення максимальної кількості відходів. Встановлено, що температура варіння свинцево-боросилікатних скло-матриць становить 1150 °С, що задовольняє вимогам щодо осклування низько- та середньо-активних відходів. Межа міцності на стиск отриманих зразків скло-матриць становить 136.0 МПа. Також показано, що свинцево-боросилікатні скло-матриці є найбільш стійкими до вилуговування. Швидкість вилуговування цезію становить $1{,}5 \cdot 10^{-5}$ г/см^2·добу.

Ключові слова: *рідкі радіоактивні відходи; кубовий залишок; осклування; міцність; швидкість вилуговування*

East European Journal of Physics. 1. 102-108 (2023)
DOI:10.26565/2312-4334-2023-1-12 ISSN 2312-4334

INVESTIGATION OF THE IMPACT OF GLASS WASTE IN REACTIVE POWDER CONCRETE ON ATTENUATION PROPERTIES FOR BREMSSTRAHLUNG RAY†

Wasan Z. Majeed[a,*], Rawaa K. Aboud[b], Nesreen B. Naji[a], Shatha D. Mohammed[b]
[a]*Department of Physics, College of Science, University of Baghdad, Baghdad, Iraq*
[b]*Department of Civil, College of Engineering, University of Baghdad, Baghdad, Iraq*
**Corresponding Author: wasan_zmz@yahoo.com*
Received November 29, 2022; revised December 15, 2022; accepted December 20, 2022

Reactive Powder Concrete (RPC) is one of the most advanced recent high compressive strength concretes. This work explored the effects of using glass waste as a fractional replacement for fine aggregate in reactive powder concrete at levels of 0%, 25%, 50%, and 100%. Linear and mass attenuation coefficients have been calculated as a function of the sample's thickness and bremsstrahlung energy. These coefficients were obtained using energy selective scintillation response to bremsstrahlung having an energy ranging from (0.1-1.1) MeV. In addition, the half-value thickness of the samples prepared has been investigated. It was found that there is a reversal association between the attenuation coefficient and the energy of the bremsstrahlung ray. The results showed that, with the exception of the specimen with a partial replacement of 25% glass waste, adding fine aggregate in part by glass waste had a negative impact on the reactive powder concrete's attenuation properties. That means the sample's density can be improved with the glass waste content ratio to 25%. Also, the bremsstrahlung radiation shielding capabilities of reactive powder concrete can be enhanced using glass waste of not more than 25%.
Keywords: *Attenuation properties; Bremsstrahlung ray; Reactive Powder Concrete (RPC); Glass waste; Sustainable material*
PACS: 28.41Qb, 28.41.Te

1. INTRODUCTION

Bremsstrahlung ray one of the nuclear radiations which classify as a great harmful ray, it has an extensive series of applications. Shielding parameters for this ray is important in the field of radiation protection to prevent its effects. It is essential to know the bremsstrahlung ray spectrum distribution that yield from $^{90}Sr/^{90}Y$ beta source in lead. Beta sources are increasingly used in the medical applications. One of the troubles in the request of beta radiation shields regards to the bremsstrahlung ray and it requires shielding against beta particles reserves [1].

To reduce the effects of radiation on the human body, many safety materials were produced. In nuclear reactors, concrete and lead are frequently employed. Additionally, reactive powder concrete (RPC) is regarded as the most significant recent development in high compressive strength concrete. These concrete varieties were created using technologies to support microstructures. It is more durable and also has better mechanical properties than regular concrete [2, 3]. Wen L., et al [4] investigation focused on the mechanical and micro structural characteristics of RPC samples. In order to create RPC samples, coal gangue sand was substituted for natural river sand at various weight ratios ranging from 0 to 100% at intervals of 25%.

In order to selection appropriate type of material to sufficiently prevent various forms of radiations, the attenuation properties must be intentional [5]. The exact values of attenuation coefficients for bremsstrahlung ray in numerous materials are necessary for nuclear and radiation physics. The energy of radiation and the nature of the object determine the attenuation coefficient [6]. In nuclear and environmental physics, there are a lot of researches have been reported to study the relatives between energy, attenuation properties and material thickness as in refs. [7-13].

Through the use of cementations materials, some of these researches have been designed to improve the mechanical properties of concrete [14–16].

The concrete industry is aware of these materials' ability to enhance certain of the characteristics of regular concrete [17]. By testing linear and mass attenuation coefficients using several radiation sources with varying energies, Wasan et al. [18] investigate the potential of employing reactive powder concrete as a shielding material. Reactive powder concrete was shown to be capable of absorbing beta particles and gamma rays without significantly reducing the specimen's compressive strength.

The linear attenuation coefficient μ (cm^{-1}) is an important shielding parameter which describe the ability of the material to attenuate the incident radiation. In the present work, the μ was measured experimentally using bremsstrahlung ray transmission method according to lambert law:

$$I = I_0 \exp(-\mu x). \quad (1)$$

where x is the absorber thickness, I_0 and I were the incident and transmitted intensities respectively. Then, the mass attenuation coefficient μ_m (cm^2/g) was calculated through the linear attenuation coefficient using equation (2):

† ***Cite as:*** W.Z. Majeed, R.K. Aboud, N.B. Naji, and S.D. Mohammed, East Eur. J. Phys. **1**, 102 (2023), https://doi.org/10.26565/2312-4334-2023-1-12

$$\mu_m = \frac{\mu}{\rho}. \quad (2)$$

ρ is particle density of absorber in gm/cm^3. The half value layer ($X_{1/2}$) is given by:

$$X_{1/2} = \frac{0.693}{\mu}. \quad (3)$$

In this work, cube samples of RPC with glass waste as fractional replacement of fine aggregate by 0%, 25%, 50% and 100% have been prepared to estimate the performance of samples composite in attenuating bremsstrahlung ray.

2. MATERIALS AND METHODS

The chemical compositions and physical characteristics of common Portland cement according to Iraqi specification No. 5/1984 are shown in Tables 1 and 2 [19]. Table 3 shows the grain size distribution of the fine aggregate, which was represented by river sand, and ranged from (150 to 600) μm. As shown in Table 4, all characteristics of the river sand complied with Iraqi specification No. 45/1984 [20]. In this investigation, there was a waste of window glass. The employed river sand had been crushed and ground in a laboratory using Los Angeles abrasion equipment before being sorted through sieves calibrated to acquire the same gradation as stated in Table 5.

Physical and chemical properties of silica fume are displayed in Tables 6, 7, and it complies with ASTM C1240-03 requirements [21]. Bulk density in Table 6 was obtained from the manufacture data sheet (MEYCO®MS610).

In order to conduct the research's experimental program, four collections of standard cubes (50×50×50) mm were cast utilizing the RPC's implemented mix, as shown in Table 8.

Table 1. Chemical composition and major compounds of cement

Oxides	Content %	Iraqi Specification Limits (I.Q.S 5/1984) % [19]
CaO	61.91	-
Fe_2O_3	3.28	-
Al_2O_3	5.04	-
SiO_2	21.38	-
MgO	2.09	Max, 5
SO_3	2.19	Max, 2.8
L.O. I	2.64	Max. 4
L.S. F	0.887	0.66-1.02
In. Residue	0.72	Max. 1.5
	Major compounds (Bogue's equations)	
C_3S	57.60	-
C_2S	29.844	-
C_3A	7.813	-
C_4AF	9.981	-

Table 2. Physical properties of cement

Property	Result	Iraqi Specifications Limits No. 5/1984 [19]
Fineness, Blaine Method (m^2/kg)	323	Min, 230
Setting time (hr: min)		
-Initial setting	2:15	Min. 45 min.
- Final setting	4:20	Max. 10 hrs.
Compressive strength (MPa)		
3 days	22.6	Not less than 15MPa
7 days	30.1	Not less than 23MPa

Table 3. Grading of the fine aggregate (river sand)

Sieve opening(mm)	Passing %	Iraqi Specification Limits (I.Q.S. 45/1993) % [20] (Zone 4)
10	100	100
4.75	100	95-100
2.36	100	95-100
1.18	100	90-100
0.6	85.1	80-100
0.3	22.4	15-50
0.15	9	0-15

Table 4. Properties of the fine aggregate.

Item	Result	Iraqi Specification Limits (I.Q.S. 45/1993) [20]
SO_3 content %	0.17	Max. 0.5
Bulk density(kg/m^3)	1687	-
Specific gravity	2.54	-
Water absorption %	0.8	-

Table 5. Grading of the waste glass.

Sieve opening(mm)	Passing %	Iraqi Specification Limits (I.Q.S. 45/1993) % [20] (Zone 4)
10	100	100
4.75	100	95-100
2.36	100	95-100
1.18	100	90-100
0.6	85.5	80-100
0.3	32.3	15-50
0.15	13.5	0-15

Table 6. Physical properties of silica fume.

Property	Test result	ASTM C 1240 Specification [21]
Specific surface area, m^2/kg	21060	Min. 15000
Retaining on sieve 45μ, %	4.8 %	Max. 10%
Pozzolanic Activity %	113	Min. 105
Bulk Density* kg/m^3	550-700	-

Table 7. Chemical analysis of silica fume.

Oxides	Content %	ASTM C1240 Specification % [21]
SiO_2	90.59	Min. 85%
Fe_2O_3	1.56	-
Al_2O_3	0.75	-
CaO	0.73	-
MgO	1.21	-
SO_3	0.59	-
L.O. I	2.60	Max. 6%
Moisture content	1.13	Max. 3%

Table 8. Mixing proportion of RPC.

Mix Sample	Cement(kg/m^3)	Silica Fume 87 (kg/m^3)	Fine Aggregate (kg/m^3)	Glass Waste (kg/m^3)	Water (kg/m^3)
NG (0%)	800	200	1000	0	200
NG1 (25%)	800	200	750	250	200
NG2 (50%)	800	200	500	500	200
NG3 (100%)	800	200	0	1000	200

Bremsstrahlung ray was formed in suitably thickness of lead using $^{90}Sr/^{90}Y$ pure beta source with end-point energies of 0.546 and 2.274 MeV. The bremsstrahlung ray absorption characteristics of reactive powder concrete at various thicknesses have been investigated and tested. For the measurements, which were authorized, two collimators with a combined diameter of 5 mm and energies ranging from 0.1 to 1.1 MeV were used. The distance between source and detector was about 35 cm.

The bremsstrahlung ray intensities have been carried out with NaI(Tl) scintillation detector of dimension 2″×2″. Equations (1), where is the absorption coefficient, can be used to evaluate the intensities, which were determined for a set duration of 1000 sec.

3. RESULTS AND DISCUSSIONS

To investigate the shielding parameters in reactive powder concrete, it is essential to know bremsstrahlung ray distribution or spectra. The absorption spectra for bremsstrahlung ray without and with glass waste replacement (0%, 25%, 50% and 100%), respectively has been shown in Fig. 1. It is apparent that the intensity of bremsstrahlung ray decreases as the energy increased.

Fig.2. shows the variation of intensity I of bremsstrahlung ray with glass waste replacement 0%, 25%, 50%, and 100% compared with the original intensity as a function of energy. It is obvious that the intensity decreasing for reactive powder concrete containing 25% glass waste is more than other specimens of glass waste partial replacement.

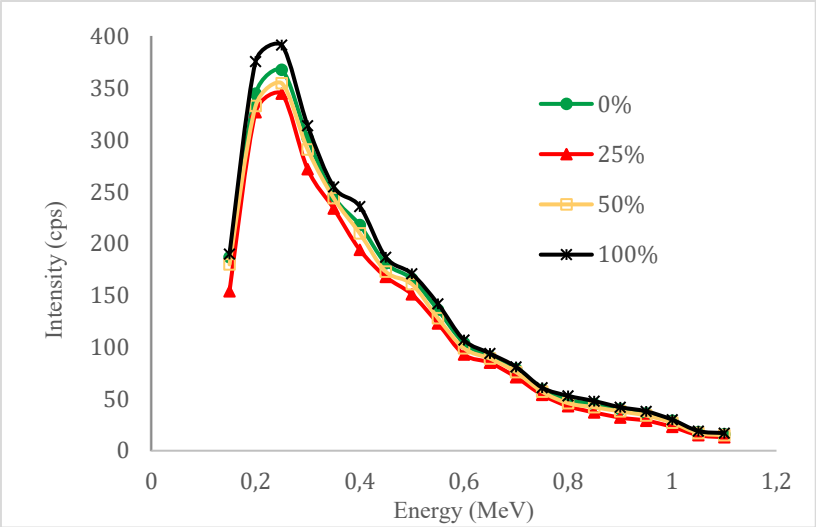

Figure 1. Absorption spectra with different glass waste replacement for bremsstrahlung ray as a function of energy

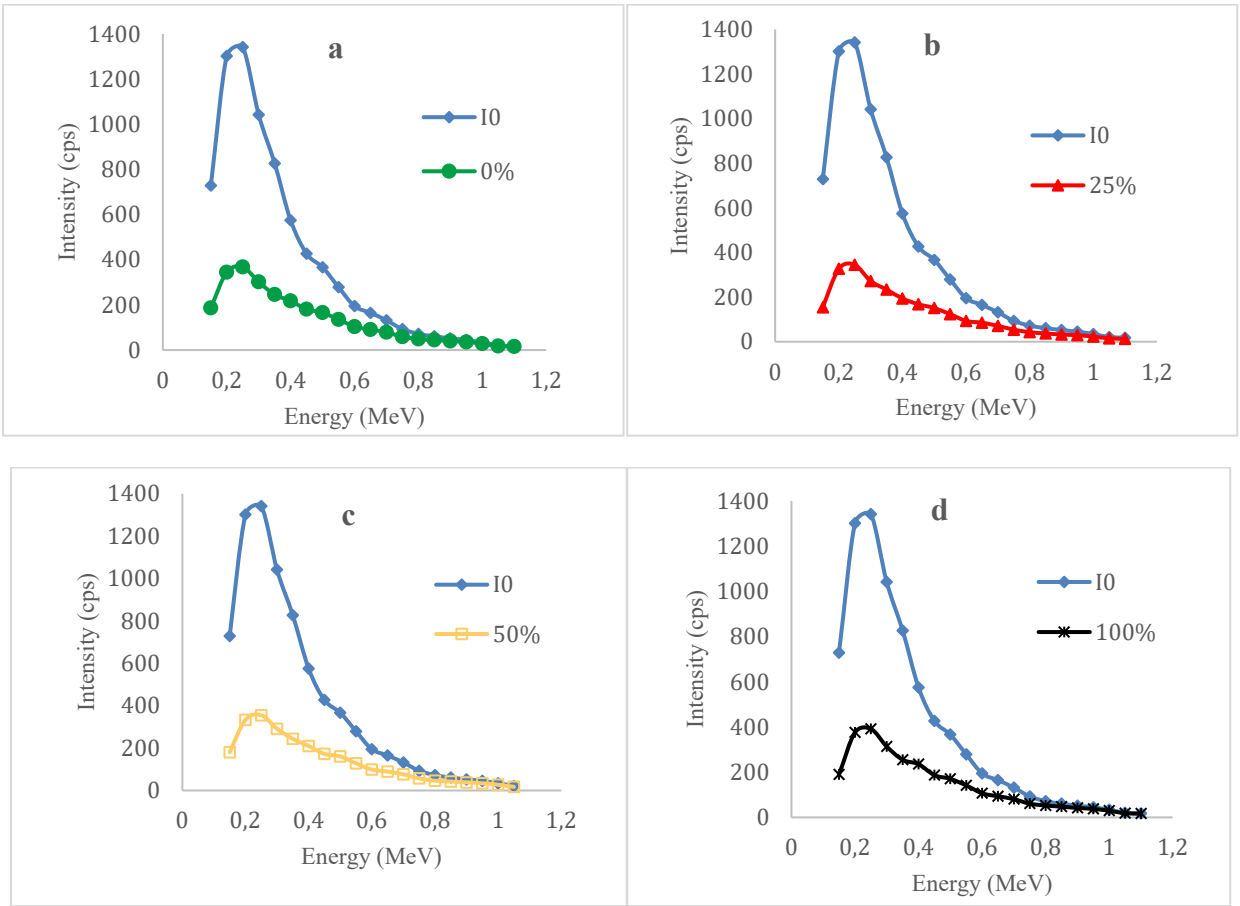

Figure 2. Original and absorption spectrum for bremsstrahlung ray with glass waste:

a) original I_0, 0% replacement. b) original I_0, 25% replacement.
c)original I_0, 50% replacement. d) original I_0, 100% replacement.

The effect of the bremsstrahlung ray energies on μ for all the tested specimens are presented in Fig 3. It is found that the inversely proportion with bremsstrahlung energies for the same thickness of reactive powder concrete.

The fitted curve of measured logarithmic transmissions intensity for reactive powder concrete containing 0%,25%, 50%, 100%, glass waste versus absorber thickness were plotted as in Fig. 4 to obtain linear attenuation coefficient.

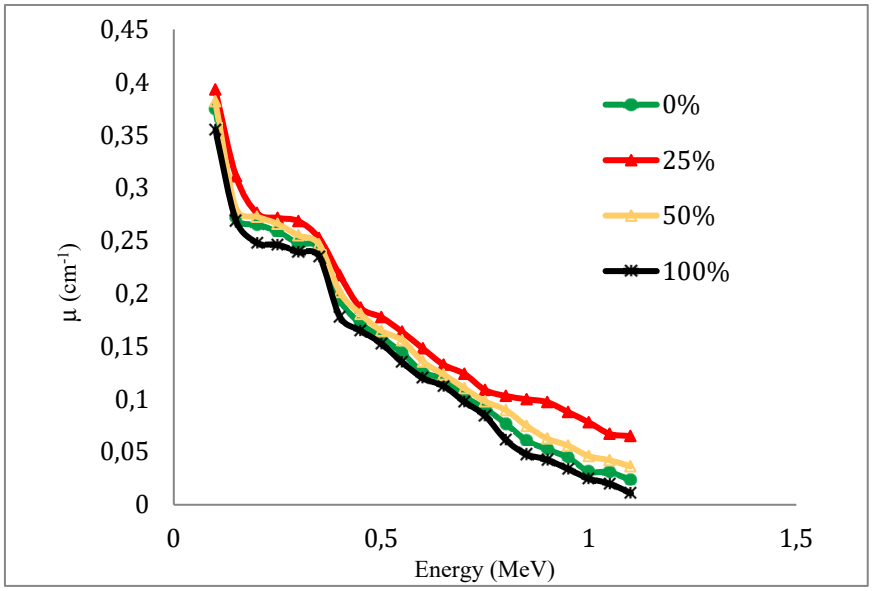

Figure 3. Attenuation coefficient as a function of energy.

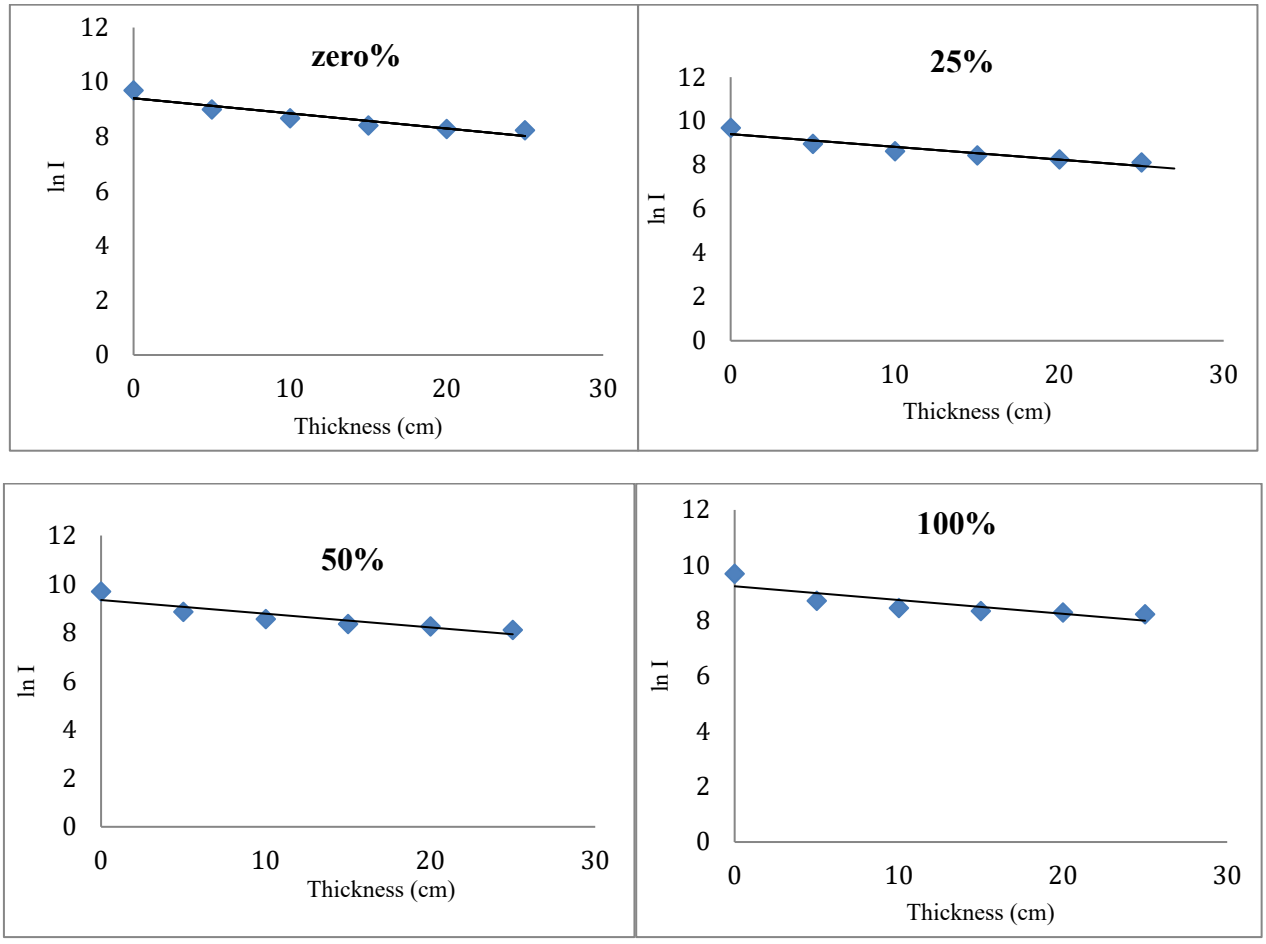

Figure 4. logarithmic transmissions intensity (ln I) for reactive powder concrete containing 0%,25%, 50%, 100%, glass waste versus absorber thickness in cm.

The experimental results of linear and mass attenuation coefficients for reactive powder concrete as a function of glass waste replacement had presented in Fig. 5a and 5b, respectively. It is obvious from this figure that the experimental values of linear and mass attenuation coefficients for reactive powder concrete containing 25% glass waste were higher than those which obtained from the specimen of (0%) glass waste replacement but the lowest values were found at 100% replacement of glass waste. It can be detected from this Figure that the attenuation coefficients decrease as the replacement of glass waste increases over 25%.

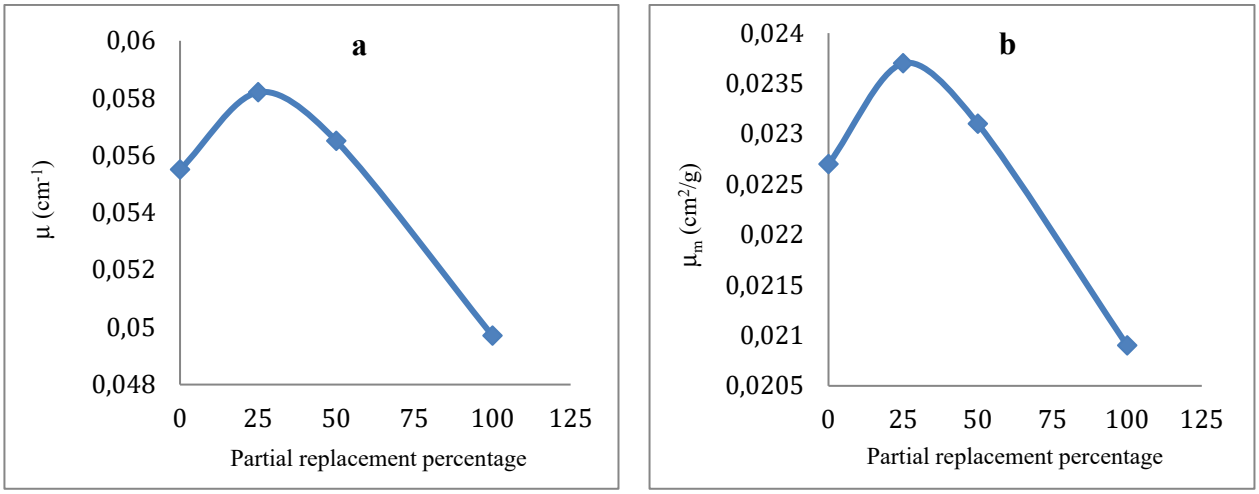

Figure 5. Attenuation coefficient of reactive powder concrete as a function of partial replacement percentage
a. Linear attenuation coefficient, **b**. Mass attenuation coefficient

According to Fig. 6, the behavior of the μ curve is the exact opposite of that of the $X_{1/2}$ curve. This shows that the qualities of the RPC attenuations improved and offered superior shielding when the RPC contained 25% of glass waste.

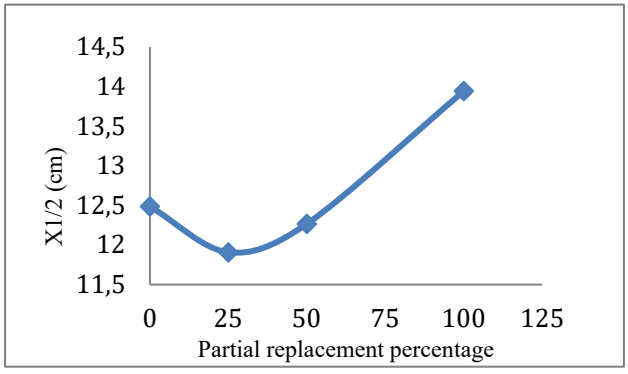

Figure 6. Half-value thickness as a function of glass waste replacement

4. CONCLUSION

In this study, linear attenuation properties such as linear attenuation coefficient, mass attenuation coefficient and half value thickness of reactive powder concrete without and with glass waste were calculated. Also, the effects of using glass waste as a fractional replacement for fine aggregate in reactive powder concrete at levels of 0%, 25%, 50%, and 100% was investigated.

From the obtained results, it can be concluded that the glass waste replacement gave a significant improvement in attenuation property. Also, tested samples in this work are a good absorbers of bremsstrahlung radiation. In addition, the density of the sample can be enhanced with the glass waste content ratio to 25 %. The bremsstrahlung radiation shielding capabilities of reactive powder concrete can be enhanced using glass waste not more than 25 %. By increasing the glass waste ratio in the reactive powder concrete up to 25 %; the density (ρ), the value of linear attenuation coefficients as well as mass attenuation coefficients are decreased and the half values thickness increases.

Acknowledgments

This work was performed in the University of Baghdad, College of Science, Department of Physics and College of Engineering, Department of Civil Engineering. We would like to thank the Council of the departments for useful propositions.

ORCID IDs

Wasan Z. Majeed, https://orcid.org/0000-0001-6595-1841; **Rawaa K. Aboud**, https://orcid.org/0000-0002-1172-1124
Nesreen B. Naji, https://orcid.org/0000-0003-1673-8678; **Shatha D. Mohammed**, https://orcid.org/0000-0002-4751-8064

REFERENCES

[1] J.E. Martin, *Physics for Radiation Protection*. 3rd ed. (WILEY-VCH Verlag GmbH & Co. KGaA, Weinheim, 2006), pp. 311.
[2] B. Badarloo, P. Lehner, and R.B. Doost, "Mechanical Properties and Gamma Radiation Transmission Rate of Heavyweight Concrete Containing Barite Aggregates", Materials, **15**, 2173 (2022). https://doi.org/10.3390/ma15062173
[3] S.H. Al-Tersawy, R.A. El-Sadany, H.E. Sallam, "Experimental gamma-ray attenuation and theoretical optimization of barite concrete mixtures with nanomaterials against neutrons and gamma rays", Constr. Build. Mater. **289**, 123190 (2021). https://doi.org/10.1016/j.conbuildmat.2021.123190

[4] W. Luo, H. Wang, X. Li, X. Wang, Z. Wu, Y. Zhang, X. Lian, and X. Li, "Mechanical Properties of Reactive Powder Concrete with Coal Gangue as Sand, Replacement", Materials, **15**, 1807 (2022). https://doi.org/10.3390/ma15051807
[5] N.M. Aowd, and H.S. Hussain, "Absorption coefficient measurement of bremsstrahlung radiation in nano composite", Eng. & Tech. Journal, **33**(7), 1258 (2015). https://etj.uotechnology.edu.iq/article_116691.html
[6] C. Laxman, and R. Dayanand, "Mass attenuation coefficient measurements in soil sample", Res. J. Chem. Sci. **2**(5), 17 (2012). http://www.isca.in/rjcs/Archives/v2/i5/3.ISCA-RJCS-2012-035_Done.pdf
[7] S.D. Mohammed, W.Z. Majeed, N.B. Naji, and N.M. Fawzi, "Investigating the influence of gamma ray energies and steel fiber on attenuation properties of reactive powder concrete", Nucl. Sci. Tech. **28**(10), 153 (2017). https://doi.org/10.1007/s41365-017-0305-9
[8] B.M. Chandrika, H.C. Manjunatha, K.N. Sridhar, and H. Chikka, "Bremsstrahlung shielding parameters in polymer concretes", Radiat. Eff. Def. Solids. **173**(5-6), 414 (2018). https://doi.org/10.1080/10420150.2018.1462363
[9] R. Ramli, F.M. Idris, M.F. Yapandi, J.Md. Saad, and S.A. Biyamin, "Investigation on different compositions of flyash concrete on gamma and neutron radiation", Mater. Sci. Eng. **555**, 012013 (2019). https://doi.org/10.1088/1757-899X/555/1/012013
[10] I.K. Alhagaish, and V.K. Sakharov, "Photon radiation fields characteristics in concrete for photon sources with energies from 10 to 50MeV", Inter. J. Sci. Tech. Res. **9**(4), 2280 (2020). https://www.ijstr.org/final-print/apr2020/Photon-Radiation-Fields-Characteristics-In-Concrete-For-Photon-Sources-With-Energies-From-10-To-50-Mev.pdf
[11] N.B. Naji, Sh.D. Mohammed, W.Z. Majeed, N.M. Fawzi, "Irradiation duration effect of gamma ray on the compressive strength of reactive powderconcrete", in: *International Conference on Geotechnical engineering*, (Trans Tech Publications Ltd, Switzerland, 2020), pp. 15-21.
[12] A.M. Abdel-Latif, M.I. Sayyed, H.O. Tekin, and M.M. Kassab, "Optimizing the shielding properties of strength-enhanced concrete containing marble", Pape. Phys. **12**, 120005 (2020). https://doi.org/10.4279/pip.120005
[13] M.D. Desta, M. Tessema, V.K. Mittal, and D.D. Amamo, "Experimental determination of linear attenuation coefficient of gamma ray in Zinc foil at different energies", J. Medi. Phys. Appl. Sci. **5**(1-6), 1-8 (2020). https://doi.org/10.36648/2574-285X.5.1.6
[14] D. Rezaei-Ochbelagh, S. Azimkhani, and H.G. Mosavinejad, "Shielding and strength tests of silica fume concrete", Ann. Nucl. Energy, **45**, 150–154 (2012). http://dx.doi.org/10.1016/j.anucene.2012.02.006
[15] K. Janković, S. Stanković, D. Bojović, M. Stojanović, and L. Antić, "The influence of nano-silica and barite aggregate on properties of ultra-high-performance concrete", Constr. Build. Mater. **126**, 147 (2016). http://dx.doi.org/10.1016%2Fj.conbuildmat.2016.09.026
[16] M.M. Tufekci, and A. Gokce, "Development of heavyweight high-performance fiber reinforced cementitious composites (HPFRCC)", Part 1: mechanical properties, Constr. Build. Mater. **148**, 559 (2017). https://doi.org/10.1016/j.conbuildmat.2017.05.009
[17] Z. Wu, C. Shi, and W. He, "Comparative study on flexural properties of ultra-high-performance concrete with supplementary cementitious materials under different curing regimes", Constr. Build. Mater. **136**, 307 (2017). https://doi.org/10.1016/j.conbuildmat.2017.01.052
[18] W.Z. Majeed, N.B. Naji, S.D. Mohammed, "Attenuation coefficient of reactive powder concrete using different energies", Int. J. Adv. Res. **4**(7), 72 (2016). http://dx.doi.org/10.21474/IJAR01/1161
[19] Iraq Standard Specification. IQS 5:84. Standard specification for Portland cement. Iraq: C.O.S.Q.C; 1984.
[20] Iraq Standard Specification. IQS 45-93. Aggregate from natural sources for concrete and building construction. Iraq: C.O.S.Q.C; 1993.
[21] American Society for Testing and Materials. ASTM C1240-03. Standard specification for use of silica fume as a mineral admixture in hydraulic cement concrete, mortar and grout. USA: ASTM; 2003.

ДОСЛІДЖЕННЯ ВПЛИВУ СКЛЯНИХ ВІДХОДІВ У РЕАКТИВНОМУ ПОРОШКОВОМУ БЕТОНІ НА ВЛАСТИВОСТІ ОСЛАБЛЕННЯ ГАЛЬМІВНОГО ВИПРОМІНЮВАННЯ

Васан З. Маджід[a], Раваа К. Абуд[b], Несрін Б. Наджі[a], Шата Д. Мохаммед[b]
[a]*Фізичний факультет, Науковий коледж, Багдадський університет, Багдад, Ірак*
[b]*Цивільний факультет Інженерного коледжу Багдадського університету, Багдад, Ірак*

Реактивний порошковий бетон (RPC) є одним із найдосконаліших сучасних бетонів високої міцності на стиск. У цій роботі досліджено вплив використання скляних відходів як фракційної заміни дрібного заповнювача в реактивному порошковому бетоні на рівнях 0%, 25%, 50% і 100%. Лінійні та масові коефіцієнти ослаблення були розраховані як функція товщини зразка та енергії гальмівного випромінювання. Ці коефіцієнти були отримані з використанням енергоселективної сцинтиляційної реакції на гальмівне випромінювання з енергією в діапазоні від (0,1 до 1,1) МеВ. Крім того, досліджено половинну товщину виготовлених зразків. Встановлено, що між коефіцієнтом ослаблення та енергією гальмівного випромінювання існує зворотний зв'язок. Результати показали, що, за винятком зразка з частковою заміною 25% відходів скла, додавання дрібного заповнювача частково відходами скла мало негативний вплив на властивості ослаблення реактивного порошкового бетону. Це означає, що щільність зразка може бути покращена за допомогою співвідношення вмісту скляних відходів до 25%. Крім того, здібності реактивного порошкового бетону до захисту від гальмівного випромінювання можна підвищити, використовуючи відходи скла не більше ніж на 25%.

Ключові слова: *властивості ослаблення; гальмівне випромінювання; реактивний порошковий бетон (RPC); скляні відходи; стійкий матеріал*

EAST EUROPEAN JOURNAL OF PHYSICS. 1. 109-117 (2023)
DOI:10.26565/2312-4334-2023-1-13 ISSN 2312-4334

THE ELECTRONIC AND THERMODYNAMIC PROPERTIES OF TERNARY RARE EARTH METAL ALLOYS†

Aman Kumar[a,*], Anuj Kumar[b], Kamal Kumar[c], Rishi Pal Singh[d], Ritu Singh[e], Rajesh Kumar[f]

[a]*Department of Physics, Keral Verma Subharti College of Science, Swami Vivekanand Subharti University Meerut, Uttar Pradesh, India*
[b]*Department of Physics, Mahamaya Government Degree College, Sherkot, Bijnore, Uttar Pradesh, India*
[c]*Department of Physics, D.A.V College Kanpur, Uttar Pradesh, India*
[d]*Department of Physics, S. S. V. College, Hapur 245101, Uttar Pradesh, India*
[e]*Department of Chemistry, S. S. V. College, Hapur 245101, Uttar Pradesh, India*
[f]*Department of Physics, Government Degree College, Nanauta, Saharanpur, UP, Pin-247452, India*
**Corresponding Author e-mail: 01amankumar@gmail.com*
Received January 3, 2023; revised January 29, 2023; accepted January 30, 2023

This article uses the FP-LAPW approach within the DFT method, and the quasi-harmonic Debye model to investigate the electronic and thermodynamic properties of intermetallic rare earth materials (such as SmInZn, SmInCd, and SmTlZn). Thermodynamic properties were determined by the quasi-harmonic Debye model, whereas the FP-LAPW approaches within DFT method were utilized to derive electronic properties. The calculated structural parameters and the available experimental data have been examined, and it was observed that there was a good agreement between available experimental and calculated values of structural parameters. The electronic behavior of SmInZn, SmInCd and SmTlZn compounds shows the metallic character. We have examined a few thermodynamic characteristics. All calculated characteristics were found to match experimental or theoretical calculations.
Keywords: *electronic; intermetallic; density of state; DFT*
PACS: 71.20.Lp; 71.20.Eh 71.20._b

INTRODUCTION

A lot of investigation has been done on the equal-atomic ternary rare-earth intermetallic compounds, owing to their various interesting properties in the field of material science. In recent years, intermetallic compounds have received a lot of attention from scientists due to their distinctive properties. They exhibit numerous structural properties [1-2]. There is a focus on structural, electronic, magnetic, and thermodynamic properties, such as fermionic, heavy-fermions [3-4], and half-metallic behavior in rare-earth intermetallic compounds such as SmInZn, SmInCd and SmTlZn [5–6], and the giant magneto-resistance device is an industrial application of heavy rare earth compounds [7-9]. These equal-atomic type compounds of rare earth have been investigated seriously in the last few years [10-15]. Sm-based compounds have been studied with theoretical and experimental significance [16-20]. It is seen from this study that Sm-based compounds can be used for refrigeration. This is based on the magneto-caloric effect (MCE) [21]. The SmInZn, SmInCd and SmTlZn compounds show many interesting applications in spintronics devices, magnetic sensors, unconventional superconductors, met-magnetism, magnetic random-access memories, and spin glass [21-22]. In this calculation, we used the space group P63/mmc (number-194) for the SmInZn, SmInCd and SmTlZn rare-earth compounds, and their crystal structures are similar to those of $CaIn_2$ at low temperatures [21].

Table 1. SmInZn, SmInCd and SmTlZn crystallographic data (space group and Wyckoff position).

Compound	Space group	Atoms	X	Y	z
SmInZn, SmInCd SmTlZn	P63/mmc (194)	Sm	0	0	0
		In/Tl	1/3	2/3	1/4
		Zn/Cd	1/3	2/3	3/4

The calculations have been executed with the help of the first principle method based on DFT, which is exerted in WIEN2K software package [23]. We have investigated the electronic and thermodynamic characteristics of SmInZn, SmInCd, and SmTlZn compounds using the FP-LAPW technique and GGA approximation [24, 25]. Here, structural and electronic properties are described, such as the energy Vs volume curve (which shows the stability of material), band diagrams, and, total and partial density of states. Thermodynamic behaviors of the SmInZn, SmInCd and SmTlZn compounds have been investigated with the help of GIBBS2 software. It's based on the Quasi Harmonic Debye (QHD) model [26]. In thermodynamics behavior, we have investigated some parameter like bulk modulus of materials (B_0), specific heat (Cv), Grüneisen parameter (γ), Debye temperature (θ_D), thermal expansion coefficient (α) and entropy (S).

COMPUTATIONAL METHOD

This article has been presented for first-principal calculations using full-potential approach based on DFT, it is utilized by the software WIEN2K [27-28], to investigate the electronic and thermodynamic properties of SmInZn,

† ***Cite as:*** A. Kumar, A. Kumar, K. Kumar, R.P. Singh, R. Singh, and R. Kumar, East Eur. J. Phys. **1**, 109 (2023), https://doi.org/10.26565/2312-4334-2023-1-13

SmInCd, and SmTlZn. In this modern DFT approach method; exchange-correlation energy potential has played an important role in the SCF process based on GGA [29]. In the SCF process, we take the value of cut-off parameter Kmax = $7/R_{MT}$ [where Kmax is the magnitude of largest reciprocal lattice vector and R_{MT} is the minimum radii of atoms in BZ (Brillouin zone)] and R_{MT} values have been taken 2.50 a.u. for Gd and Sb atoms and 2.46 a.u. for Ni atom. In SCF process, 47 k-mess points and 2000 k-point was used in the irreducible parts of full BZ and cut-off energy −6.0 Ry. We have chosen the energy convergence 0.0001ec. The energy terms used in this process gives information about valence and core atomic states. The total energy Vs volume curve has been fitted in the Brich-Murnaghan equation of state (EOS) [30]. Thermodynamics behaviors of the SmInZn, SmInCd and SmTlZn compound have been investigated, with the help of GIBBS2 software. It's based on the Quasi Harmonic Debye (QHD) model.

RESULTS

Structural and electronic properties

The stability curves (volume vs energy curve) can be used to calculate the structural characteristics of an intermetallic compound. The bulk modulus of material (B_0), pressure derivative bulk modulus of material (B_0'), and lattice constant (a_0) parameters were derived from structural characteristics. Figures 1(a), 1(b), and 1(c) depict the energy vs. volume curve (i.e., material stability curve) for SmInZn, SmInCd, and SmTlZn respectively, as fitted by the Brich-Murnaghan equation of state (EOS).

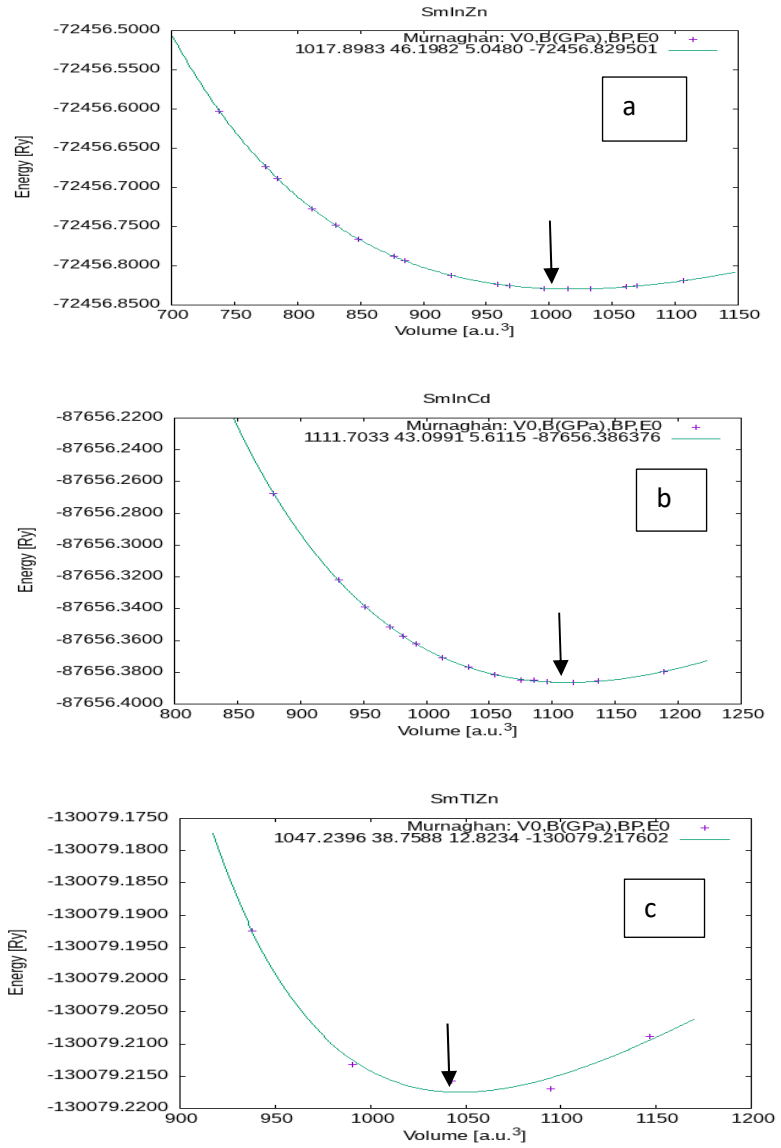

Fig. 1 Total energy Vs unit cell volume for (a) SmInZn (b) SmInCd and (c) SmTlZn

Using the optimization method and revealing that compound SmInZn is stable with a minimum energy value (E_0 = -72456.829501 Ry) at the minimum volume (V_0 = 1017.8983 a. u^3). The optimization method revealed that compound SmInCd is stable with a minimum energy value (E_0 = -87656.386376 Ry) at the minimum volume (V_0 = 1111.7033 a. u^3) while SmTlZn is stable with a minimum energy value (E_0 = -130079.217602 Ry) at the minimum

volume (V_0 = 1047.2396 a. u^3). After calculating the energy Vs. volume curve (i.e., material stability curve), we get the values of lattice constant (a_0), bulk modulus of material (Bo) and pressure derivative of bulk modulus of material (B_0'). (See Table 2). These structural parameters are obtained using the GGA approximation. The value of the lattice constant we determined from our calculations is supported by some research on these compounds [32].

Table 2. Some structural parameters calculated using the GGA approximation

Parameter	Symbols	SmInZn	SmInCd	SmTlZn
Lattice parameters (Å)	a_0	4.0952	4.8660	4.7780
	c_0	6.5879	7.4690	7.8130
Bulk modulus of material (GPa)	B_0	46.1982	43.0991	38.7588
Pressure derivative of bulk modulus of material (GPa)	B_0'	5.0480	5.6115	12.8234
Energy at equilibrium Condition (Ryd.)	E_{min}	-72456.829501	-87656.386376	-130079.217602
Volume of Unit cell at equilibrium condition (a. u. ^3)	V_0	1017.8983	1111.7033	1047.2396

At present, we are discussing here spin polarized electronic characteristics such as energy bands and DOS (i.e., density of states). The calculated energy bands for majority and minority spin channels along the high symmetry directions Γ, Σ, M, K, Λ and Δ in the first Brillouin zone for SmInZn, SmInCd, and SmTlZn compounds were obtained using GGA approaches, which are shown in Figures 2 (a) to 2 (f) respectively. Figures 2(a) and 2(b) show band structures for spin up and spin down for SmInZn Compound. Similarly, Figs. 2(c) and 2(d) have been represented for SmInCd, and Figs. 2(e) and 2(f) have been depicted for SmTlZn compound.

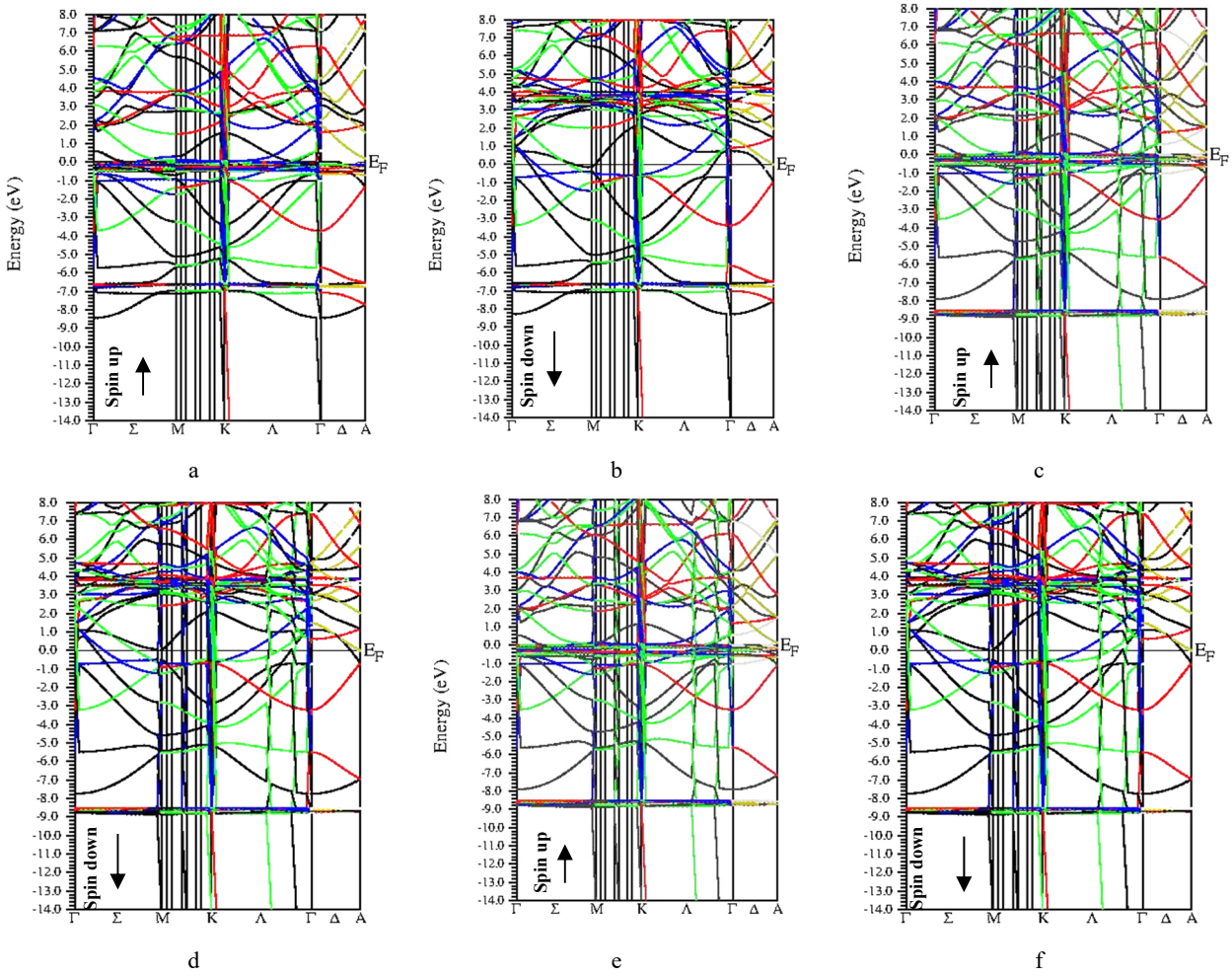

Figure 2. Band diagram for (a) spin up for SmInZn (b) spin down for SmInZn (c) spin up for SmInCd (d) spin down for SmInCd (e) spin up for SmTlZn (f) spin down for SmTlZn

It is clear from these graphs that most of the energy levels in the valence bands lie between -8.0 eV and 0.0 eV and conduction bands lies above 0.0 eV, Whereas the Fermi level is assumed to at the origin. It can be seen from Figure 2(a,b,c,d,e,f) Due to the electronic arrangement of Tl and In [Xe] $4f^{14}5d^{10}6s^26p$ and [Kr] $4d^{10}5S^25p^1$, the bands that were present in at roughly-09.0 eV in SmTlZn, SmInZn and SmInCd for spin up have been disappear in spin down bands, as can be seen in Figs. 2(a)–(f) (i.e. these bands in exist due to Zn bands).

Additionally, the valence band and conduction bands both cross the Fermi level, so there is no band gap. Thus, three compounds (SmInZn, SmInCd, and SmTlZn) indicative metallic properties. The Sm-f orbitals are mainly to blame for the formation of these bands. Now we are going to talk about the total densities of states, also known as T-DOS, for providing metallic character to these compounds. In addition, the profile of the partial densities of states (P-DOS) for the SmInZn, SmInCd, and SmTlZn compounds have been calculated with the help of the GGA approach and are plotted in graphs in Figure 3 (a-i) for SmInZn, Figure 4 (a-i) for SmInCd, and Figure 5 (a-i) for SmTlZn.

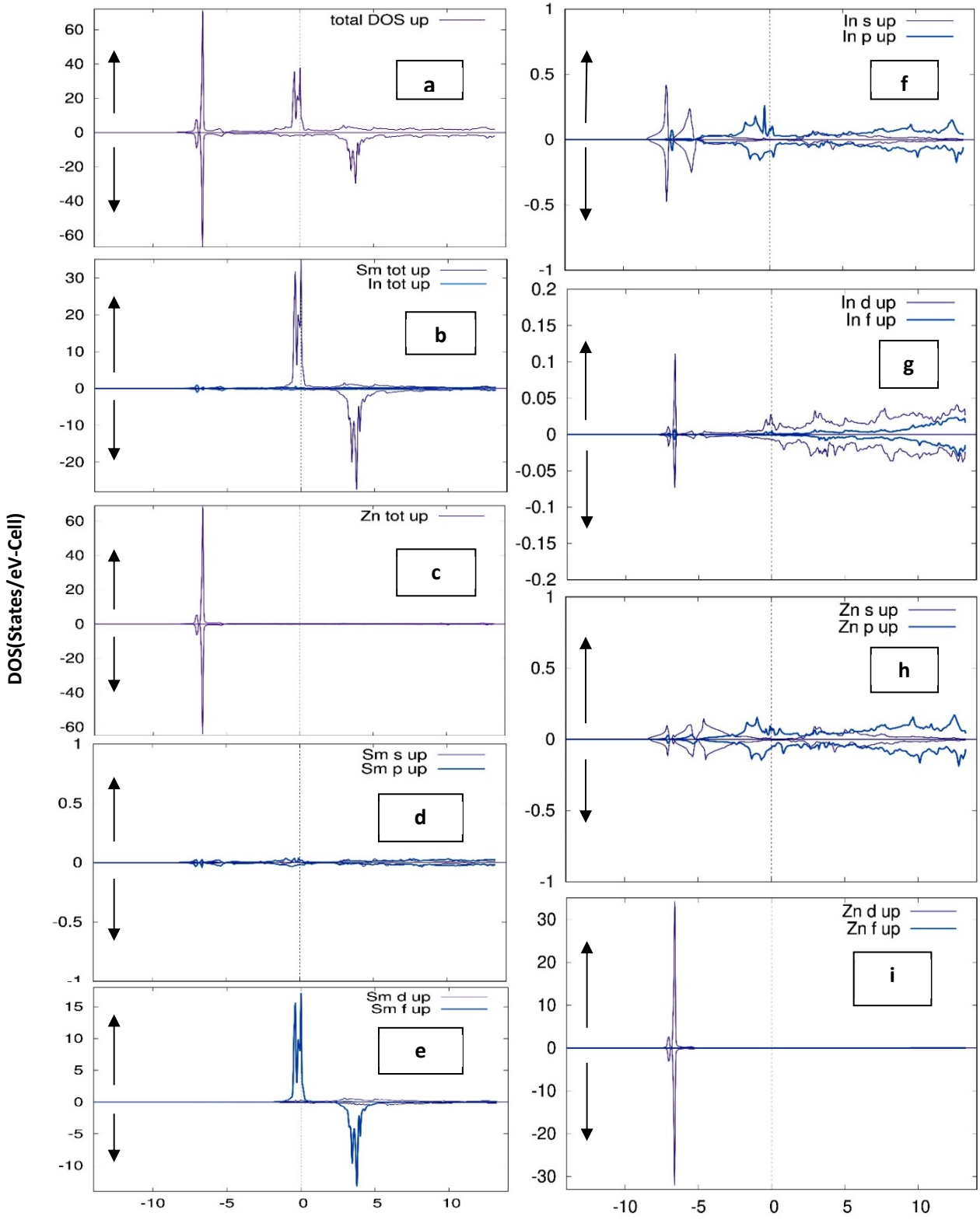

Figure 3. T-DOS and P-DOS for (a) SmInZn -Total (b) Sm-Total & In-Total (c) Zn-Total (d) Sm-s & Sm-p (e) Sm-d & Sm-f (f) In-s & In-p (g) In-d & In-f (h) Zn-s & Zn-p (i) Zn-d & Zn-f

The Fermi level at the origin can be seen in Fig. 3(a-i). It has been found that three sharp peaks are at around 0, -1 and -7 electron-volts (eV) in the spin-up state below the Fermi level and also one peaks are obtained at around +4 electron-volts(eV) above the Fermi level. It has been found that one sharp peak is at Fermi level in a spin-down state. According to our observations, the Zn-d states are responsible for the peak that occurs at around -7 eV below the Fermi level for both channels. A small contribution of In-s and In-d states. A second peak at about 0 eV and -1 eV is caused by the spin-up state of Sm-f state and a minor contribution from In-d and Zn-p states.

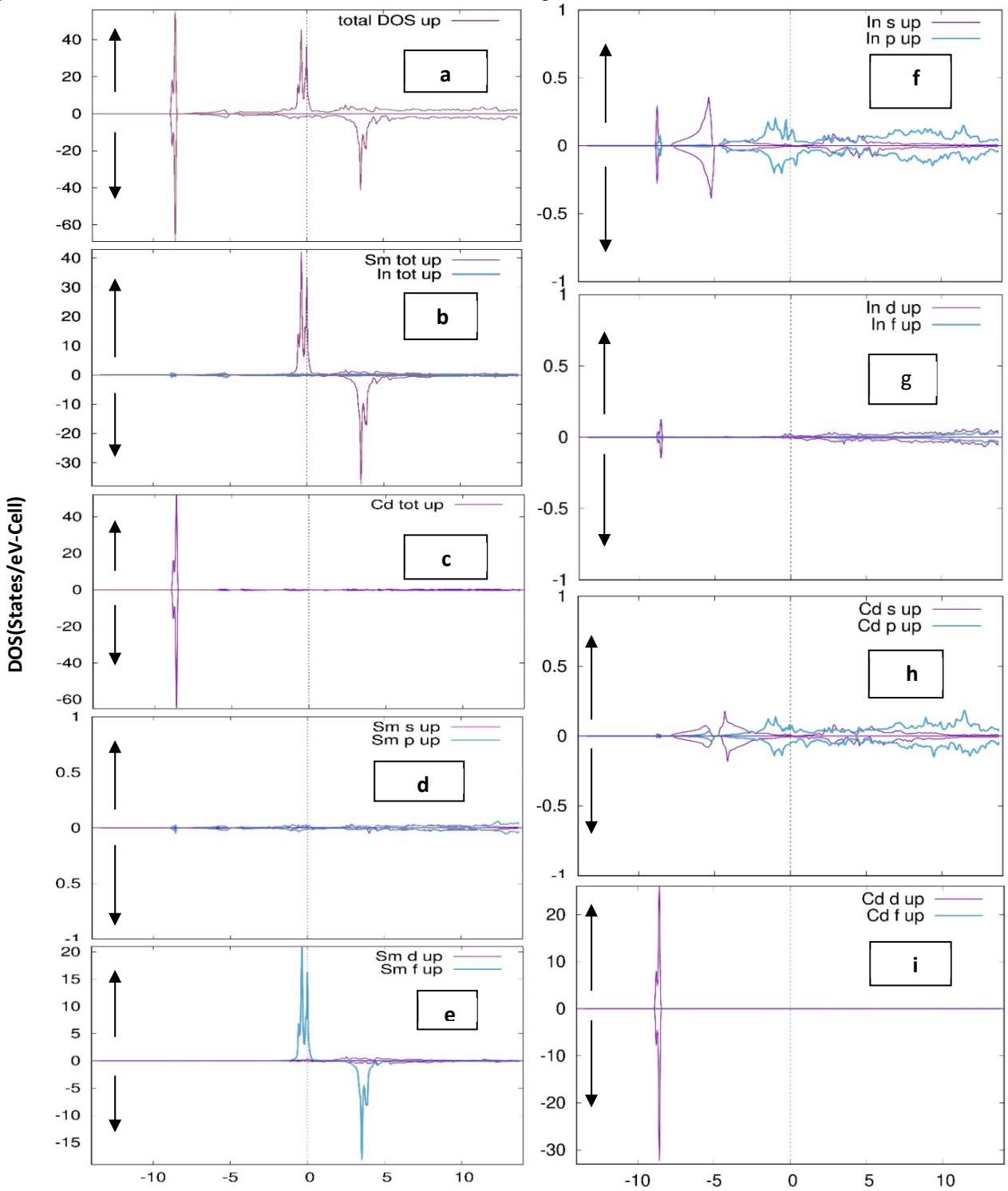

Figure 4. T-DOS and P-DOS for (a) SmInCd -Total (b) Sm-Total & In-Total (c) Cd-Total (d) Sm-s & Sm-p (e) Sm-d & Sm-f (f) In-s & In-p (g) In-d & In-f (h) Cd-s & Cd-p (i) Cd-d & Cd-f.

Now we discuss another peak at around +4e V is caused by spin down state of Sm-f state above the Fermi level. The Fermi level at the origin can be seen in Fig. 4(a-i). It has been found that three sharp peak is at around 0 eV, -1 eV spin up state and -9 electron-volts (eV) in the both state below the Fermi level and also one peak is obtained at around

+4 electron-volts(eV) in the spin down state above the Fermi level. We notice that a sharp peak around -9 eV is caused by the Cd-d states with small contribution In-s and In-d state for both channels. A second peak at about 0 eV and -1 eV is caused by the spin-up state of Sm-f states and a minor contribution from In-p and Cd-p states. Now we discuss another peak at around +4e V is caused by spin down state of Sm-f state above the Fermi level. The Fermi level at the origin can be seen in Fig. 5(a-i).

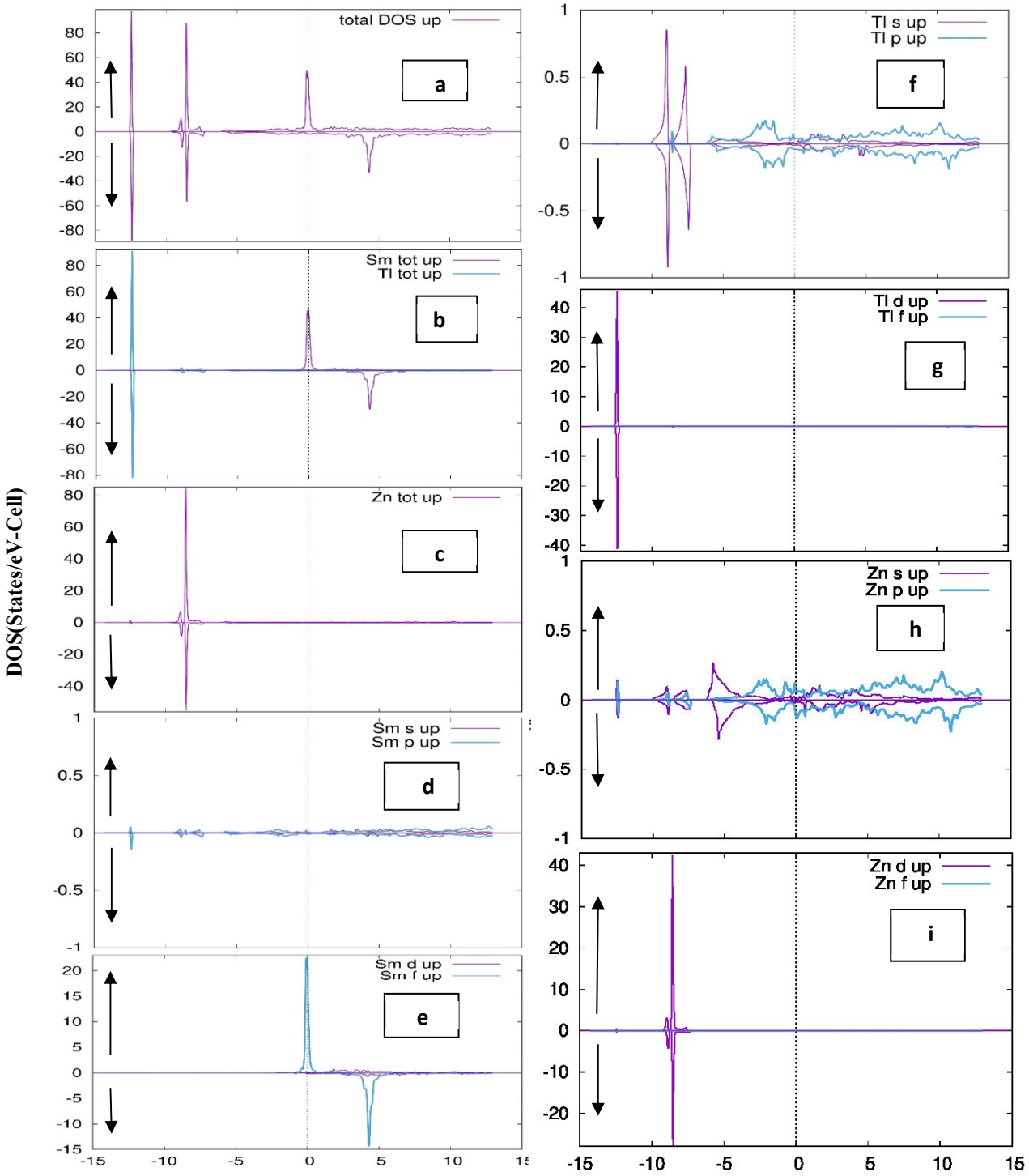

Figure 5. T-DOS and P-DOS for (a) SmTlZn -Total (b) Sm-Total & Tl-Total (c) Zn-Total (d) Sm-s & Sm-p (e) Sm-d & sm-f (f) Tl-s & Tl-p (g) Tl-d & Tl-f (h) Zn-s & Zn-p (i) Zn-d & Zn-f.

It has been found that four sharp peaks are at around -9 eV and -13 electron-volts (eV) in both states below the Fermi level, and also one peak found around 0 eV in the spin up state at Fermi level. And one peak is obtained at around +4 electron-volts (eV) in the spin down state above the Fermi level. We observe that the peak of around -9 eV for both channels below the Fermi level is caused by the Zn-d state with the hybridization of the Zn-s and Tl-s states. Another peak at around -13 eV is caused by the both state of Tl-d states and a minor contribution from Zn-p and Zn-s states. The

peak around 0 eV is caused by spin up state of Sm-f state at Fermi level. Another peak around +4 eV is caused by spin down state of Sm-f state above the Fermi level. Fermi energy has been found that E_F = 0.52524 electron-volts (eV) for SmInZn, E_F = 0.48818 electron-volts (eV) for SmInCd and E_F = 0.54729 electron-volts (eV) for SmTlZn.

Thermodynamics properties

The QHD model, implemented in the Gibbs software package was used to calculate the thermodynamic properties for SmInZn, SmInCd, and SmTlZn compounds within wide range of temperature (0-400 K). Figures 6(a-f) depict temperature dependent thermodynamics characteristics. In thermodynamic properties, we have extracted some important parameters, such as entropy (S), thermal expansion coefficient (α), bulk modulus of material (B), specific heat at constant volume (C_V), and Debye temperature (θ_D). The variation of the bulk modulus with temperature is shown in Fig. 6(a).

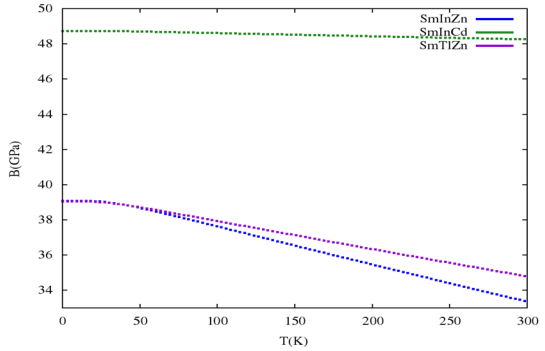

Figure 6(a). Bulk modulus (B) Vs temperature graphs for SmInZn, SmInCd and SmTlZn

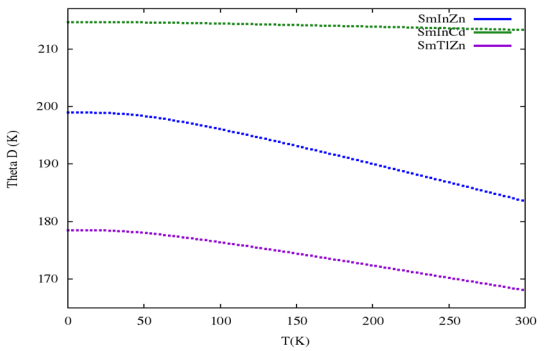

Figure 6(b). Debye temperature (θ_D) Vs temperature graphs for SmInZn, SmInCd and SmTlZn

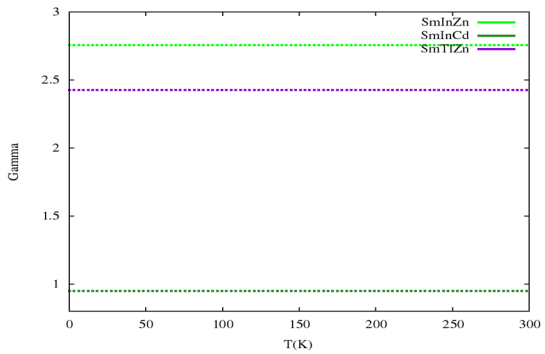

Figure 6(c). Grüneisen parameter (γ) Vs temperature graphs for SmInZn, SmInCd and SmTlZn

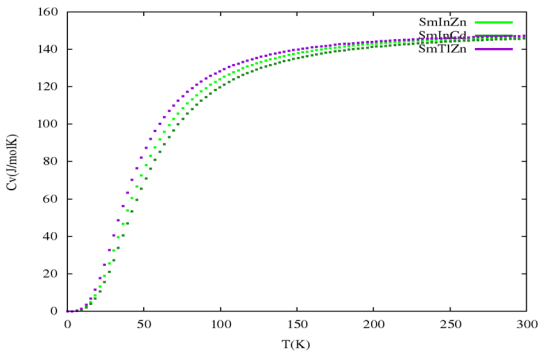

Figure 6(d). Specific heat (C_V) Vs temperature graphs for SmInZn, SmInCd and SmTlZn

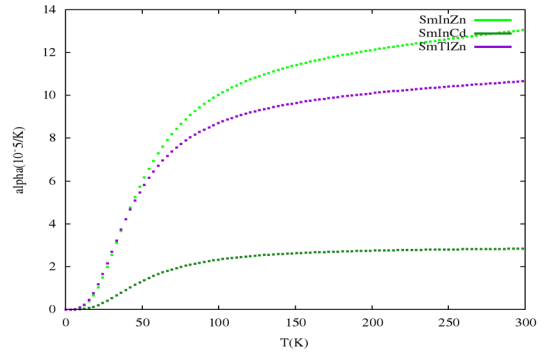

Figure 6(e). Thermal expansion coefficient (α) Vs temperature graphs for SmInZn, SmInCd and SmTlZn

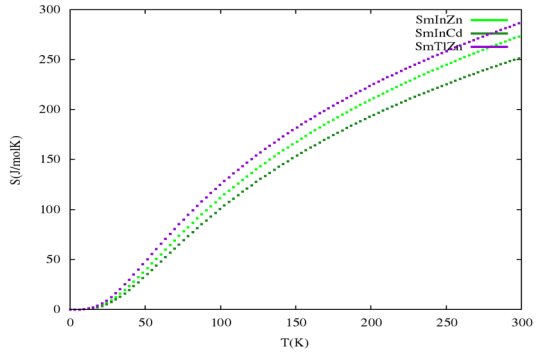

Figure 6(f). Entropy (S) Vs temperature graphs for SmInZn, SmInCd and SmTlZn

These graphs show that as the temperature increases, the bulk modulus (B), decreases. The bulk modulus (B), and compressibility (C), are inversely proportional. So, we can say that as the temperature increases, the compressibility (C), of these compounds will also increase. As a result, Figures 6(a) demonstrates also that as the temperature rises, the three compounds (SmInZn, SmInCd, and SmTlZn) become more compressible, or flexible. Other thermodynamic properties, such as the Debye temperature, provide interesting information about the elastic nature of materials. The relationship between the Debye temperature and temperature is depicted in Figures 6(b), which also demonstrates that for all three compounds.

The Debye temperature (θ_D) gradually decreases as the temperature increases. Additionally, Figs. 6(b) show that SmInZn has a larger θ_D value than SmInCd and SmTlZn, indicating that SmInZn is stiffer than those two metals (as stiff material has a high Debye temperature).

The anharmonicity of crystal lattices under vibrational motion is described by the Grüneisen parameter (γ).

Figures 6(c) indicate how the Grüneisen parameter (γ) changes with temperature and show that it rises with rise in temperature. In the quasi-harmonic Debye model, γ is a function of volume which is depends upon lattice parameters. The dimensions of the lattice and, hence, the volume, grow as the temperature rises so γ also increase with rise in temperature. As a result, increasing temperature raises crystal anharmonicity and the value of γ. A crucial factor that offers crucial insight into the vibrational characteristics and microscopic structure of a crystal is specific heat (C_V).

The variation of specific heat (C_V) is shown in Figures 6 (d) which illustrates how the computed heat capacity at constant volume (C_V) responds to temperature. At temperature ≈ 300 K, it's clear that C_V follows the Debye model relationship (C_V proportional to T^3 law), and beyond T > 300 K, the Dulong-Petit limit is approaching.

The thermal expansion coefficient (α) varies with temperature, as shown in Figures 6(e). it is clear that α increases sharply with temperature when it gets close to 300K. The impact of temperature on the thermal expansion coefficient (α) reduces when temperature rises and exceeding 300 K. when the atoms are moving in a variety of ways. The amount of disorder or irregularity in an atom's or molecule's motion inside a thermodynamic system is described by the entropy(S) Figures 6(f) demonstrate how the entropy (S) for SmInZn, SmInCd, and SmTlZn changes with temperature. Figures 6(f) show that the entropy is zero at absolute zero temperature and that the vibrations inside the thermodynamics system increase as the temperature rises. As a result, the entropy of the system starts to increase rapidly.

CONCLUSIONS

In the current chapter, the DFT approach has been used to examine the electronic properties and quasi-harmonic Debye model has been applied to calculate the thermodynamic characteristics of the SmInZn, SmInCd, and SmTlZn compounds. The following important conclusions have been drawn from the calculations.

SmInZn, SmInCd, and SmTlZn are well stable in hexagonal phase.Equilibrium volume increases from SmInZn → SmTlZn → SmInCd due to increasing lattice parameter from SmInZn → SmTlZn → SmInCd. All three compounds confirm metallic nature due to dominancy of Sm-f spin up bands at the Fermi level. Sm-f spin up bands provide metallic character to these materials. Fermi energies E_F = 0.52524 electron-volts (eV) for SmInZn, E_F = 0.48818 electron-volts (eV) for SmInCd and E_F = 0.54729 electron-volts (eV) for SmTlZn.

Bulk modulus characteristics show that strength of SmInZn, SmInCd, and SmTlZn compounds decreases with temperature and become more flexible with increasing the temperature. The impact of temperature on Debye temperature, θ_D was found to be small on SmInZn and SmInCd while impact of temperature on θ_D is larger in SmTlZn. Thus, SmInZn was found to be stiffer than SmInZn and SmInCd. All three compounds show deviation from harmonic oscillator and SmInZn show larger deviation from harmonic oscillator character compared to SmInCd and SmTlZn. α increases with increasing the temperature due to expansion of unit cell dimensions and hence volume with temperature. The amount of disorder was found to be zero at 0K and increases rapidly with increasing the temperature in these compounds.

ORCID IDs

Aman Kumar, https://orcid.org/0000-0002-8867-6595; **Anuj Kumar**, https://orcid.org/0000-0003-3372-3718
Kamal Kumar, https://orcid.org/0000-0001-8132-5373

REFERENCES

[1] R.D. Hoffmann, and R. Pöttgen, Z. Kristallogr. **216**, 127 (2001).
[2] M.D. Klicpera, F. Malý, I. Puente-Orench, and P. Javorský, J. Alloys Compd. **822**, 153595 (2020). https://doi.org/10.1016/j.jallcom.2019.153595
[3] Mishra, U. Subbarao, S. Roy, S.C. Sarma, D. Mumaddi, S. Sarkar, and S.C. Peter, Inorg. Chem. **57**, 12576 (2018). https://doi.org/10.1021/acs.inorgchem.8b01650
[4] K. Sun, H. Yao, E. Fradkin, and S.A. Kivelson, Phys. Rev. Lett. **103**, 046811 (2009). https://doi.org/10.1103/PhysRevLett.103.046811
[5] L. Bessais, "Structure and Magnetic Properties of Intermetallic Rare-Earth-Transition-Metal Compounds: A Review", Materials, **15**, 201 (2022). https://doi.org/10.3390/ma15010201
[6] E. Burzo, "Exchange Interactions and Transition Metal Moments in Rare-Earth Compounds", J. Synchrotron Investig. **12**, 431 (2018). https://doi.org/10.1134/S1027451018030072
[7] M. Duchna, and I. Cieślik, "Rare Earth Elements in New Advanced Engineering Applications", Rare Earth Elements - Emerging Advances, Technology Utilization, and Resource Procurement, (2022). https://doi.org/10.5772/intechopen.109248
[8] M. Traore, A. Gong, Y. Wang, L. Qiu, Y. Bai, W. Zhao, Y. Liu, et al., "Research progress of rare earth separation methods and technologies", Journal of Rare Earths, (2022). https://doi.org/10.1016/j.jre.2022.04.009
[9] A. Fert, F.N. Van Dau, Comptes Rendus Physique, **20**(7-8), 817 (2019). https://doi.org/10.1016/j.crhy.2019.05.020
[10] V. Balaram, "Rare earth elements: A review of applications, occurrence, exploration, analysis, recycling, and environmental impact", Geoscience Frontiers, **10**(4), 1285 (2019). https://doi.org/10.1016/j.gsf.2018.12.005
[11] G. Barakos, H. Mischo, and J. Gutzmer, *A forward look into the US rare-earth industry; How potential mines can connect to the global REE market?,* Mining Engineering, (2018), pp. 30-37. https://thoriumenergyalliance.com/wp-content/uploads/2020/02/REE-GeorgeNabeelhighlights.pdf

[12] W. Gwenzi, L. Mangori, C. Danha, N. Chaukura, N. Dunjana, and E. Sanganyado, "Sources, behaviour, and environmental and human health risks of high-technology rare earth elements as emerging contaminants", The Science of the Total Environment, **636**, 299-313, (2018). https://doi.org/10.1016/j.scitotenv.2018.04.235
[13] J. Kang, and A.M. Kang, "Trend of the research on rare earth elements in environmental science", Environ. Sci. Pollut. Res. **27**, 14318 (2020). https://doi.org/10.1007/s11356-020-08138-z
[14] M.Y. Raïâ, R. Masrour, A. Jabar, M. Hamedoun, A. Rezzouk, A. Hourmatallah, N. Benzakour, et al., Journal of Physics and Chemistry of Solids, **163**, 110581 (2022). https://doi.org/10.1016/j.jpcs.2022.110581
[15] M. Jirsa, M. Rameš, and M. Muralidhar, Acta Phys. Pol. A, **113**, 223 (2008). http://przyrbwn.icm.edu.pl/APP/PDF/113/a113z1054.pdf
[16] D.J. García, V. Vildosola, and P. Cornaglia, Condensed Matter, **32**(28), 285803 (2019). https://doi.org/10.1088/1361-648X/ab7e5a
[17] X.B. Liu, and Z. Altounian, "First-principles calculation on the Curie temperature of GdFeSi", J. Appl. Phys. **107**, 09E103 (2010). https://doi.org/10.1063/1.3364048
[18] S. Talakesh, and Z. Nourbakhsh, "The density functional study of structural, electronic, magnetic and Thermodynamic properties of XFeSi (X=Gd, Tb, La) and GdRuSi compounds", J. Supercond. Novel Magn. **30**, 2143 (2017). https://doi.org/10.1007/s10948-017-3976-x
[19] V.K. Pecharsky, and K.A. Gschneidner Jr, "Magnetocaloric effect and magnetic refrigeration", J. Magn. Magn. Mater. **44-56**, 200 (1999). https://doi.org/10.1016/S0304-8853(99)00397-2
[20] J. Du, Q. Zheng, Y. Li, Q. Zhang, D. Li, and Z. Zhang, "Large magnetocaloric effect and enhanced magnetic refrigeration in ternary Gd-based bulk metallic glasses", J. Appl. Phys. **103**, 023918 (2008). https://doi.org/10.1063/1.2836956
[21] V. Franco, J.S. Blázquez, J.J. Ipus, J.Y. Law, L.M. Moreno-Ramírez, and A. Conde, Prog. Mater. Sci. **93**, 112 (2018). https://doi.org/10.1016/j.pmatsci.2017.10.005
[22] A. Mahmood, M. Rashid, K. Safder, M.W. Iqbal, N.A. Noor, S.M. Ramay, W. Al-Masry, et al., Results in Physics, **20**, 103709 (2021). https://doi.org/10.1016/j.rinp.2020.103709
[23] P. Blaha, K. Schwarz, G.K.H. Madsen, D. Kuasnicka, and J. Luitz, *WIEN2k An Augmented Plane Wave-Local Orbitals Program for Calculating Crystal Properties*, (K. Schwarz Technical Universitat, Wien Austria, 2001). ISBN: 3-9501031 1-2
[24] D.J. Singh, and L. Nordstrom, *Plane Waves Pseudo Potentials and the LAPW Method*, (Springer, New York, 2006).
[25] K. Schwarz, "DFT calculations of solids with LAPW and WIEN2k", J. Solid State Chemistry, **176**, 319 (2003). https://doi.org/10.1016/S0022-4596(03)00213-5
[26] A. Otero-de-la-Roza, and, D. Abbasi-Pérez, and V. Luaña, "GIBBS2: A new version of the quasiharmonic model code. II. Models for solid-state thermodynamics, features, and implementation", Computer Physics Communications, **182**. 2232 (2011). https://doi.org/10.1016/j.cpc.2011.05.009
[27] W. Kohn, and L.J. Sham, Phys. Rev. **140**, A1133 (1965). https://doi.org/10.1103/PhysRev.140.A1133
[28] P. Blaha, K. Schwarz, G.K.H. Madsen, D. Kvasnicka, and J. Luitz, *WIEN2k, An Augmented Plane Wave Plus Local Orbital Program for Calculating Crystal Properties*, (Vienna University of Technology, Vienna, 2001).
[29] J.P. Perdew, K. Burke, and M. Ernzerhof, Phys. Rev. Lett. **77**, 3865 (1996). https://doi.org/10.1103/PhysRevLett.77.3865
[30] F.D. Murnaghan, Proc. Natl. Acad. Sci. U.S.A. **30**, 244 (1994). https://doi.org/10.1073%2Fpnas.30.9.244
[31] K. Hartjes, and W. Jeitschko, J. Alloys Compd. **226**, 81 (1995). https://doi.org/10.1016/0925-8388(95)01573-6

ЕЛЕКТРОННІ ТА ТЕРМОДИНАМІЧНІ ВЛАСТИВОСТІ ПОТРІЙНИХ РІДКІСНОЗЕМЕЛЬНИХ СПЛАВІВ

Аман Кумар[a], Анудж Кумар[b], Камал Кумар[c], Ріші Пал Сінгх[d], Ріту Сінгх[e], Раджеш Кумар[f]
[a]Факультет фізики, Науковий коледж Керала Верми Субхарті, Університет Свамі Вівекананда Субхарті, Мірут, Уттар-Прадеш, Індія
[b]Факультет фізики, Махамайя Державний коледж, Шеркот, Бійнор, Уттар-Прадеш, Індія
[c]Факультет фізики, D.A.V College Kanpur, Уттар-Прадеш, Індія
[d]Факультет фізики, S. S. V. College, Хапур 245101, Уттар-Прадеш, Індія
[e]Факультет хімії, S. S. V. Коледж, Хапур 245101, Уттар-Прадеш, Індія
[f]Факультет фізики, Державний коледж, Нанаута, Сахаранпур, Уттар-Прадеш, Pin-247452, Індія

У цій статті використовується підхід FP-LAPW в рамках методу DFT і квазігармонійна модель Дебая для дослідження електронних і термодинамічних властивостей інтерметалічних рідкоземельних матеріалів таких як SmInZn, SmInCd і SmTlZn. Термодинамічні властивості були визначені за допомогою квазігармонічної моделі Дебая, тоді як підходи FP-LAPW в рамках методу DFT були використані для отримання електронних властивостей. Розраховані структурні параметри та наявні експериментальні дані були досліджені, і було помічено, що існує хороша узгодженість між доступними експериментальними та розрахунковими значеннями структурних параметрів. Електронна поведінка сполук SmInZn, SmInCd та SmTlZn демонструє металевий характер. Ми розглянули кілька термодинамічних характеристик. Усі розраховані характеристики збігаються з експериментальними або теоретичними розрахунками.

Ключові слова: *електроніка; інтерметаліди; щільність стану; DFT*

East European Journal of Physics. 1. 118-124 (2023)
DOI:10.26565/2312-4334-2023-1-14 ISSN 2312-4334

A QUALITATIVE THEORETICAL STUDY OF INORGANIC HTM-FREE $RbGeI_3$ BASED PEROVSKITE SOLAR CELLS USING SCAPS-1D AS A PATHWAY TOWARDS 3.601% EFFICIENCY†

Mary T. Ekwu[a], Eli Danladi[b], Nicholas N. Tasie[c], Idoko S. Haruna[d], Osaretin E. Okoro[d], Philibus M. Gyuk[e], Olayinka M. Jimoh[f], Rita C. Obasi[d]

[a]*Department of Physics, Airforce Institute of Technology, Kaduna, Nigeria*
[b]*Department of Physics, Federal University of Health Sciences, Otukpo, Benue State, Nigeria*
[c]*Department of Physics, Rivers State University, Port Harcourt, Rivers State, Nigeria*
[d]*Centre for Satellite Technology Development-NASRDA, Abuja, Nigeria*
[e]*Department of Physics, Kaduna State University, Kaduna, Nigeria*
[f]*Department of Physics, Federal University, Dutsin-Ma, Katsina State, Nigeria*
**Corresponding Author: danladielibako@gmail.com, tel.: +2348063307256*
Received January 20, 2023; revised January 28, 2023; accepted January 31, 2023

The presence of toxic lead in perovskite solar cells has hindered its commercial viability. In this present work, a mesoscopic inorganic lead-free perovskite solar cells based on $RbGeI_3$ was proposed and implemented using SCAPs simulation tool. The effect of electron transport material (ETM) and Absorber thickness were analyzed. When the device was first simulated, its power conversion efficiency (PCE), fill factor (FF), current density (J_{sc}), and open circuit voltage (V_{oc}) all reached values of 3.584% for PCE, 48.477% for FF, 25.385 mA/cm^2 for J_{sc}, and 0.291 V for V_{oc}. When the ETM and absorber are at their ideal thicknesses of 0.08 μm and 0.40 μm , the development of efficiency becomes stable. Using the aforementioned parameters, the optimized PSC device produced the following values: PCE = 3.601%, J_{sc} = 25.386 mA/cm^2, V_{oc} = 0.291 V, and FF = 48.637%. The PCE improvement over the basic device without optimization is around 1.01 times. The findings indicate that perovskite solar cell lacking HTM has a substantial capacity to absorb photon energy and produce electrons. It has also shown how to create environmentally clean and economically viable technology.
Keywords: *perovskite solar cells; $RbGeI_3$; SCAPS; layer thickness*
PACS: 41.20.Cv; 61.43.Bn; 68.55.ag; 68.55.jd; 73.25.+i; 72.80.Tm

1. INTRODUCTION

Organic-inorganic halide perovskites have attracted a lot of scientific interest due to their many benefits, such as their high coefficient of absorption, good solution processability, simplicity in synthesis, variable bandgap, and long diffusion length, to name just a few [1-3]. With a power conversion efficiency of 3.8%, Kojima et al. published the first study on their use in solar cells in 2009 [4].

In the past decade, a transformation in efficiency has risen to a value exceeding 25% [5-7]. However, the presence of toxic lead in perovskite absorber is considered as one of the major drawbacks towards its commercial viability. To carter for such problem, researchers have invested much efforts on other cations that are divalent among which are $Sn^{2+}$and Ge^{2+}, whose oxidation state is +2 and some of their properties close to that of lead [8].

$Sn^{2+}$and Ge^{2+} both have ionic radius smaller than Pb^{2+} with Sn^{2+} to be (1.35 Å), Ge^{2+} to be (0.73 Å) and Pb^{2+} to be (1.49 Å), so when Sn^{2+} and Ge^{2+} act as divalent cations to replace Pb^{2+}, it will not destroy the perovskite crystal structure [5, 9]. The ionic radius of Ge^{2+} is smaller than that of Sn^{2+} and Pb^{2+}, indicating that Ge-based perovskites have higher conductivity than Pb-based and Sn-based perovskites. Saikia et al. studied the effect of thickness, defect concentration, and dopant concentration on $CsGeI_3$-based PSCs [10]. Krishnamoorthy et al. fabricated $CsGeI_3$-based PSCs for the first time and achieved a PCE of 0.11%, which can be seen as a result of Ge^{2+} oxidation during fabrication [11]. Jayan and Sabastian [12] determined the optoelectronic, thermodynamic, structural, thermoelectric, and mechanical properties of $RbGeI_3$ perovskites as a function of various exchange correlations. Pindolia et al. investigated the effect of different hole transport materials (HTM) and electron transport materials (ETM) with $RbGeI_3$ as the light absorbing layer [5].

The instability in perovskite solar cells which is seen to result from organic compounds has been a major problem in the photovoltaic horizon [13, 14]. The commonly used HTM, Spiro-OMeTAD, involves a complex synthetic route with yields below 40% [5, 15, 16]. Organic charge transport materials become unstable under ambient conditions and light exposure [5, 17-20]. Devices without HTM are practical solutions to the problem of the expensive and unstable Spiro-OMeTAD that has limited the commercialization of PSCs technologies due to structural complexity, high cost, and poor stability. Etgar et al. created the first HTM-free PSC by using a Pb-based perovskite absorber as both a light harvester and a hole transport material at the same time [21]. To the best of our research knowledge, the utilization of $RbGeI_3$ as a perovskite absorber in a hole transport free structure has not been reported. In this research paper, an inorganic $RbGeI_3$ based PSC was investigated without HTM. The structure was proposed and implemented using SCAPS-1D software. By utilizing TiO_2 as ETM, fluorine doped tin oxide (FTO) as front contact and silver (Ag) as back contact, two layers'

† ***Cite as:*** M.T. Ekwu, E. Danladi, N.N. Tasie, I.S. Haruna, O.E. Okoro, P.M. Gyuk, O.M. Jimoh, and R.C. Obasi, East Eur. J. Phys. **1**, 118 (2023), https://doi.org/10.26565/2312-4334-2023-1-14

properties such as thickness of ETM and thickness of perovskite layer were optimized to obtain a PCE of 3.601%, FF of 48.637%, J_{sc} of 25.386 mA/cm^2 and V_{oc} of 0.291 V. The manuscript is categorized into four sections which include, the introduction, theoretical method & simulations, results and discussions and the conclusion part.

2. THEORETICAL METHODS AND DEVICE STRUCTURE

In this study, SCAPS-1D software version 3.3.10 was used to carry out the simulation. This software is based on basic semiconductor equations: the Poisson equation and the continuity equation of both charge carriers (holes and electrons) under steady-state condition [1].

The proposed device follows the configuration of FTO/TiO_2/$RbGeI_3$/Ag, which is depicted in Figure 1. Starting from illumination point, FTO is used as a front contact, ETL as TiO_2, the absorber layer as $RbGeI_3$ and silver (Ag) as the back contact. The front electrode's work function is 4.40 eV, whereas the counter electrode's work function is 4.63 eV. The simulation was run with an A.M. 1.5 spectrum light intensity (1000 W/m^2), a simulation temperature of 300 K, a simulation frequency of 1×10^{16} Hz, and a scanning voltage range of 0 to 1.40 V. Tables 1 and 2 summarized the information for each layer and the interface settings.

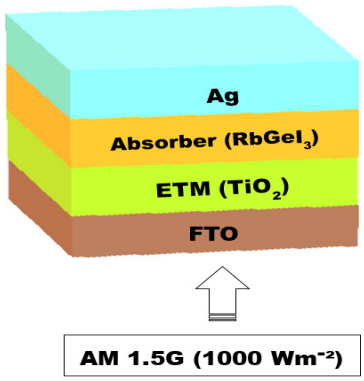

Figure 1. Device structure

Table 1. Variables utilized in SCAPS-1D simulations of perovskite solar cell architecture [1, 2, 5]

Parameters	FTO	TiO_2	$RbGeI_3$
Thickness (μm)	0.4	0.05	0.4
Band gap energy E_g (eV)	3.5	3.2	1.31
Electron affinity χ (eV)	4.3	4.2	3.9
Relative permittivity ϵ_r	9	10	23.01
Effective conduction band density N_c (cm^{-3})	2.2×10^{18}	2.2×10^{18}	2.8×10^{19}
Effective valance band density N_v (cm^{-3})	1.8×10^{19}	2.2×10^{18}	1.4×10^{19}
Electron thermal velocity (cm/s)	1.0×10^{7}	1.0×10^{7}	1.0×10^{7}
Hole thermal velocity (cm/s)	1.0×10^{7}	1.0×10^{7}	1.0×10^{7}
Electron mobility μ_n (cm^2 V^{-1} s^{-1})	20	20	28.6
Hole mobility μ_p (cm^2 V^{-1} s^{-1})	10	10	27.3
Donor concentration N_D (cm^{-3})	1.0×10^{18}	1×10^{17}	0
Acceptor concentration N_A (cm^{-3})	0	0	1×10^{9}
Defect density N_t (cm^{-3})	1×10^{15}	1×10^{15}	1×10^{15}

Table 2. Defect parameter values of the interfaces of the device

Parameters	TiO_2/$RbGeI_3$ interface
Defect type	Neutral
Capture cross section for electrons (cm^2)	1×10^{-18}
Capture cross section for holes (cm^2)	1×10^{-16}
Energetic distribution	Single
Energy level with respect to E_v (eV)	0.600
Characteristic energy (eV)	0.1
Total density (cm^{-3})	1×10^{12}

3. RESULTS AND DISCUSSIONS

3.1. Initial simulation

In accordance to the parameters presented in Tables 1 and 2, the initial device characteristics are shown in Figure 2. Figure 2a shows the current density-voltage (*J-V*) curve, Figure 2b shows the quantum efficiency (QE) curve with respect to wavelength, Figure 2c shows the quantum efficiency curve with respect to photon energy and Figure 2d shows the calculated energy band diagram profile. In this initial simulation, we ignored the reflection of each layer, as well as the interface and the additional series resistance brought on by front contact or back contact.

The incidence to photon conversion efficiency curve with respect to wavelength is shown in Figure 2b for the initial device. Based on the given curve in Figure 2c, the band gap energy of $RbGeI_3$ is 1.31 eV, which is narrower than the lead-based counter part of 1.55 eV, and this results to a red shift in the absorption wavelength of the lead-free perovskite absorber to 900 nm. The curve sweeps across the visible range of the electromagnetic spectrum, and the absorption from 380 to 780 nm is the strongest, seen above 78%, which is in good agreement with the QE spectrum in similar literature [5].

Based on the values listed in Tables 1 and 2, the band gap profile was calculated and is shown in Figure 2d. The highest energy level of the valence band is represented by E_v (eV), and the lowest energy level of the conduction band is represented by E_c (eV). The offset energy of the valance band is 2.186 eV while the interface conduction band offset is 0.319 eV. The offset value existing between valance band of $RbGeI_3$ and ETL prevents the positive charges from flowing to the TiO_2 side from the absorber layer whereas the offset value at their conduction band blocks the electron from diffusing to the absorber from the TiO_2. Thus, the recombination processes at the interface are minimal thereby resulting to good photovoltaic performance.

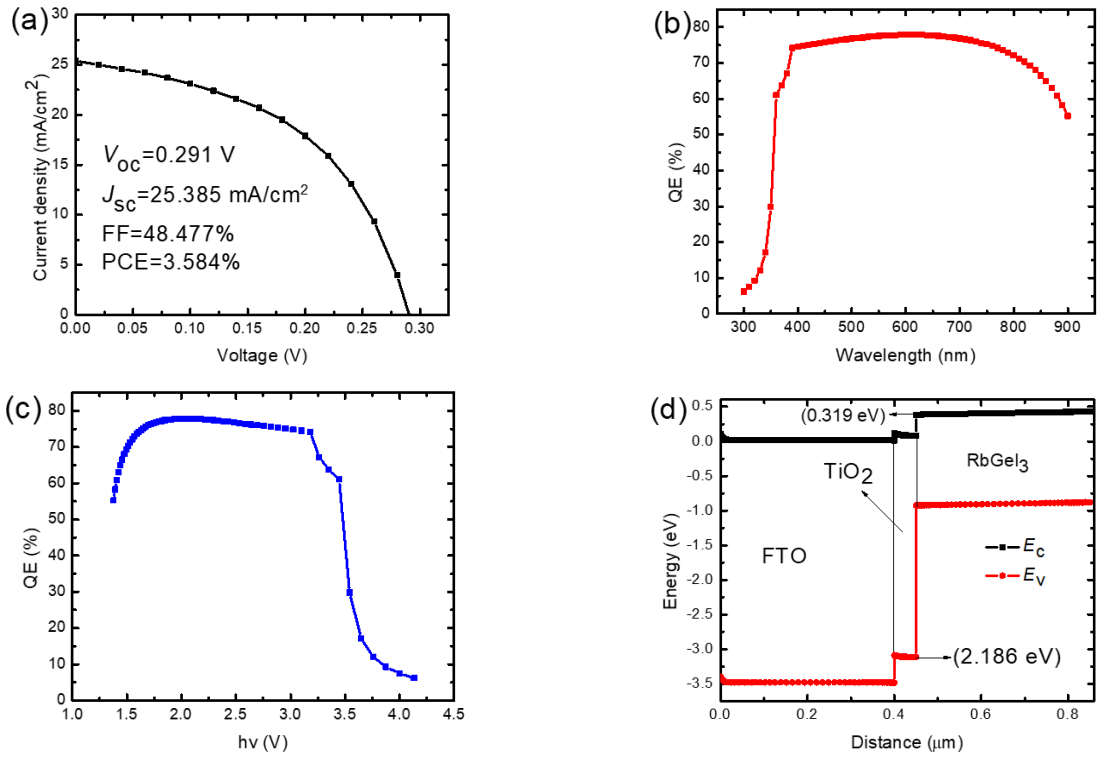

Figure 2. (a) *J-V* curve under illumination for initial device, (b) QE versus wavelength for initial device, (c) QE versus photon energy for the initial device and (d) energy profile diagram of the initial device

3.2. Effect of changing ETM thickness

To understand the influence of ETM thickness on PCE of the proposed PSC, we utilized the parameters in Tables 1 & 2 for the simulation while varying the thickness from 10 to 100 nm. The results are presented in Table 3 and Figure 3. The quantum efficiency versus wavelength curve is depicted in Figure 3b. The simulated results of our study show that PCE increased with increasing TiO_2 thickness from 10 to 80 nm before it starts decreasing. This decrease is attributed to lower transmittance at excessive values of ETM thickness that prohibit solar radiation from reaching the perovskite skeleton and partial TiO_2 layer absorption of incident light [1]. From Table 3 and Figure 3a, it can be seen that the 80 nm thickness gave V_{oc} = 0.291 V, J_{sc} = 25.385 mA/cm^2, FF = 48.637%, and PCE = 3.598%.

Table 3. *J-V* characteristic parameters with the variation of thickness of ETM

Thickness (μm)	PCE (%)	*FF* (%)	J_{sc} (mA/cm^2)	V_{oc} (V)
0.01	3.195	44.885	21.981	0.285
0.02	3.370	46.486	25.106	0.289
0.03	3.499	47.689	25.260	0.290
0.04	3.560	48.248	25.349	0.291
0.05	3.584	48.477	25.385	0.291
0.06	3.594	48.576	25.394	0.291
0.07	3.597	48.618	25.392	0.291
0.08	3.598	48.637	25.385	0.291
0.09	3.597	48.645	25.377	0.291
0.10	3.596	48.649	25.367	0.291

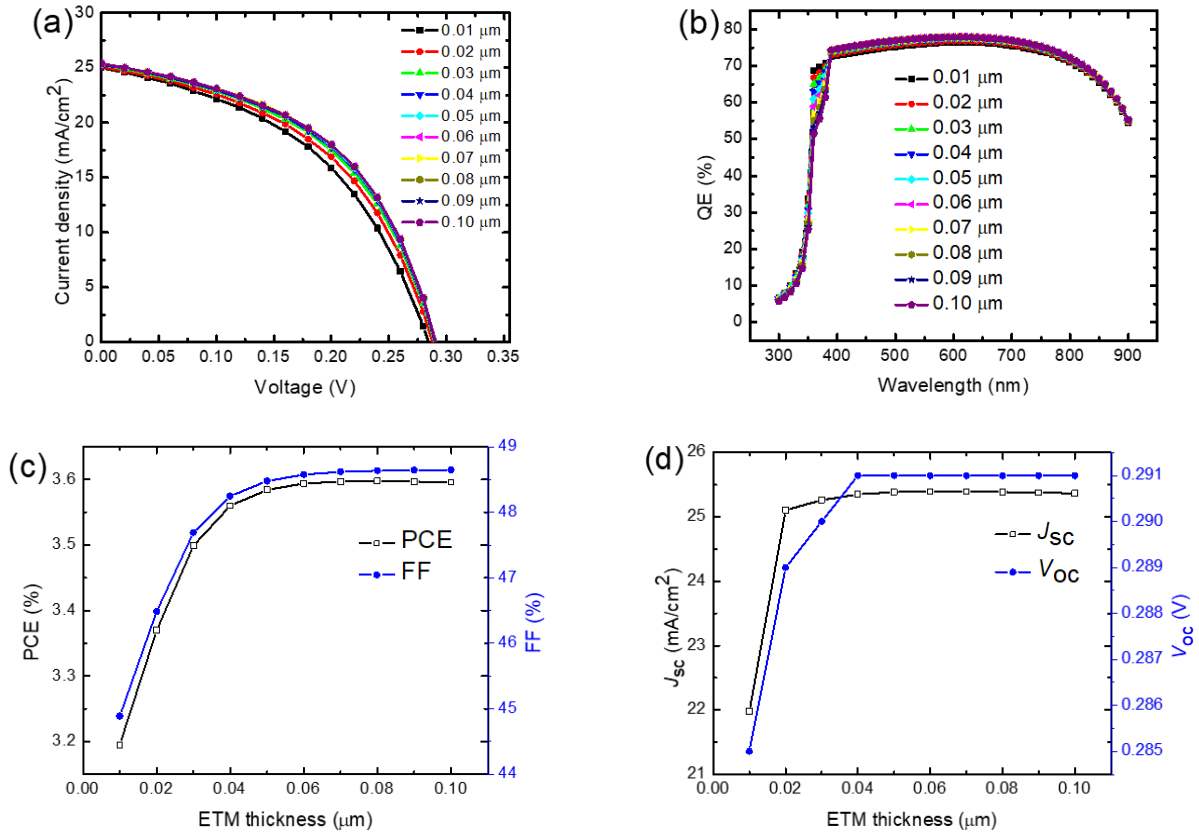

Figure 3. (a) *J-V* curve under illumination with different ETM thickness, (b) QE versus wavelength, (c) variation of ETM thickness with PCE and FF, and (c) variation of ETM thickness with J_{sc} and V_{oc}

The QE is a crucial property of solar cell, which shows the ratio of the electron–hole pairs collected to the number of striking photons [2]. QE is seen as a function of wavelength in nm or photon energy in eV. The curve was measured within the wavelength range of 300-900 nm. The simulated QE increased from 5% at 300 nm to a maximum of 78% at 600 nm but gradually decreases to 60% at a wavelength value of 900 nm. The absorption is within the visible and near infrared region. The correlation between the PCE and FF with respect to thickness is shown in Figure 3c and the relationship between J_{sc} and V_{oc} with thickness is shown in Figure 3d.

3.3. Effect of changing absorber layer thickness

One of the important parameters that should not be overlooked in choice for good device performance is the perovskite layer thickness. This thickness is affected by the diffusion lengths and life-time of the photo-generated electrons and holes [22, 23], as such should be properly chosen. For its influence in solar cells to be fully explored, the layer thickness was controlled in the range of 100–1000 nm while maintaining other parameters fixed as shown in Tables 1 & 2.

Figure 4a shows the *J-V* curves of the simulated device with varied $RbGeI_3$ layer thicknesses. As can be seen from the curve, when the absorber layer is increased, the J_{sc} increases significantly upto thickness of 500 nm, after which the J_{sc} value tends to have a downward trend as the absorbing layer thickness keeps increasing, which shows that absorber layer exceeding 500 nm encourages charge recombination. This rise in J_{sc} is due to a significant photon absorption in this range (as seen by the QE-wavelength curve). Along with the increase in absorber layer thickness from 100 to 400 nm, we also observed a rise in PCE. The thicker perovskite layer absorbs enough photons to produce charge carriers when the absorption layer thickness of the perovskite layer rises above 400 nm.

The PCE curve, however, tends to become flatter as absorption layer thickness increases due to increased recombination and diffusion length. The carriers may recombine before reaching the metal electrode if the thickness of the absorption layer is greater than the diffusion length of the carrier [22].

The research above determined the ideal value for the thickness of the absorber layer used for additional simulation and taken into account to be 400 nm (see Table 4). Due to a rise in series resistance, the value of FF as a function of absorber layer thickness decreases [22].

The impact of the $RbGeI_3$ layer's thickness on the QE (%) with respect to wavelength is depicted in Figure 4b. Since the absorption grows more potent and quantum efficiency also rises with thickness, carrier extraction rises along with thickness. Figure 4c displays the relationship between the PCE and FF with regard to thickness, whereas Figure 4d displays the relationship between the J_{sc} and V_{oc} with respect to thickness.

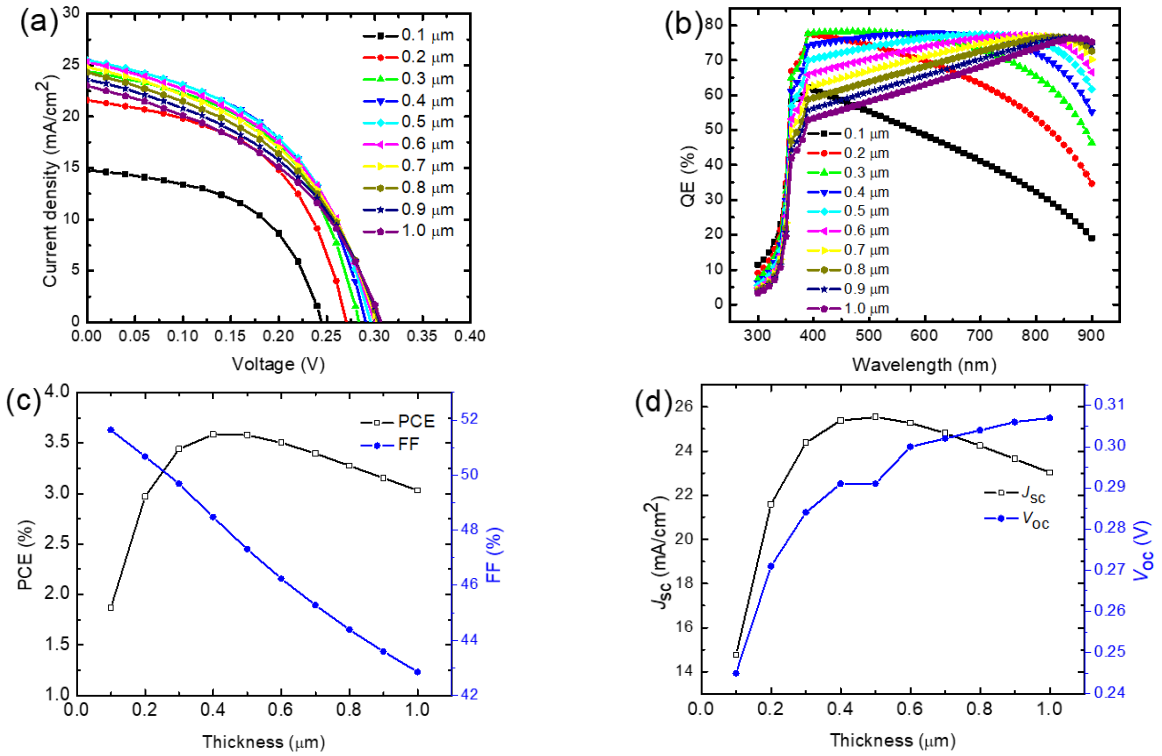

Figure 4. (a) *J-V* curve under illumination with different absorber thickness, and (b) QE versus wavelength, (c) variation of ETM thickness with PCE and FF, and (d) variation of ETM thickness with J_{sc} and V_{oc}

Table 4. *J-V* characteristic parameters with the variation of thickness of Absorber

Thickness (μm)	PCE (%)	*FF* (%)	J_{sc} (mA/cm^2)	V_{oc} (V)
0.1	1.870	51.638	14.767	0.245
0.2	2.969	50.677	21.594	0.271
0.3	3.440	49.687	24.384	0.284
0.4	3.584	48.477	25.385	0.291
0.5	3.579	47.311	25.541	0.291
0.6	3.503	46.239	25.282	0.300
0.7	3.396	45.279	24.815	0.302
0.8	3.274	44.387	24.251	0.304
0.9	3.152	43.593	23.646	0.306
1.0	3.030	42.853	23.029	0.307

3.4. Performance of the optimized device

Figure 5 shows the curve of the optimized (black color) and initial (red color) device. The optimized ETM thickness is 80 nm while the optimized $RbGeI_3$ layer thickness is 400 nm.

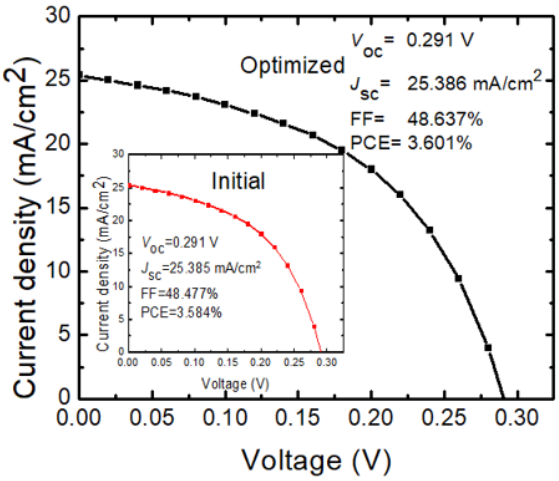

Figure 5. The initial and optimized *J–V* curves

The optimized device gave a PCE of 3.601%, J_{sc} of 25.386 mA/cm^2, V_{oc} of 0.291 V, and FF of 48.637%. This shows an improvement of ~ 1.01 times in PCE over the initial device without optimization. The results obtained demonstrate that, ETM and absorber thickness have crucial role in improving the performance of $RbGeI_3$ HTM free perovskite solar cell. This can provide proper guidance to researchers involved in experimental development of perovskite solar cells for realizing high performance.

3.5. Influence of temperature on the performance of the optimized PSC device

To explore the properties of the optimized device, we simulated the device at different temperature which include 240, 250, 260, 270, 280, 290, 300, 310 and 320 K. Figure 6a depicts the *J-V* behavior, while Figures 6b-f show the power density with the changing temperature, variation of the PCE

with the temperature, correlation of the FF with respect to the temperature, variation of J_{sc} with the temperature and correlation of the V_{oc} with respect to the temperature. The performance of the device is significantly impacted by temperature changes, as can be readily shown in Table 5. With an increase in temperature, the V_{oc}, J_{sc}, and PCE continuously decrease. The increase in saturation current, which also causes an increase in recombination rate, is responsible for these observed properties [24]. Low PCE and J_{sc} are a result of recombination, which has an impact on the carrier concentration, electron and hole mobilities, and the ability of the electron to reach the depletion area [1, 2]. The increase in flaws with rising temperature is thought to be the cause of the observed drop in V_{oc}.

Table 5. *J-V* characteristic parameters with temperature variation

Temperature (K)	PCE (%)	*FF* (%)	J_{sc} (mA/cm^2)	V_{oc} (V)
240	4.674	48.047	26.776	0.363
250	4.511	47.782	26.558	0.355
260	4.335	47.597	26.337	0.346
270	4.160	47.650	26.112	0.334
280	3.992	47.991	25.885	0.321
290	3.787	48.099	25.655	0.307
300	3.601	48.637	25.386	0.291
310	3.363	48.537	25.178	0.275
320	3.152	48.906	24.933	0.258

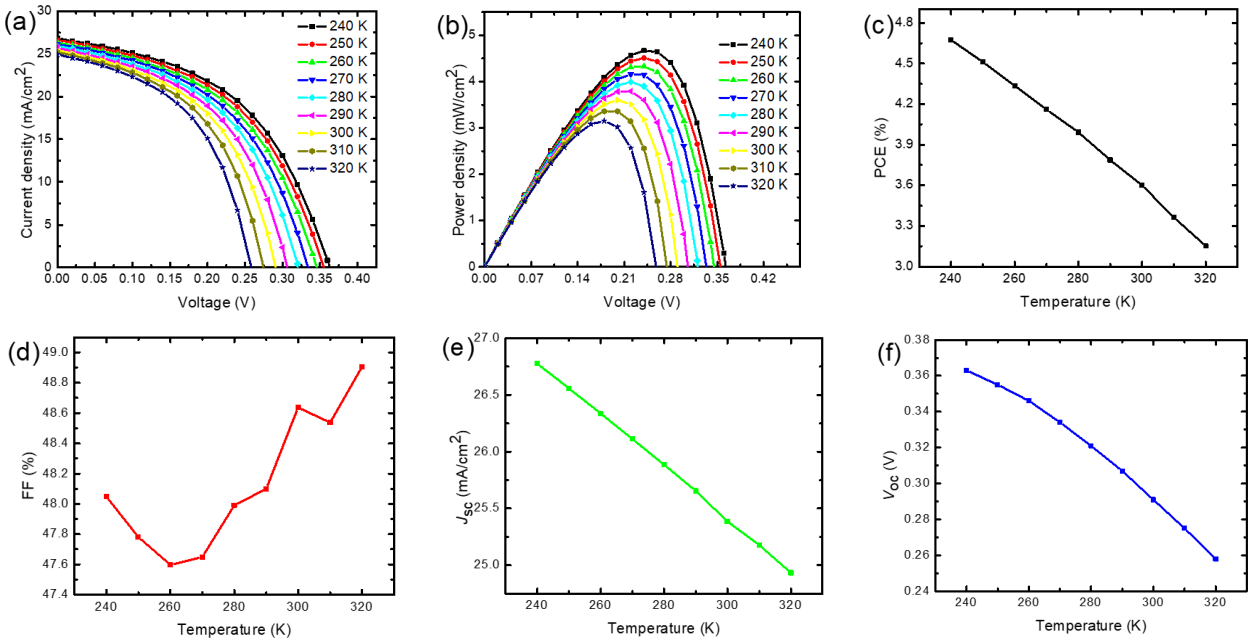

Figure 6. (a) *J-V* curve with varied temperature under illumination, (b) *P-V* curve with varied temperature under illumination (c) PCE with respect to temperature, (d) FF with respect to temperature, (e) J_{sc} with respect to temperature and (f) V_{oc} with respect to temperature

4. CONCLUSION

We utilized SCAPS software which is based on the three basic equations of semiconductor to simulate the proposed HTM-free $RbGeI_3$ PSC structure. On initial device simulation, its power conversion efficiency, fill factor, current density and open circuit voltage attained values of 3.584%, 48.477%, 25.385 mA/cm^2 and 0.291 V. For the solar cell device to be optimized, the ETM and $RbGeI_3$ thicknesses were varied individually from 10 to 100 nm and from 100 to 1000 nm while keeping other parameters fixed. The optimized thickness of ETM was 80 nm and the optimized thickness of $RbGeI_3$ was 400 nm. The optimized PSC device using the aforementioned parameters gave a PCE of 3.601%, J_{sc} of 25.386 mA/cm^2, V_{oc} of 0.291 V, and FF of 48.637% respectively. The performance of the optimized device is greatly affected by the temperature. Increase in temperature leads to decrease in PCE, J_{sc} and V_{oc}.

Acknowledgement

The authors would like to thank Professor Marc Burgelman, Department of Electronics and Information Systems, University of Ghent for the development of the SCAPS software package and allowing its use.

Funding. This article did not receive any funding support.
Conflict of interest. Authors have declared that there is no conflict of interest.

ORCID IDs

Eli Danladi, https://orcid.org/0000-0001-5109-4690; **Nicholas N. Tasie**, https://orcid.org/0000-0001-8398-2596

REFERENCES

[1] E. Danladi, M. Kashif, A. Ichoja, and B.B. Ayiya, Transactions of Tianjin University, **28**(5), (2022). https://doi.org/10.1007/s12209-022-00343-w
[2] E. Danladi, M. Kashif, T.O Daniel, C.U. Achem, M. Alpha, and M. Gyan, East European Journal of Physics, **3**, 19 (2022). https://doi.org/10.26565/2312-4334-2022-3-03
[3] Z. Qu, F. Ma, Y. Zhao, X. Chu, S. Yu, and J. You, Chinese Physics Letters, **38**, 107801 (2021). https://doi.org/10.1088/0256-307X/38/10/107801
[4] A. Kojima, K. Teshima, Y. Shirai, and T. Miyasaka, Journal of American Chemical Society, **131**, 6050 (2009). https://doi.org/10.1021/ja809598r
[5] G. Pindolia, S.M. Shinde, P.K. Jha, Solar Energy, **236**, 802 (2022). https://doi.org/10.1016/j.solener.2022.03.053
[6] J. Wu, Y. Li, Y. Li, W. Xie, J. Shi, D. Li, S. Cheng, and Q. Meng, Journal of Materials Chemistry A, **9**, 6382 (2021). https://doi.org/10.1039/D0TA12046D
[7] J.J. Yoo, G. Seo, M.R. Chua, T.G. Park, Y. Lu, F. Rotermund, Y.K. Kim, et al., Nature, **590**(7847), 587 (2021). https://doi.org/10.1038/s41586-021-03285-w
[8] W. Ke, and M.G. Kanatzidis, Nature Communications, **10**, 965 (2019). https://doi.org/10.1038/s41467-019-08918-3
[9] N.K. Noel, S.D. Stranks, A. Abate, C. Wehrenfennig, S. Guarnera, A.A. Haghighirad, A. Sadhanala, G.E. Eperon, S.K. Pathak, M.B. Johnston, A. Petrozza, L.M. Herz, and H.J. Snaith, Energy & Environmental Science, **7**, 3061 (2014). https://doi.org/10.1039/C4EE01076K
[10] D. Saikia, J. Bera, A. Betal, and S. Sahu, Optical Materials, **123**, 111839 (2022). https://doi.org/10.1016/j.optmat.2021.111839
[11] T. Krishnamoorthy, H. Ding, C. Yan, W.L. Leong, T. Baikie, Z. Zhang, M. Sherburne, S. Li, M. Asta, N. Mathews, and S.G. Mhaisalkar, Journal of Materials Chemistry A, **3**, 23829 (2015). https://doi.org/10.1039/C5TA05741H
[12] D.K. Jayan, and V. Sebastian, Materials Today Communications, **28**, 102650 (2021). https://doi.org/10.1016/j.mtcomm.2021.102650
[13] M.G. Ju, M. Chen, Y. Zhou, J. Dai, L. Ma, N.P. Padture, and X.C. Zeng, Joule, **2**, 1231 (2018). https://www.cell.com/joule/pdf/S2542-4351(18)30187-9.pdf
[14] T. Leijtens, G.E. Eperon, N.K. Noel, S.N. Habisreutinger, A. Petrozza, and H.J. Snaith, Advanced Energy Materials, **5**(20), 1500963 (2015). https://doi.org/10.1002/aenm.201500963
[15] T.P.I. Saragi, T. Spehr, A. Siebert, T. Fuhrmann-Lieker, and J. Salbeck, Chemical Reviews, **107**, 1011 (2007). https://doi.org/10.1021/cr0501341
[16] J.M. Tour, R. Wu, and J.S. Schumm, Journal of the American Chemical Society, **112**, 5662 (1990). https://doi.org/10.1021/ja00170a053
[17] A.F. Akbulatov, L.A. Frolova, M.P. Griffin, I.R. Gearba, A. Dolocan, D.A. Vanden Bout, S. Tsarev, E.A. Katz, A.F. Shestakov, K.J. Stevenson, and P.A. Troshin, Advanced Energy Materials, **7**, 1700476 (2017). https://doi.org/10.1002/aenm.201700476
[18] Z. Hawash, L.K. Ono, S.R. Raga, M.V. Lee, and Y. Qi, Chemistry of Materials, **27**, 562 (2015). https://doi.org/10.1021/cm504022q
[19] A.K. Jena, Y. Numata, M. Ikegami, and T. Miyasaka, Journal of Materials Chemistry A, **6**, 2219 (2018). https://doi.org/10.1039/C7TA07674F
[20] K. Norrman, M.V. Madsen, S.A. Gevorgyan, and F.C. Krebs, Journal of the American Chemical Society, **132**, 16883 (2010). https://doi.org/10.1021/ja106299g
[21] L. Etgar, P. Gao Z. Xue, Q. Peng, A.K. Chandiran, B. Liu, M.K. Nazeeruddin, and M. Gratzel, Journal of the American Chemical Society, **134**(42), 17396 (2012). https://doi.org/10.1021/ja307789s
[22] M.O. Abdulmalik, E. Danladi, R.C. Obasi, P.M. Gyuk, F.U. Salifu, S. Magaji, A.C. Egbugha, and D. Thomas, East European Journal of Physics, 4, 125 (2022). https://periodicals.karazin.ua/eejp/article/view/20949
[23] J. Barb´e, M.L. Tietze, M. Neophytou, B. Murali, E. Alarousu, A. el Labban, M. Abulikemu, W. Yue, O.F. Mohammed, I. McCulloch, A. Amassian, and S. del Gobbo, ACS Applied Materials Interfaces, **9**, 11828 (2017). https://doi.org/10.1021/acsami.6b13675
[24] S. Ahmed, F. Jannat, M.A.K. Khan, and M.A. Alim, Optik, **225**, 165765 (2021). https://doi.org/10.1016/j.ijleo.2020.165765

ЯКІСНЕ ТЕОРЕТИЧНЕ ДОСЛІДЖЕННЯ НЕОРГАНІЧНИХ СОНЯЧНИХ ЕЛЕМЕНТІВ НА ОСНОВІ ПЕРОВСКІТУ, БЕЗ HTM $RbGeI_3$, З ВИКОРИСТАННЯМ SCAPS-1D ЯК ШЛЯХУ ДО 3,601% ЕФЕКТИВНОСТІ

Мері Т. Екву[a], Елі Данладі[b], Ніколас Н. Таці[c], Ідоко С. Харуна[d], Осаретін Е. Окоро[d], Філібус М. Гюк[e], Олаїнка М. Джімо[f], Ріта К. Обасі[d]

[a]*Факультет фізики, Технологічний інститут ВПС, Кадуна, Нігерія*
[b]*Факультет фізики, Федеральний університет наук про здоров'я, Отукпо, штат Бенуе, Нігерія*
[c]*Факультет фізики, Університет штату Ріверс, Порт-Гаркорт, штат Ріверс, Нігерія*
[d]*Центр розвитку супутникових технологій NASRDA, Абуджа, Нігерія*
[e]*Факультет фізики, Університет штату Кадуна, Кадуна, Нігерія*
[f]*Факультет фізики, Федеральний університет, Дутсін-Ма, штат Каціна, Нігерія*

Наявність токсичного свинцю в перовскітних сонячних елементах перешкоджає їх комерційній життєздатності. У цій роботі було запропоновано та реалізовано мезоскопічні неорганічні безсвинцеві перовскітні сонячні батареї на основі RbGeI3 за допомогою інструменту моделювання SCAP. Було проаналізовано вплив матеріалу транспортування електронів (ETM) і товщини поглинача. Коли пристрій було вперше змодельовано, його ефективність перетворення потужності (PCE), коефіцієнт заповнення (FF), щільність струму (J_{sc}) і напруга холостого ходу (V_{oc}) досягали значень 3,584%, 48,477% для коефіцієнта заповнення, 25,385 мА/см^2 для J_{sc} і 0,291 В для V_{oc}. Коли ETM і абсорбер мають ідеальну товщину 0,08 і 0,40, розвиток ефективності стає стабільним. Використовуючи вищезазначені параметри, оптимізований пристрій PSC дав такі значення: PCE = 3,601%, J_{sc} = 25,386 мА/см^2, V_{oc} = 0,291 В і FF = 48,637%. Покращення PCE порівняно з базовим пристроєм без оптимізації становить приблизно 1,01 рази. Отримані дані показують, що перовскітний сонячний елемент без HTM має значну здатність поглинати енергію фотонів і виробляти електрони. Він також показав, як створити екологічно чисту та економічно життєздатну технологію.

Ключові слова: *перовскітні сонячні елементи; $RbGeI_3$; SCAPS; товщина шару*